Epitaxial Growth and Intrinsic Magnetic Properties of Magnetic Thin Films on Semiconductor Materials

Cong Lu

Doctor of Philosophy

University of York

Electronics

September 2013

Abstract

Spin electronics, or spintronics, is an emergent interdisciplinary area whereby the spin degree of freedom in electronic devices is employed. One of the most important topics of spintronics is to develop magnetic/semiconductor hybrid materials for the next generation spin devices such as Spin-FET. This dissertation investigates the magnetic properties of magnetic thin films deposited on semiconductor substrate. Fe and Ni films have been deposited onto GaAs substrate with different substrate treatment. Both single and poly crystalline samples were developed during the process, and the magnetic properties were compared to explore the differences. The origin of a uniaxial magnetic anisotropy (UMA) from the crystal symmetry of the bcc Fe, observed in Fe/GaAs (100) has been investigated.

Another major work for this thesis is the Artemis TR-ARPES (time resolved – angular resolved photoemission spectroscopy) project in Rutherford Appleton Laboratory. Successful MBE growth was achieved for the first time during the Artemis TR-ARPES project, followed by static and time-resolved MOKE, and time-resolved photoemission measurements. Preliminary time-resolved photoemission spectroscopy measurements has been performed on the single crystal Fe samples, which is the world first result in term of the study of the time-dependent valence band structures using direct photoemission technique from a metallic material.

The research finally extended to the CoFeB film on GaAs substrate. The discovery of uniaxial magnetic anisotropy of this amorphous film make it one of the hottest topic in research. XMCD measurements were conducted and the results went through a series of calculations gives an indication of the relation between magnetic moment to the anisotropy. TEM inspections offers a clear look at the interface of the samples.

List of Figures

Chapter 3

Chapter 4

Chapter 5

Chapter 6

List of Tables

Acknowledgements

A thesis is a summary of the research work and results of years of hard work that only could have been possible with many others helping me by my side. My first gratitude would be my supervisors Prof. Yongbing Xu and Dr. Jing Wu for the offering me an opportunity of PhD research and freedom to let me work on my own.

I would also thank Dr.Emma Springate, Dr. Cephise Cacho, Dr. Edmond Turcu and the technician team from Artemis Lab, Central Laser Facility in Rutherford Appleton Laboratory for such an exciting collaboration; Dr. Iain Will, Mr. Jonathan Creamer, Mr Charan Panesar for professional support and guidance in the MBE lab and cleanroom; Dr. Vlado Lazarov, Mr Ian Wright for the instructions in the nanocentre. My practical experience was sharpened because of you, and it really benefits me throughout the whole PhD period.

My colleagues are the next group of people I must pay gratitude for. You have been my spiritual companions for years and we shared the same experience of pursuing for PhD degree. I'm glad some of you have already achieved it, and I wish those who are still on the way the best luck. Your names are: Dr Guodong Li, Dr, Daxin Niu, Dr Johnny Wong, Dr Wen Zhang, Dr Xiao Zou, Dr Jialin Liao, Dr Zhaocong Huang, Dr An Ding, Dr Xuefeng Hu, Dr Tuyuan Cheng. Mr Nicholas Maltby, Dr James Sizeland, Dr Wenqing Liu and Mr Shuo Zhao. Special thanks go to Dr. Shunpu Li, who has contributes a lot for my last period of experiment and writing up.

The last and the greatest belongs to my girlfriend Dr. Tian Tian (soon to be) and dearest families, for all of yours' years of support, guidance, and tolerance. I can never say enough about how I appreciate your unconditional and immense love.

Declaration of Authorship

I declare that this thesis titled, “Epitaxial Growth and Intrinsic Magnetic Properties of Magnetic Thin Film on Semiconductor Materials”, and the work presented in it are my own. I confirm that:

This work was done wholly or mainly while in candidature for a research degree at this university and has not been submitted previously for a degree at this or any other university.

Where I have quoted from the work of others, the source is always given. With the exception of such quotations, this thesis is entirely my own work. I have acknowledged all main sources of help.

Where the thesis is based on work done by myself jointly with other, I have made clear exactly what was done by others and what I have contributed myself.

1. Lu C, Lu X, Jin F, Yan Y, Yan L, Wu J, et al. The Effect of GaAs Substrate Treatment on the Magnetic Properties in Fe/GaAs (100). Submitted to IEEE TRANSACTIONS ON MAGNETICS 2015. (submitted)

2. Lu, C; Cheng, TY; Willcox, M; Wu, J; Xu, YB, Seddon, E; Cacho, C; Turcu, E;Springate, E, “Probing the microscopic origin of laser-induced ultrafast spin dynamics using time resolved photoemission/MOKE”, poster presentation at the WUN spintronics international conference at the University of Sydney, 23-25 July 2012.

3. Lu, C; Cheng, TY; Willcox, M; Wu, J; Xu, YB, Seddon, E; Cacho, C; Turcu, E;Springate, E, “Probing the microscopic origin of laser-induced ultrafast spin dynamics using time resolved photoemission/MOKE”, in preparation.

4. Li, J; Jiang, YZ; Ma, TY; Lu, C; Xu, YB; Yang, DR; Yan, M, “Structure and magnetic properties of gamma '-Fe4N films grown on MgO-buffered Si (001)”, PHYSICA B-CONDENSED MATTER 407, 4783-4786 (2012).

5. Bowerbank, T ; Ding, A; Lu, C; Xu, YB, "Shape Effect of Magnetic Nanoelements as Biomolecular Labels for Magnetic Biosensors", IEEE TRANS. MAGN. 48, 3681-3683 (2012).

6. Ding, A; Will, I; Lu, C; Xu, YB, "Vortex Domain Wall Formation in Nanowires With Twin Pinning Sites", IEEE TRANS. MAGN. 48, 2304-2306 (2012).

7. Zhang, L; Ma, TY; Ahmad, Z; Yuan, TZ; Lu, C; Xu, YB; Yan, M, "Low temperature pulsed laser deposition of textured gamma '-Fe4N films on Si (100)"

8. Wenqing Liu, Weiyi Wang, Jiajun Wang, Fengqiu Wang, Cong Lu, Feng Jin, Anmin Zhang, Y.B. Xu, Qunxiang Li, Qingming Zhang, Gerrit van der Laan, and Rong Zhang, "Atomic-Scale Interfacial Magnetism in Fe/Graphene Heterojunction"

for my dearest families…

Chapter 1

Introduction

1.1 The Current Information Industry

The success of semiconductor based electronics has been built on the nature of charge freedom of electrons in semiconductors. The impact started from the first discovery of transistor action in Bell Labs in 1947. Since then, many other semiconductor devices such as field-effect-transistors (FET), light-emitted diodes (LED), integrated circuits (IC) and semiconductor laser have become available in both cooperative and consumer market. This revolution brought overwhelming development of computational industry but at the same time demands higher performance constantly. Ever since Gordon Moore, a cofounder of Intel predicted the famous Moore's Law that not only defined, but also urged on the industry to double the density of components in an integrated circuit chip. After over decades of development, the industry has hit the wall which higher performance draw exponentially more power and generate enormous heat as waste of energy. Demands for higher speed, lower energy dissipation and denser medium and components have been climbing to the top of the priority list and is now inevitable.

The next generation of electronic devices will be smaller, more robust and most importantly, have lower energy consumption. Successors to silicon technologies have been proposed, such as single-electron transistors, molecular-electronic devices based on organic materials, and carbon nanotubes etc. All of which are either based on a complete different genre of materials or a new operational mechanism. Such propose requires years if not decades of fundamental research and debates, extensive development of correlated industries, and unavoidably huge capital investment. If there is a solution that allows us to wisely use the current transistors, it could be the more efficient and immediately obvious. One possibility might be to utilise the intrinsic angular momentum or the spin of an electron as an extra degree of freedom in electronic devices. This newly emerging field of research has triggered development of a series of new multidiscipline researches which aim at integrating spin dependent effects with the current developed semiconductor functionalities. The term "spintronics" is generally used to encompass the ideas of coupling electronic spin and charge based physics and functionalities in one field.

1.2 Definition and Application of Spintronics

Spintronics, also named “spin electronics” or “magnetoelectronics”, refers to a research field that utilizes the spin degree of freedom of electrons in devices. The spin dependent conduction and spin transportation in metals and semiconductors are believed to have great practical application potential and thus draw lots of fundamental research interest.

Spintronics came to the interests of researchers since the discovery of the giant magnetoresistance effect (GMR) in 1988 by French and German physicists who both later on were rewarded Nobel price. It results in spin dependent conduction in magnetic thin films which cause phenomenon changes in resistivity when magnetization state is changes. The most famous application for this effect was for read head incorporating GMR material in hard-disk drives that would be able to sense much smaller magnetic field changes and thus greatly increase the storage density on each hard disk

The potential applications of spintronics is huge and expanding, as it could help constructing new devices combining logic, storage and sensor applications. There are currently two major approaches in designing and manufacturing spintronics devices. One is to perfect current GMR and TMR based technologies by either developing new materials that has larger spin polarization or making improvements to the devices to allow better spin filtering; the other is more focused on utilizing and generating spin-polarized current, which requires the material to be functional as spin polarizer or spin valve.

One of the most typical magnetoelectronic devices is the magnetic hard drive. Developed on the basis of GMR effect, [1] this type of hard drives uses GMR sandwich structure heads that comprises alternating ferromagnetic and nonmagnetic metal layers so that a small magnetic field can produce large change in electrical resistance by switching the relative direction of the magnetization. Over the past decade, GMR and TMR heads has boosted the disk drive capacity from 20 to more than 1000GB per platter.

Metallic spintronic devices, such as hard disk read heads and magnetic random access memory (MRAM) have been one of the most successful technologies in the last decade. However hybrid spintronic devices consisting of both magnetic metals and semiconductors offers an opportunity to unify processing, communication, and storage within the same technology. [2] The hybrid ferromagnetic and semiconductor structures have demonstrated their potentials for possible high efficient spin injection at room temperatures both theoretically and experimentally by employing a Schottky tunnelling barrier between ferromagnetic metals and semiconductors. [3,4]

1.3 Aims of the PhD work

To successful incorporate spins into semiconductors devices, the control of the magnetic properties during thin film growth and the understanding of spin dynamic processes within the hybrid ferromagnetic (FM)/semiconductor devices are one of the most important issues in current spintronics. This PhD work aims to take advantage of in-situ characterisation to study the dependence of static and dynamic magnetic properties on the growth condition, and in particularly, the semiconductor substrates, of the ferromagnetic layers of FM/semiconductor structures. An in-situ magneto-optical Kerr (MOKE) magnetometer has been set up to monitor the developing of magnetic moment and magnetic anisotropy during MBE growth of magnetic thin films on semiconductor substrates.

Another important goal is to make use of the extreme violet ultrafast light source in the Artemis station in the Rutherford Appleton Laboratory to study the electronic band dynamics of FM/semiconductor structures after laser excitation by time-resolved photoemission spectroscopy. The instrumentation involves building up a MBE growth chamber in the Artemis station and connecting it with the main photoemission chamber via a transfer arm, and set up time-resolved photoemission spectroscopy measurements. Alongside the time-resolved photoemission spectroscopy, an in-situ time-resolved MOKE is built up by another PhD student so as to compare the global magnetisation dynamics with the transient changes in the electronic band of the ferromagnetic thin films of FM/semiconductor hybrid structures.

Last but not the least, an XMCD centred project were included as the third contribution. This project uses the synchrotron radiation as a powerful tool to analyse the magnetic

moment information for individual elements in magnetic films. And to use the information to search the contribution of uniaxial magnetic anisotropy in an amorphous film on semiconductor substrates.

1.4 Overview of the Thesis

The following chapter reviews the magnetic ordering and the origin of magnetic anisotropy. It also characterise anisotropy into three disciplines and gives theoretical explanation for each of them. It then move the topic to spin dynamics, introducing the mechanism of femtomagnetism and its experimental measurements. The experimental methods used for this project will be described in Chapter 3 covering the whole process from preparing, producing and characterisation of a magnetic thin film sample. In Chapter 4, the instrumentation and measurements performed in the Artemis project in Rutherford Appleton Laboratory is described. The details of the extreme violet beam line, the growth chamber, and the photoemission chamber are included. The MBE growth, static MOKE measurements, and time-resolved photoemission spectroscopy results of Fe/GaAs structures are presented. Chapter 5 is the second result chapter on growth and in-situ MOKE measurements of Fe/GaAs and Ni/GaAs thin films samples with various thickness. The effect of the GaAs substrate processing on the magnetic properties of the top Fe and Ni layers has been studied in details. This work also serves as a preparation for the dynamic studies of such hybrid structure in the Artemis station in the Rutherford Appleton Laboratory. Chapter 6, as the last result chapter, covers the area of substrate orientation dependency and XMCD measurements of amorphous CoFeB on GaAs substrates. The magnetic moment of both Co and Fe elements were separately analysed regarding to the XMCD spectra. The results are supported by VSM and TEM cross section inspections to identify the possible origins of UMA behaviour.

Chapter 2

Theory background and Literature Review

2.1 Introduction

In this chapter, I will review the background theory relevant to the experiments, which will be discussed later in the thesis. The origin of ferromagnetism and magnetic anisotropy will be presented first. Then a brief on the magnetisation dynamic studies on femtosecond time domain is introduced. Finally I will present the current studies of two typical FM/semiconductor hybrid structures, namely, Fe/GaAs and Ni/GaAs.

2.2 Magnetic Ordering

The term Magnetic Ordering comes about when the spins of the electrons in a material interacts with each other through exchange interactions. Exchange interaction is a quantum mechanical effect that describes the change in energy and distance of multiple particles when their work functions are overlapped. Its value determines the spin alignments of the material. A positive exchange interaction will align the spins in parallel to each other and lead to ferromagnetism; while a negative one will put spins antiparallel with one another, and thus lead to antiferromagnetism.

When the exchange interaction between two spins is of a positive value, the spins will be aligned in the same direction regardless of the existence of external field. Below the Curie temperature of the material, this gives rises to spontaneous magnetization. This type of magnetic ordering is called Ferromagnetism. In microscopic view, these aligned spins should generate a magnetic moment pointing to a certain direction; however, most macroscopic ferromagnetic materials do not show a net magnetization unless an external field is applied. This can be explained by introducing the concept of domains.

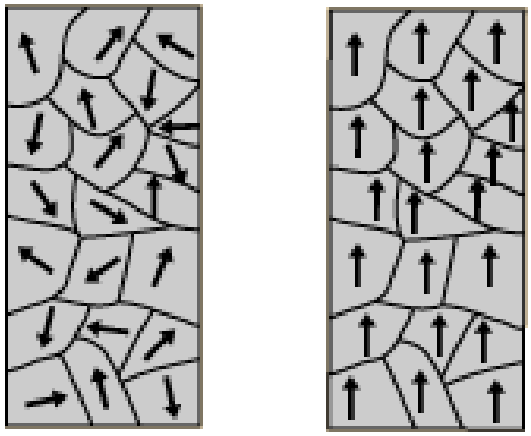

Figure 2.1. Domain magnetizations within a bulk material without and with an external field.

A magnetic domain is small area within the material, in which the spins of electrons are aligned to one same direction but can be different from those of neighbouring domains. Domains are formed because their configuration minimizes the total stray field energy of the bulk material, which is a more energetically favourable state for the coupled spins. When a macroscopic material has all of its spins aligned, the magnetostatic energy reaches to the maximum value, which is an unfavourable state. To enter the favourable state (the lowest magnetostatic energy), a single domain would break into multiple small units that all contain strongly coupled and aligned spins, but pointing to different directions. The preferential directions of each domain are determined by the magnetic anisotropy in an absence of external field. At the boundary regions of the domains, the magnetization directions are gradually rotated to align with the neighbouring domain. Depending on the thickness of the material, the rotation of magnetization can either take place in plane which is parallel to the plane of domain wall, or perpendicular to it. In the thin films, it is usually Neel wall, and in the thick films Bloch wall. The width of domain walls is usually within tens of nanometres, and is determined by the exchange

and anisotropy energy. Misaligned preferential directions cause the bulk material to show very weak net magnetization, the real value is very close to zero.

If an external field is brought in and applied across a ferromagnetic material, it would force the magnetization directions of domains to align, and as a result, produce a net magnetization vector. One of the iconic properties of ferromagnetic materials is that the response of the net magnetization to the external field is nonlinear. The magnetization increases rapidly at first, then as more and more domains are aligned in the field direction, the rate will go down until eventually the magnetization will reach to a maximum value which is called the saturation point (Ms). When the field is decreased, the magnetization does not decrease accordingly on the same original path. Instead, it will decrease slower than the external field and thus not return back to zero when the field goes all the way back to zero. This remaining magnetization is called remnant magnetization (Mr). In order to bring the remnant magnetization back to zero, a negative magnetic field is required. This negative field will break the alignment of domains and put them into a randomized state, so that the net magnetization of all domains will be zero. The field required to accomplish this is called the coercivity (H_c). The coercivity is a very important property of any ferromagnetic materials. It is strongly affected by the crystalline structure of the material, as well as the deposition conditions and processes.

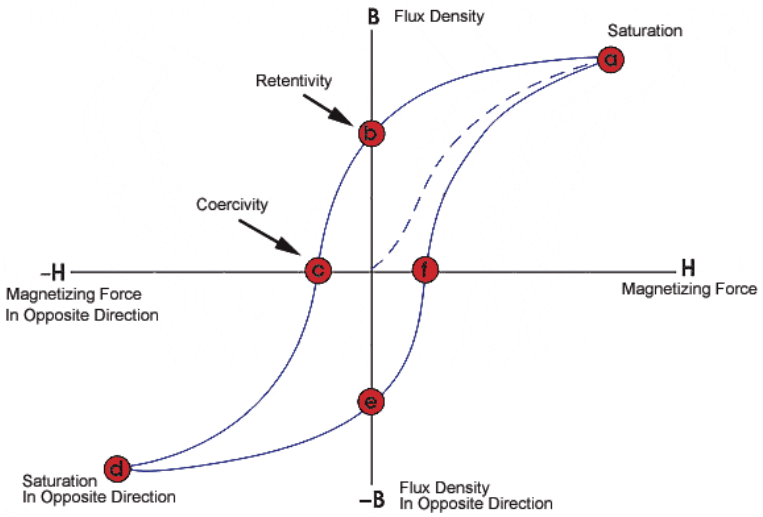

Figure 2.2. Typical hysteresis loop.

If the field is further decreased, the domains will be re-aligned to the opposite direction, and a negative saturation point will be reached eventually. A negative remnant and coercivity will also present if the field is increased back to zero, and when the domain is re-randomized again. In general cases, the negative and positive Ms, Mr and H_c are expected to be of the same value, thus the plot of magnetization against applied field on positive and negative regions should be symmetrical and form a closed loop. This loop is called the Hysteresis loop.

As mentioned before, the alignment of the spins or the spontaneous magnetization would only happen below the Curie temperature. This temperature is different for various materials, and is dependent to the strength of exchange interaction between spins. Above this critical temperature, thermal energy will surpass the exchange energy, which causes coupled spin align broken up, the ferromagnetic material undergone a phase transition and effectively become paramagnetic.

2.2.1 Ferromagnetism

A ferromagnetic material is a material in which the magnetic dipole moments of individual atoms are strongly coupled and aligned parallel, so that a spontaneous magnetisation exists even in the absence of an external magnetic field. When the temperature increases and exceeds the Curie temperature, the coupling between the atomic dipoles can no longer keep them aligned parallel, and then the spontaneous magnetisation disappears and the material becomes paramagnetic. A ferromagnetic specimen may not exhibit a macroscopic magnetic moment when the applied field is zero, but a small applied field will produce a magnetic moment with magnitude many orders larger than that produced in a paramagnetic substance. Weiss suggested the existence of domains to explain this. The magnetic moment of the entire sample is the vector sum of the magnetic moment of each domain. The direction of each domain need not be parallel so the entire specimen may have zero net magnetic moment. The small applied field aligns the domain arrangement in the sample and a net magnetisation exists.

The strong interaction in a ferromagnetic material may be considered to be an effective internal magnetic field, H_m, which tends to align the atomic dipoles parallel to each other. The amplitude of H_m could be estimated in the following way as described in Morrish [5]. The Curie temperature T_c must be the temperature at which the thermal agitation energy is sufficient to destroy the spontaneous magnetisation. For an atom with a dipole moment of one Bohr magneton, we get

$$\mu_B H_m \approx \mathrm{k}T_c$$

(2.1)

For $T_c \cong 10^3\ K$, we get $H_m \approx 10^7\ Oe$. Heisenberg showed that the molecular field is the result of the quantum mechanical exchange interaction. His theory is based on the Heitler-London method developed for the hydrogen molecule. The Schrödinger equation for two non-interacting electrons moving in the same potential field is

$$\left[-\frac{\hbar^2}{2m}\left(\nabla_1^{\,2}+\nabla_2^{\,2}+V(q_1)+V(q_2)\right)\right]\psi = E\psi$$

(2.2)

where the subscripts 1 and 2 refer to the two electrons, and q_1 and q_2 represent their co-ordinates. Because the two electrons are indistinguishable,

$$\left|\psi(1,2)\right|^2 dq_1 dq_2 = \left|\psi(2,1)\right|^2 dq_1 dq_2$$

(2.3)

where $\psi(1, 2)$ is the wave function for the two electron system and $\psi(2, 1)$ is that when the two electrons are interchanged. The only possible solutions for equation 1.1.3 are the linear combinations of one-electron wave function,

$$\psi_{sym}(1,2) = \frac{1}{\sqrt{2}}\left[\psi_a(1)\psi_b(2) + \psi_a(2)\psi_b(1)\right]$$

$$\psi_{anti}(1,2) = \frac{1}{\sqrt{2}}\left[\psi_a(1)\psi_b(2) - \psi_a(2)\psi_b(1)\right]$$

(2.4)

where $\psi_a(1)$ is the solution of the one-electron Schrödinger equation when electron 1 is in state a and $\psi_b(2)$ is that when electron 2 is in state b. $\psi_a(2)$ and $\psi_b(1)$ are wave functions obtained when electrons 1 and 2 are interchanged.

Electrons are Femions and always have wave functions that are antisymmetric with respect to exchange of electron co-ordinates. One-electron functions are functions of the spatial co-ordinates and of the spin, that is

$$\psi = \phi(r)\chi$$

(2.5)

where ϕ is the solution of a Schrödinger equation for an electron without spin and χ is a function of spin only. There are two possible antisymmetrical forms

$$\psi_I = \phi_{sym}(1,2)\chi_{anti}(1,2)$$

(2.6)

$$\psi_{II} = \phi_{anti}(1,2)\chi_{sym}(1,2)$$

(2.7)

where $\phi_{sym}(1,2)$ and $\phi_{anti}(1,2)$ are symmetric and antisymmetric spatial wave functions, respectively, while $\chi_{anti}(1,2)$ and $\chi_{sym}(1,2)$ are antisymmetric and symmetric spin wave functions, respectively. Therefore ψ_I is the wave function when the spin of two electrons that are anti-parallel to each other, while ψ_{II} is the wave function when the spin of two electrons are parallel to each other.

To illustrate the principle of the interaction between the two-electron system, we can examine a simple example. For the hydrogen molecule, the interaction can be given by Hamiltonian H_{12}, which is

$$H_{12} = \frac{e^2}{r_{ab}} + \frac{e^2}{r_{12}} - \frac{e^2}{r_{1b}} - \frac{e^2}{r_{2a}} \tag{2.8}$$

where r_{ab} is the distance between nuclei, r_{12} is the distance between electrons and r_{1b} and r_{2a} are the distances between a given nucleus and the electron on the other atom. The additional energies for the states whose wave functions are given by equation (2.9), (2.10) are, respectively,

$$E_I = A^2(K_{12} + J_{12}) \tag{2.9}$$

$$E_{II} = A^2(K_{12} - J_{12}) \tag{2.10}$$

where

$$K_{12} = \int \phi_a^*(1)\phi_b^*(2)H_{12}\phi_a(1)\phi_b(2)d\tau_1 d\tau_2$$

$$J_{12} = \int \phi_a^*(1)\phi_b^*(2)H_{12}\phi_a(2)\phi_b(1)d\tau_1 d\tau_2$$

(2.12)

Here K_{12} is the average Coulomb interaction energy, and J_{12} is called an exchange integral. If we only consider the spin dependent term, the exchange Hamiltonian of the two-electron system may be written in terms of the electron spins as

$$H = -2J_{12}\mathbf{s}_1 \cdot \mathbf{s}_2$$

(2.13)

For ferromagnetism to occur, J_{12} has to be positive so that the state in which the spins are parallel corresponds to a lower energy state. Suppose that the spatial wave function ϕ has no nodes in the overlap region, so that $\phi_a^*(1)\phi_b^*(2)\phi_a(2)\phi_b(1)$ is positive. For J_{12} to be positive, the contributions from the positive terms of the Hamiltonian must exceed those from the negative. This requires that r_{12} is small and r_{1b} and r_{2a} are big. These conditions are met if r_{ab} is large compared to the radii of the orbitals, as is most likely to be the case for *d* and *f* wave functions for the atoms of some iron and rare earth metals. Figure 2.3 shows schematically the exchange integral as a function of the interatomic distance r_{ab}.

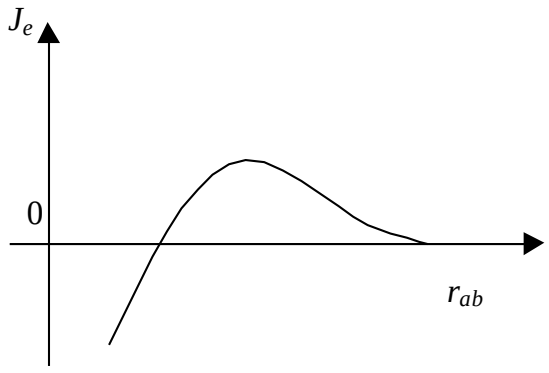

Figure 2.3. Schematic Variation of the exchange integral as a function of the inter-atomic distance, a.k.a the Bethe-Slater Curve.

The Heisenberg theory of ferromagnetism was based on the assumption that the electrons are localised at the atoms. Since most ferromagnetic materials are either metals or alloys, theories considering mobile electrons or holes in unfilled bands have been developed as shown in Fig 2.4 of the spin-dependent density of states (DoS) of Fe. Stoner [6] developed the collective electron theory, calculating the interaction between the electrons of an electron gas. One of the main achievements of this theory is the prediction of non-integral values for n_{eff}, the effective number of magnetic carriers.

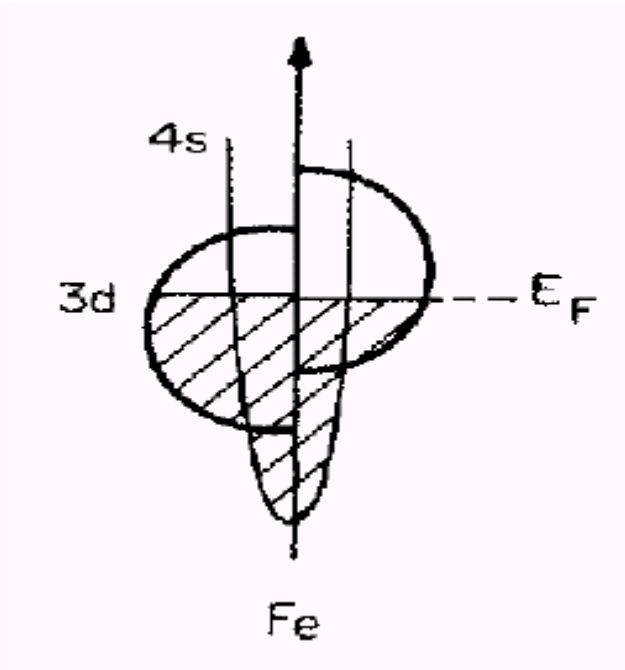

Figure 2.4. The Spin-dependent density of states (DoS) of Fe.

2.3 Magnetic Anisotropy

Anisotropy describes the physical property of a material that is direction dependent. When the magnetization of a material prefers to align to a certain direction rather than the others, the material exhibits magnetic anisotropy. The parameter that defines the magnetization process is called magnetic permeability. It indicates the ease of magnetic flux propagation. Mathematically it is the ratio of the flux density of the magnetic field within the material to its applied field strength, and can be express as:

$$\mu = B/H$$

Where μ is the magnetic permeability of the material (H/m), B is the flux density (T) and H is the applied field (A/m).

Generally speaking, magnetic anisotropy comes from the shape of the material, its crystal arrangement and the stress force that is applied to it. Fundamentally, the sources of the magnetic anisotropy can be characterized as the magnetic dipolar interaction and the spin-orbit interaction.

Considering the long range character of the dipolar interaction, it contributes to the material anisotropy through its shape. This is critical for thin film sample and other types of in-plane magnetization. Within local areas, the electron spins are coupled through spin-orbit interactions to the orbits. These interactions are easily influenced by the crystal lattice, thus responsible for the magneto-elastic or magnetostrictive anisotropies both of which are induced in a strained system. The differences of three major anisotropy terms will be discussed in detail.

2.3.1 Magneto Crystalline Anisotropy

A ferromagnetic crystal exhibits different behaviour depending on the direction along which it has been magnetised. This effect indicates that different crystalline directions are not magnetically equivalent and this can be observed in magnetisation curves by applying an external field along different directions.

Taking a bcc Fe bulk material for example, as illustrated below, an obvious cubic anisotropy appears in the magnetisation curves when applying and increasing fields along different crystallographic axes.

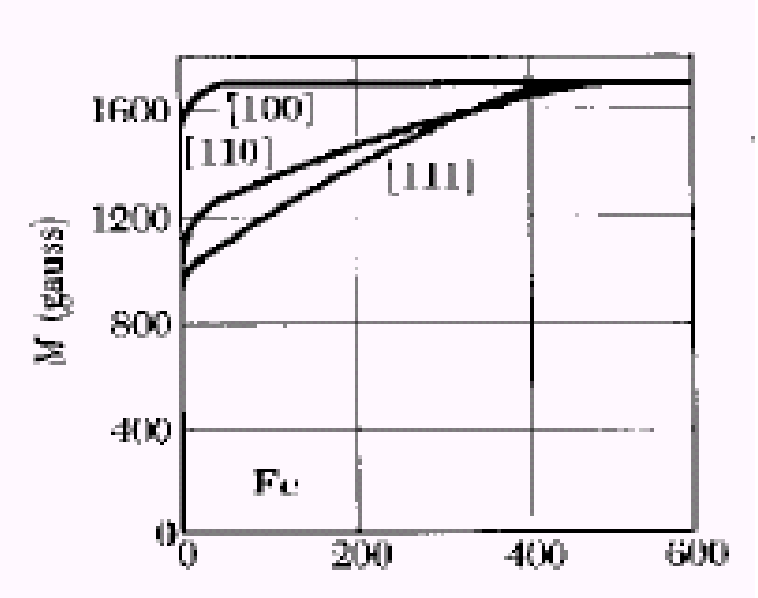

Figure 2.5: Schematic curve of M and H showing the difference in size of field required to achieve same magnetisation along three bcc Fe crystalline axes. [7]

Due to the magneto-crystalline anisotropy, the saturation magnetisation state will be reached at different fields along different directions which can be used to define the easy and hard axes. As shown in Figure 2.5, for magnetite crystals, [100] is the easy direction along which the moments are saturated in a relatively low field, [111] is the

hard direction along which the magnetisation vector, M, reaches the saturation magnetisation, M_s, in a higher field and [110] is the intermediate direction. Given by the difference in the area under *M* and *H* curves, there is an energy difference associated with magnetisation along hard and easy axes. This is called the magneto-crystalline energy.

The easy and hard directions arise from the interaction of the magnetic moment with the crystal lattice (spin-orbit coupling). The magneto-crystalline anisotropy energy is therefore usually written in terms of the angle, θ, between the direction of magnetisation and the axes of the cube. The equivalent anisotropy field can be derived from the anisotropy energy as a function of magnetisation, $\vec{M}$.

$$E_{ani}=K_1\left(\alpha_x{}^2\alpha_y{}^2+\alpha_y{}^2\alpha_z{}^2+\alpha_x{}^2\alpha_z{}^2\right)+K_2\left(\alpha_x{}^2\alpha_y{}^2\alpha_z{}^2\right)+\cdots$$

$$\vec{H}_{crystal}=-\frac{dE}{d\vec{M}}$$

(2.14)

where K_1 and K_2 denote the magnetic anisotropy constants of first and second order respectively and $a_{x,y,z}$ represents the direction cosines between $\vec{M}$ and the cubic edge.

2.3.2 Surface and Volume Contribution

A typical expression for the dominant anisotropy energy in thin film is

$$E = -K\cos^2\theta \tag{2.15}$$

where E is the orientation-dependent energy of the magnetisation, θ is the angle between the magnetisation and the normal of the film, and K is an anisotropy constant [8]. K is positive when the magnetisation prefers to be perpendicular to the plane of film. A second-order uniaxial term $K_2\cos^4\theta$ is usually very small. In order to distinguish the contributions from the surface or interface from the volume or bulk, K_s is defined as surface anisotropy energy per unit area, and K_v is defined as volume anisotropy energy per unit volume. For a magnetic layer with its thickness t much smaller than its exchange length, the average magnetic anisotropy energy may be written as

$$K_{eff} = K_v + 2K_s / t \tag{2.16}$$

The factor 2 comes from the assumption that the magnetic layer is bounded by two identical interfaces. Equation (2.16) is often used in analysing experiments and K_v and K_s can be obtained by plotting the product Kt versus thickness t. Below a certain thickness, the surface anisotropy contribution outweighs the volume anisotropy contribution, and results in perpendicular magnetisation.

2.3.3 Shape Anisotropy

The shape anisotropy due to the long-range dipole interaction senses the outer boundaries of the sample. It is the main contribution to K_v in equation (2.16). The shape effect can be described via a demagnetising field. For a thin film, the corresponding anisotropy energy per unit volume is

$$E_d = 2\pi M_S^2 \cos^2\theta \qquad (2.17)$$

where θ is the angle between the magnetisation and the normal of the film[8]. As shown in equation (2.17), this contribution favours an in-plane magnetisation rather than a perpendicular one, and is independent of thickness, so this anisotropy energy only contributes to K_v.

2.3.4 In-Plane Uniaxial Anisotropy

Strain, oblique deposition, and in-situ magnetic field during growth may induce an in-plane uniaxial anisotropy in a thin film sample. It can be seen in magnetisation curves that smaller field is required to saturate the sample along one in-plane direction than along others. The axis along which the sample is easily saturated is called easy in-plane uniaxial axis, while the axis along which the sample is difficult to saturate is called hard in-plane uniaxial axis. The energy of the in-plane uniaxial anisotropy has the form

$$E_u = -K_u \cos^2(\theta_k - \theta) \tag{2.18}$$

where K_u is the uniaxial anisotropy constant, θ_k is the angle between the easy in-plane uniaxial anisotropy axis and the static field **H,** and θ is the angle between **M** and **H.** In a bulk material, the magnetisation tends to lie along certain crystallographic axes due to the spin-orbit interaction.

2.4 Femtomagnetism

One of the most intriguing issues in today's nanomagnetism is the dynamics of spin systems at down to femtosecond timescales – femtomagnetism. Interest in this challenging field is fuelled both by a scientific desire to further fundamental understanding of spin systems under extreme non-equilibrium conditions and by the push to develop novel concepts for ultrahigh density magnetic data storage and ultrafast spintronic devices such as spin-FETs and spin quantum bits. Indeed, a clear understanding of the electron/spin dynamics in transition metal magnetic thin films on semiconductors is pivotal to the further development of materials for spintronics applications and hence for the whole burgeoning area of spintronics itself.

Beaurepaire and his co-workers reported their pioneering work on ultrafast magnetisation dynamics induced by femtosecond laser pulses in the visible in ferromagnetic transition metals in 1996 [9], as shown in Fig 2.6. They observed that the time-resolved magneto-optical contrast dropped by 50% on a timescale of 1-2 ps following the absorption of a 60 fs laser pulse. This rapid reduction was interpreted as non-equilibrium heating of the spins, electrons, and the lattice resulting in an ultrafast demagnetisation of nickel. The non-equilibrium states developed in magnetic materials following intense fs laser excitation represent a subject that has been widely investigated over the last decade [10].

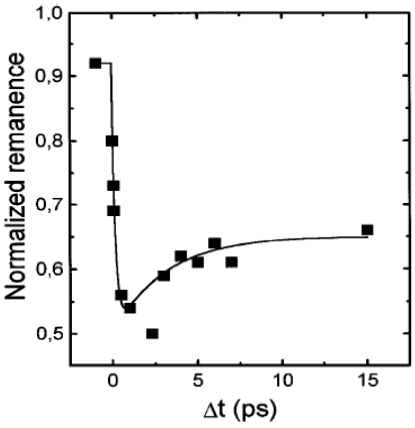

Figure 2.6. The ultrafast demagnetisation after 60 fs laser excitation on a 22 nm thick Ni film. [1]

During laser-induced ultrafast demagnetisation the energy and momentum carried by the photon are directly absorbed by the valence band electrons [11,12]. For an intense optical excitation, a non-equilibrium distribution of electron density of states (DOS) are created [13], as shown in Fig 2.6, left. Such a non-thermal carrier distribution will redistribute its energy by electron-electron collisions among the electron subsystem. This electron-electron scattering leads to internal thermalisation among the electrons during the electron thermalisation time τ_{th} (Fig 2.6). The time required for thermalisation depends on the excitation density of electrons. At subsequent delays, the excess energy is transferred to the lattice via electron-phonon scattering, resulting in energy transferred to the lattice and 'cooling' of the electron gas. The spin system temperature responds on a similar time scale to the electron system, which leads to the demagnetisation process in ferromagnetic 3d-transition metals, such as Fe, occurring on sub-picoseconds time scales. In order to conserve angular momentum, laser induced ultrafast quenching of magnetisation must be associated with transient angular momentum transfer between different degree systems.

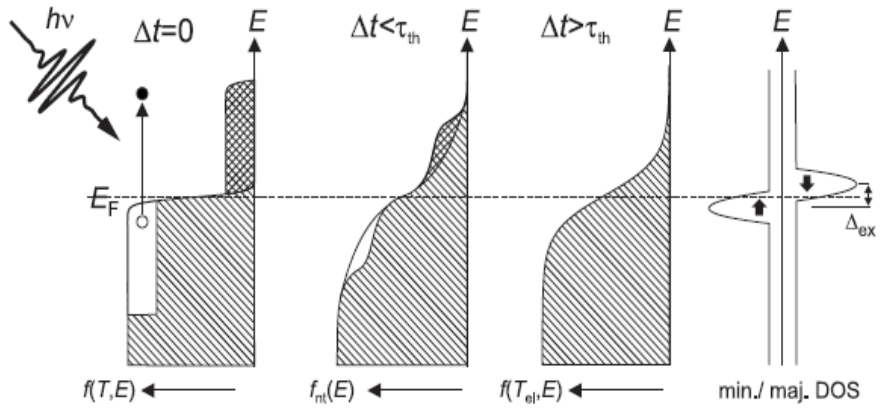

Figure 2.7. Schematic relaxation of the electron system in a metal after intense ultra-short laser excitation. Starting at a Fermi-Dirac distritbution f(T,E) in equilibrium, the intense laser pulse generates a strongly non-thermal electron distribution fnt, which thermalized within the thermalisation time τth. On the right, the typical electronic band structure for a ferromagnetic metal with majority and minority subbands is shown.

However, microscopic mechanism responsive for the first picosecond spin dynamics are still unknown. To accommodate the angular-momentum change associated with a modification of the magnetisation, spin angular-momentum transfer to the lattice has to be invoked, which is governed by spin-orbit coupling. Stamm *et al.* [14] have studied laser-induced ultrafast demagnetisation in Ni thin films by time-resolved X-ray absorption spectroscopy (XAS) and X-ray magnetic circular dichroism (XMCD) at the Ni L_3 edge using the BESSY femto-slicing source. They have observed a XAS energy shift which indicates an increased localization of the 3d/4sp electron and could result in an enhanced spin-orbit coupling. This increased electron localization is interpreted from a shrinking valence band width which shifts the centre of the valence band towards the Fermi level to retain charge neutrality as shown in Figure 2.8.

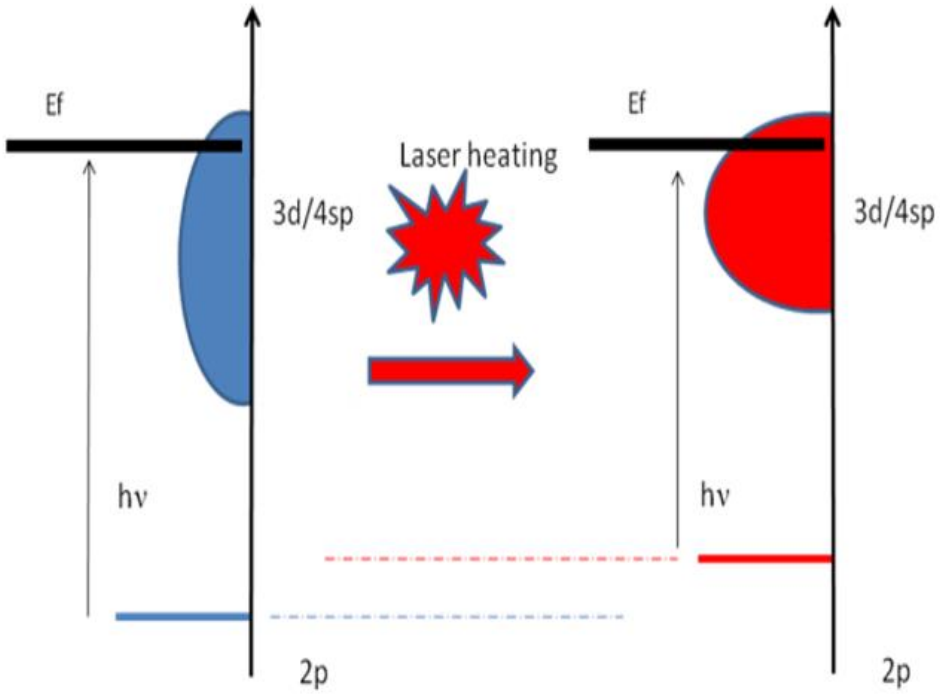

Figure 2.8. Schematic diagram of electronic structure of the 2p core level and 3d/4sp valence band before and after laser excitation in a TM metal.

A direct time-resolved observation of the 3d/4sp band structure with magnetic order information alongside simultaneous time-resolved global magnetisation monitoring will be ideal to get insight into the microscopic origin of the ultrafast demagnetisation during the very first picosecond after pulsed laser irradiation. The high-order harmonic generation (XUV) at the Artemis station provides an unique spectroscopic tool for pump-probe experiments at ferromagnetic transition metal $M_{2,3}$ edges with femtosecond temporal resolution and photon flux about five orders of magnitude higher than the current femto-slicing techniques at synchrotron sources. The energy range of 10-100eV is ideal to probe 3d energy band structures of transition metals and oxides with large cross sections.

One of the projects of this PhD is to perform the time resolved photoemission spectroscopy and compare with the time-resolved magneto optical Kerr effect (TR-MOKE) measurements. The aim is to explore the microscopic mechanisms of the ultrafast demagnetisation by mapping the time-resolved energy band structure and at the same time monitoring the time-resolved globe magnetisation at femtosecond temporal resolution after ultra-short laser excitation in the ferromagnetic transition metal thin films. The temporal evolution of the correlation between the band structure and the global magnetisation induced by laser excitation will provide first direct information on the microscopic origin of, and therefore the insights into the mechanisms of the ultrafast demagnetization.

2.5 Magnetic Thin Film on GaAs

2.5.1 Fe/GaAs

The growth of epitaxial ferromagnetic metal/semiconductor hybrid structures was first demonstrated in Fe/GaAs by Prinz's group in Navel Research Laboratory [15,16]. This is possible in part due to the fact that the lattice constant of bcc Fe (a_o=2.866Å) is almost exactly half that of GaAs (a_o=5.654Å) as shown in Figure 2.9.

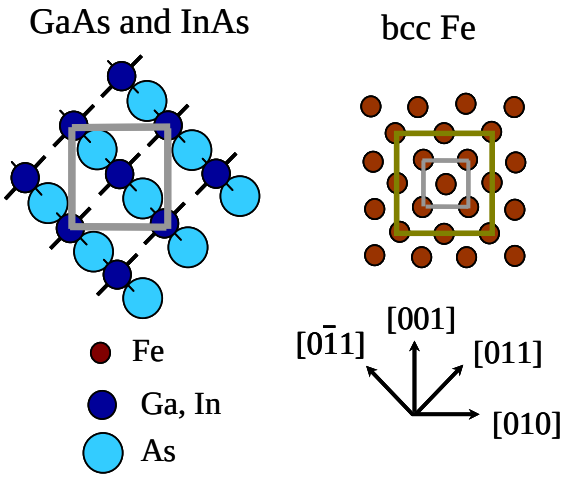

Figure.2.9 Crystal structures of bcc Fe, GaAs(100) and InAs(100). The lattice constants of GaAs and InAs are about twice of that of bcc Fe.

Fe/GaAs continues to be of interest as a model system for the epitaxial growth of ferromagnetic metals on semiconductors. The Fe/InAs hybrid structure is also an interesting system, as metals on narrow gap semiconductors, such as InAs which has a direct band gap as small as 0.36eV at 300K, form low resistance contacts [17]. Though the lattice mismatch of Fe and InAs (a_o=6.058Å) at 5.4% is much larger than that of Fe/GaAs (1.3%), high quality bcc Fe has been demonstrated on InAs (100) surface by Xu et al. [18]. Co and Ni are interesting as their meta-stable bcc phases can be formed on GaAs and InAs in the atomic/nanometer thickness range.

Molecular Beam Epitaxy (MBE) is the most commonly used growth technique to synthesise high quality hybrid ferromagnetic metal/semiconductor structures [19,20,21,22,23]. The typical MBE systems have a base pressure of about 1-2x10^{-10} mbar with a deposition rate of approximately one monolayer (ML) per minute. It is crucial to have a clean and well-ordered semiconductor substrate for the growth. The epi-ready GaAs(100) wafer are usually used. Typical substrate cleaning procedures include the following steps: a)The substrate was chemically cleaned using an H2SO4:H2O2:H2O (4:1:1) solution for 45 seconds, followed by de-ionized (DI) water rinsing and isopropyl alcohol (IPA) vapour cleaning. b) After transferred into the UHV chamber, the substrate was sputtering cleaned for about 30min with an Argon pressure of around 5x10-6 mbar, and the voltage of around 110 eV, and c) annealed at around 830 K for about 30 minutes until a sharp RHEED/LEED pattern can be identified as shown in figure 2.10. To have well-ordered surface with a specific reconstruction, the wafers with an Arsenide capping layer can be used, and then the semiconductor surface reconstructions can the controlled by the annealing temperatures [24]. In the earlier studies [19,21,22], the ferromagnetic layers were grown at elevated temperatures of around 170-200^{o}C, and it was found that this high temperature growth leads to the formation of a magnetic dead layer at the interface. To reduce the intermixing of Fe with Ga, In, or As at the interface, Xu et al [18] found that the ferromagnetic layers can be grown at room temperature.

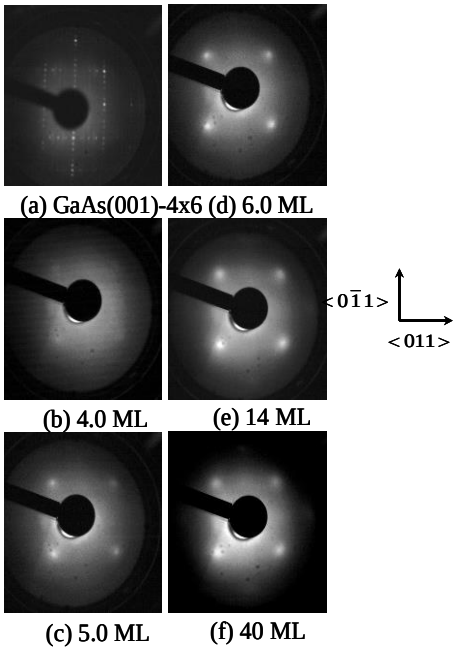

Figure 2.10 LEED patterns of the GaAs(001)-4x6 substrate after As desorption and after Fe deposition. [18]

Fig. 2.10 shows the LEED patterns of Fe/GaAs(100) following the deposition of Fe at room temperatures [23]. No Fe LEED pattern was observed for the first 4ML deposited. After the deposition of 5ML faint LEED spots from the Fe film appear. Clear LEED patterns were observed after the deposition of 6ML. The diffraction spots became broadened at higher coverages. These LEED patterns show that Fe grows epitaxially on GaAs(001) at room temperature with an epitaxial relationship of Fe(001)<100>||GaAs(001)<100>. The lack of Fe LEED patterns for the first four monolayers indicates that the growth proceeds via the three dimensional Volmer-Weber growth mode as previously reported for higher temperature growth, but the LEED pattern develops at a slightly higher Fe coverage (5ML) than that at higher growth temperature (3ML).

One of open issues over almost two decades is the origin of an uniaxial magnetic anisotropy, unexpected from the crystal symmetry of the bcc Fe, observed in Fe/GaAs(100) [19,20,23]. The UMA is dominant in the ultrathin regions as shown by the square loops along the [011] directions. Above critical thicknesses of about 50 ML for Fe/GaAs and 16 ML for Fe/InAs, the cubic anisotropy becomes dominant. There are four possible mechanisms responsible for the UMA observed in Fe/GaAs and Fe/InAs:

a) Shape anisotropy as the films show 3D island growth,

b) If a nearly half-magnetised phase exists at the interface, then this may be partly responsible for the UMA,

c) Intrinsic anisotropy due to the unidirectional nature of Fe-As, Fe-Ga and Fe-In bonds,

d) Magneto-elastic interactions due to strain in the ultrathin epitaxial films caused by lattice mismatch.

STM study shows no evidences of shape anisotropy due to the 3D island growth. The so-called nearly half-magnetized phase at the interface could also be excluded, as this phase does not exist in the samples grown at room temperatures. It is now generally believed that the atomic scale structure related to the semiconductor surface is responsible for this uniaxial anisotropy.

By examining the anisotropy of the Fe films deposited on different kinds of GaAs substrates showing different reconstructions as shown in Fig 2.7, Kneedler *et al* [23] reported that the unidirectional nature of Fe-As or Fe-Ga bonds is responsible for the

UMA. This might be understood as a "chemical" effect, in which the electronic structure of the Fe atoms near the interface differs distinctly from "normal" bcc Fe. The measurements of the thickness dependence of anisotropies of in Fe/GaAs by Brockmann et al [25] demonstrated that the uniaxial anisotropy is a pure interface term originating exclusively from the Fe/GaAs interface, which favours the term of "unidirectional chemical bonding" at the interface.

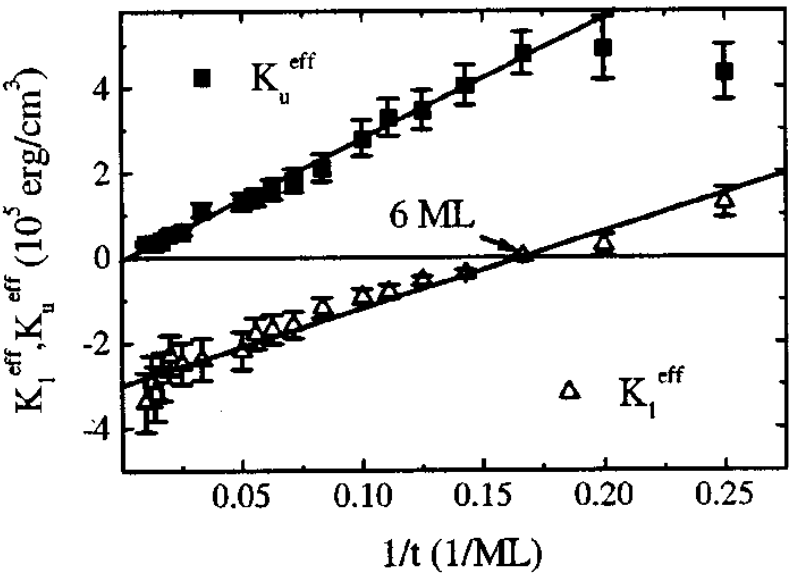

Figure. 2.11 Effective fourfold in-plane magnetic anisotropy constant K1eff (triangles) and effective uniaxial in-plane anisotropy constant KUeff (squares) Vs inverse film thickness for Fe34Co66 films on GaAs (001), determined from MOKE loops. (M. Dumm et al., J. Appl. Phys. 87, 5457, 2000).

Another issue is that uniaxial magneto-elastic coupling due to anisotropic lattice relaxation is the origin of the uniaxial magnetic anisotropy [26]. The magneto-elastic effect occurs as a direct result of the compression or expansion of the Fe film in order to fit the GaAs or InAs lattice respectively. Ahmad and Morley et al found that the magnetoelastic constants of a 10ML Fe film on GaAs could be 20 times larger than that of bulk Fe figure, showing the importance of magneto-elastic coupling in ultrathin films[27,28].

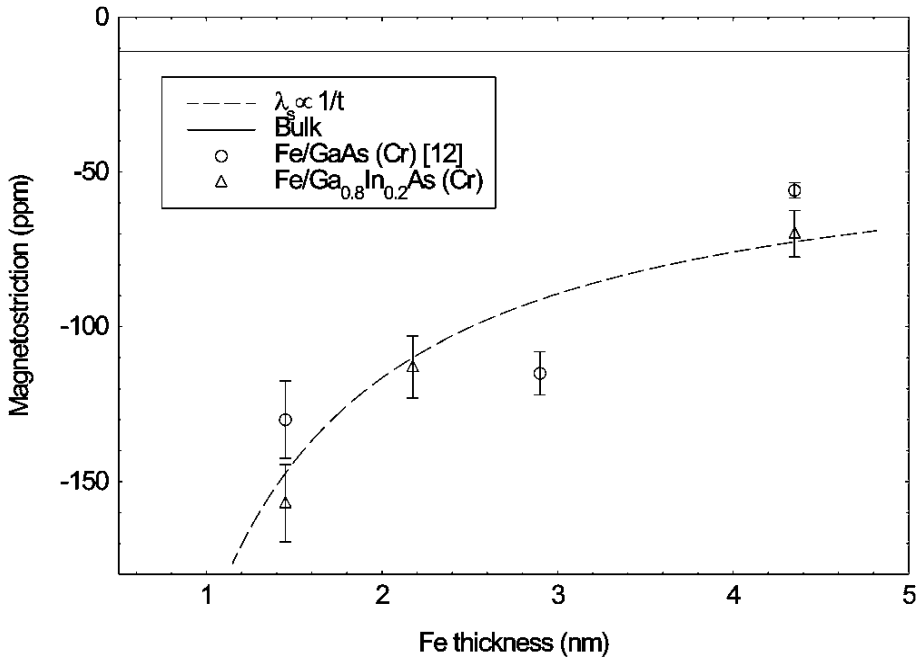

Figure. 2.12. Magnetostriction constants of Fe films on GaAs (100) and Ga0.8In0.2As (100) substrates as a function of Fe film thickness. The solid black line is the magnetostriction constant of bulk Fe in the [110] direction, and the dashed line is proportional to the inverse thickness, and is a guide for the eye. [28]

2.5.2 Ni/GaAs

Epitaxial growth of Ni on GaAs(001) is one of the most interesting hybrid FM/SC systems for heterointerface studies since bcc Ni which does not exist in nature could be formed on GaAs(001) by MBE growth. This was first demonstrated by Tang *et al* [29]. By growing the Ni film at RT, the presence of a bcc phase up to 2.5 nm has been confirmed by in-situ RHEED and ex-situ MOKE showing a fourfold in-plane magnetic anisotropy with the easy axes along the <100> directions. Still, it is expected that the evolution of the bcc phase is strongly dependent on the sample preparation recipe as in the case of bcc Co on GaAs discussed. Beyond 2.5 nm, the fcc phase starts developing and co-exists with the bcc Ni. Moreover, uniaxial anisotropy has been observed to contribute to the total magnetic anisotropy of the film. Recently, a systematic study has been carried out by the same group [30]. Bcc Ni has been epitaxially grown on GaAs(001)-(4x6) at 170 K instead of 300 K. As the authors claimed that a thicker bcc Ni film could be obtained in this condition. The bcc Ni lattice constant was found to be 0.282 nm which is in good agreement with the reported results [31]. A series of MOKE measurements for Ni film thicknesses ranging from 0.8 to 3.0 nm confirmed the absence of a magnetic dead layer in the Ni/GaAs interface. The magnetization of the bcc Ni was determined by ex-situ SQUID at 5 K yielding a value of $0.52 \pm 0.08 \mu_B/atom$ which is similar to the theoretical predicted value of $0.54 \mu_B/atom$. The magnetic anisotropy in the system studied has been attributed to both cubic and uniaxial anisotropies with $K_1 = 4.0 \times 10^5 erg/cm^3$. It has been proposed that the uniaxial term may be a result of the in-plane shear strain induced in the system.

Another approach for growing high quality epitaxial Ni films on GaAs(001) has been given by Scheck *et al*. who use electro-deposition with the intention to overcome the

intermixing at the interface [32]. Figure 2.13 shows the hysteresis loops of four different Ni layers grown on GaAs(001) with thicknesses indicated in the graph. Each graph shows three loops for each of which the orientation of the magnetic field with respect to the GaAs[110] direction is mentioned.

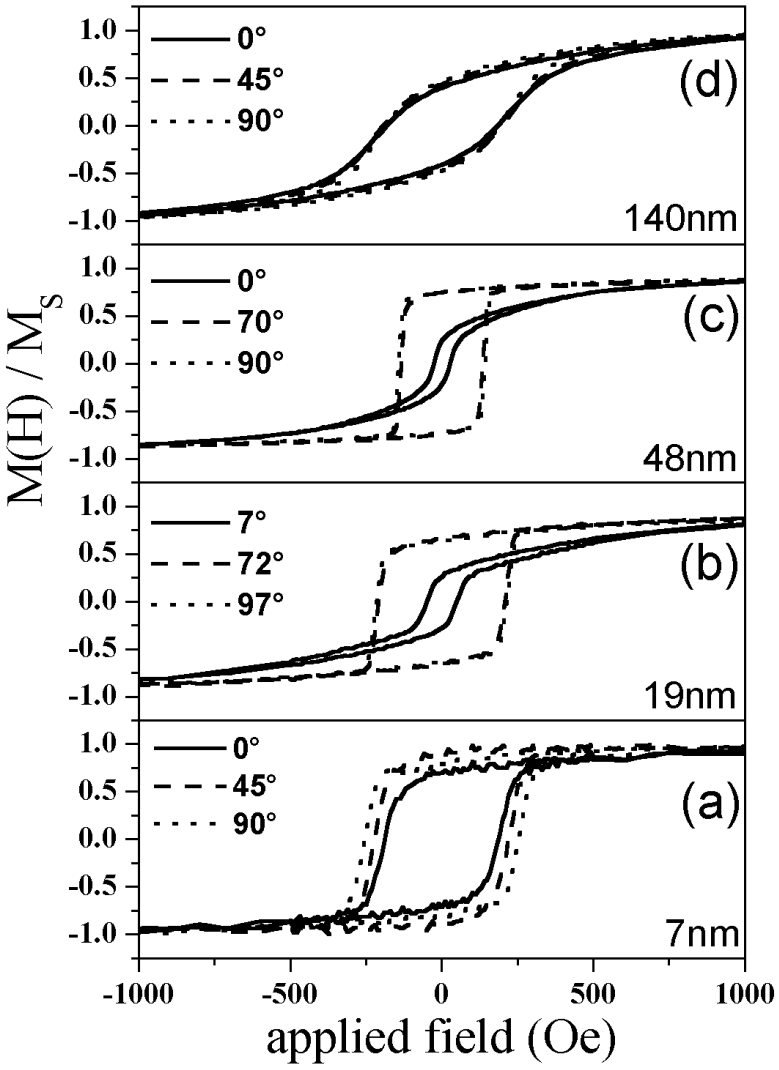

Figure 2.13. Hysteresis loops of four different Ni layers grown on GaAs(001) with thicknesses indicated in the graph. [32]

Interestingly, the Ni film in this case is in the fcc phase instead of the bcc phase previously reported. The deposition of Ni was carried out at RT and the epitaxial

relation achieved by this technique is given as Ni(001)[100]||GaAs(001)[110]. Characterized by XPS, the absence of an As peak for a 14 nm film suggests that both As segregation and As diffusion do not take place. On the other hand, the presence of the As3d peak in the 6 nm Ni film reveals the occurrence of As diffusion into the Ni layer destroying the magnetic properties of the fcc Ni film and leading to a 20% reduction of the magnetization compared to the bulk value. In the study of the evolution of interface properties of the electrodeposited Ni film upon annealing, interdiffusion between Ni and GaAs has been found not to be pronounced for annealing up to 523 K. Significant increase of As out diffusion has been observed for annealing temperatures up to 623 K accompanying a rise in Schottky barrier height which has been attributed to the Ni-Ga-As compound formation [33].

Chapter 3

Experimental Techniques

3.1 Introduction

A wide range of experimental techniques have been established and utilized to fabricate and characterize the samples studies for this project. All these techniques are found readily in York, either in the author's laboratory or in other department facilities within the university. In this chapter, we outline a detailed description of various experimental techniques that were heavily involved in this work. Chapter is organised as four main sections. The film growth techniques are firstly introduces in Section 3.2, followed by the cleanroom facilities and wafer selections in Section 3.3. Section 3.4 is devoted to the ex-situ structural characterization methods, while MOKE is emphasised in an independent Section 3.5 with in-depth explanation.

3.2 Thin Film Growth Techniques

3.2.1 Thermal Evaporator

Thermal evaporation is one of the most basic methods for thin film deposition. The evaporation principle is to heat the source material up to sufficiently high temperature to release vapour, and let it be condensed on top of a cooler and clean substrate and form a layer of thin film. The heating is usually carried out by applying a large current through a filament basket or boat, which have a certain finite resistivity. Tungsten is the most commonly used material to create filament basket, since it is chemically stable, easy to shape and stands over 3000˚C of temperature. Same as most of the resistive thermal evaporators, the one in the clean room of York University has a distance between source material and samples of over 20cm. This requires the vacuum to be good enough to form a straight line of vapour deposition. At room temperature of 25˚C, the mean free path for air is about 45cm at 10^{-4} Torr, thus the minimum pressure requirement for evaporation to take place is below 10^{-5} Torr level. Better vacuum is better for reducing contamination of the film.

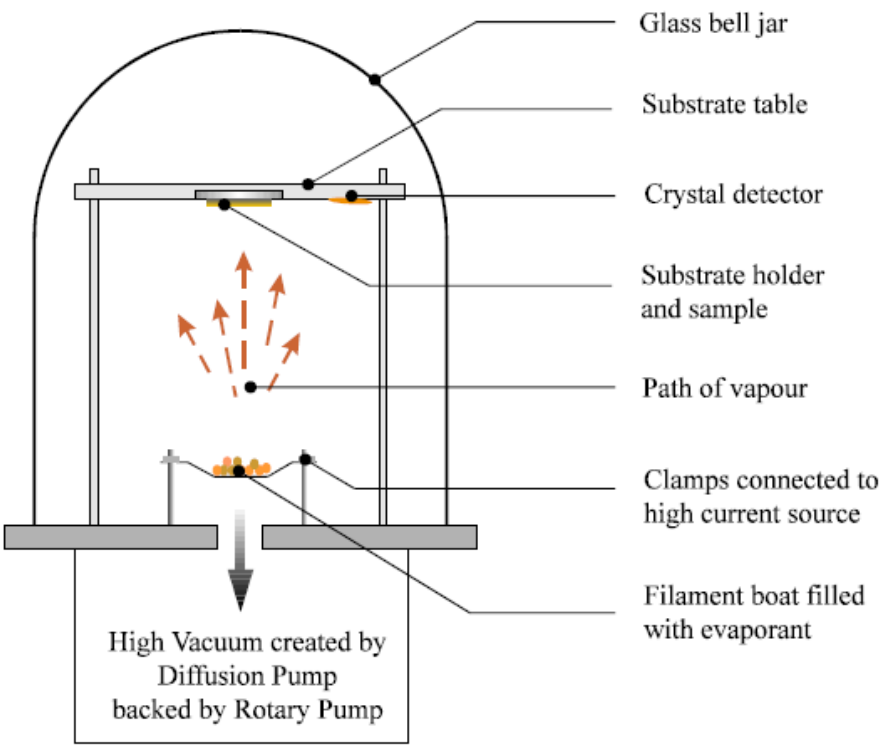

Figure 3.1. System diagram of resistive thermal evaporator. [34]

For one of the author's project, thermal evaporator was used to coat GaAs substrate samples with a thin layer of gold to isolate the surface Fe film from atmosphere environment. This layer of gold needs to be thin enough to allow post growth MOKE measurement, so the thickness was set to be at 3nm. The growth thickness was monitored by a quartz crystal rate meter. This is a commercial model, which has exclusive computer software to control the data analysing of the sensor. From the diagram above it is clearly to see that there is a distance between the position of quartz sensor and the actual position of the sample. It is important to determine the correct ratio of respective amount of deposition between these two surface, and this ratio is called tooling factor. Table 3.1 lists the determined tooling factor and other settings for gold deposition.

Source	Density(g/cm^3)	Acoustic Impedance	Tooling Factor
Gold	19.30	23.17	1.83

Table 3.1 Growth setting of gold evaporation.

3.2.2 Molecular Beam Epitaxy (MBE)

MBE can be considered as another advanced form of evaporator. One of the major differences is that MBE has a much higher vacuum requirement, usually ultra-high vacuum level, which is below 10^{-9} mbar. The source vapour is generated by heating the source material with e-beam heating filament. The filament is a twisted tungsten wire that has a large current applying across it. The source material is placed close to the filament and has a positive high voltage applied at the tip. This high potential difference would extract all free electrons generated from hot filament, causing the electron bombarding on the tip of the source material and heat it up to sublimation temperature and thus generate vapour. Same as in thermal evaporator, the source vapour would condense on the sample substrate surface but in UHV system; by reducing the growth rate to a few atom layers per minute would allow Epitaxy growth of the film, this generally means that the film would be grown with a crystallographic relationship to the substrate. The growth rate for most of the samples made by the author was about 2 ML/minute, and the background pressure inside of the growth chamber was lower than $5x10^{-10}$ mbar.

The pumping system and sealing are both very important part of building up an MBE system. Faults of either would directly cause huge impact to the vacuum quality. To achieve UHV condition, it is usually required to have at least 2 pumping stages. [35] The first stage is a normal rotary pump that has an electromagnetic motor driving fixed blade on a high speed. This pump stage draws most of the air volume out of the chamber in a relatively short time. The second stage is called turbo pump. This type of pump is usually mechanical as others but does not have a fixed blade. The blade disk is floating

inside of the pump with electromagnetic force to reduce the friction greatly, thus the rotation frequency could be as high as 1500 Hz. The total pumping capability for the MBE used by the author's project is up to 600 L/min.

A MBE growth chamber has multiple sized flange port to connect to other components such as extra chambers, evaporators, ion guns, glass view windows, manipulators and pumps. These flange ports, similar to Fig 3.2 illustrated, are in standard shape and diameter; they all have sharp knife edges along the port. These knife edges are made exclusively for the metal gaskets sealing. For UHV systems, normal plastic or rubber o-ring seal would not be sufficient enough to keep the pressure as low as 10-10mBar, instead, soft metal gaskets such as copper or aluminium were widely used to achieve higher sealing requirements.

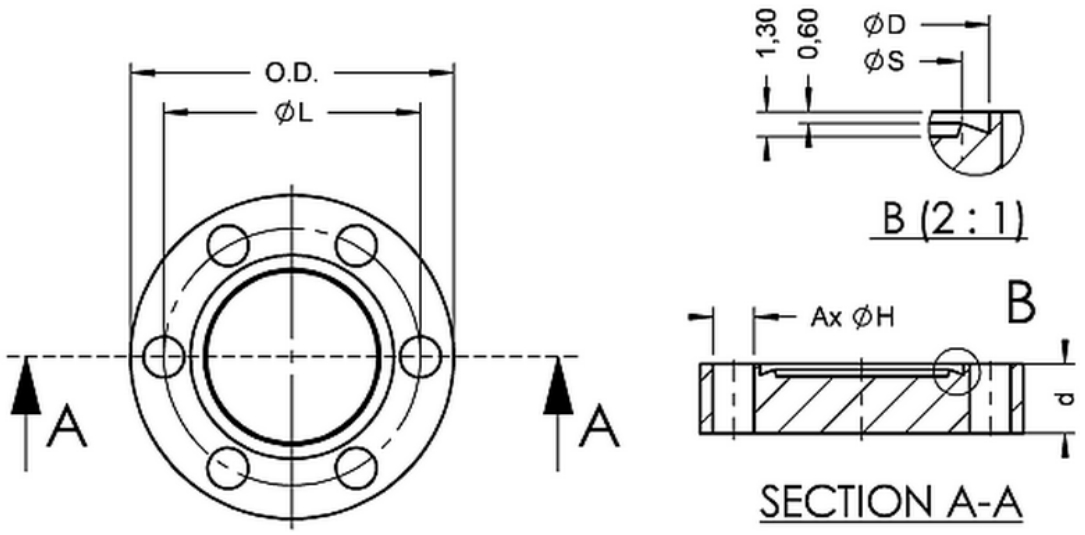

Figure 3.2. Flange CAD drawings with knife edge at top right corner.

3.3 Cleanroom Facilities

In the Department of Electronics in the University of York, sample fabrication and preparations are supported by the availability of a well-equipped class 1000 cleanroom. In this section, we introduce briefly introduce the sample preparation involved in this thesis and the selection of our substrate wafers.

3.3.1 Semiconductor Substrate Preparation

Wet bench is where chemical treatment of all samples were carried out in this project. The supply of chemicals covers a wide range. Commercial epi-ready GaAs wafers used in the later result chapters were all cleaned using a series of pre-defined chemical treatments by using a mixture of acids and other chemicals detailed in the later chapter.

3.3.2 Commercial GaAs (100) Wafers

The most commonly used wafer piece in this project is the commercially epi-ready GaAs (100). These wafers are usually purchased from Wafer Technology UK, IDB Technology and Good Fellow Ltd. When purchased, it is vital to confirm how the suppliers classify the product in terms of the substrate crystallography: EJ or US, which defines the direction of the main crystallographic axes. According to EJ definition, the major flat of the wafer refers to [0-11] axes, while [011] for US. Definition of the crystallographic directions are illustrated in Fig 3.3. For different suppliers, there could be variation of how the axis is marked. Fig 3.3 only serve for a reference purposes here.

After scribing, the substrate were chemically cleaned to remove surface contaminations including dusts, stains and particles. Detergent (RBS), acetone, iso-propanol (IPA) are used for this purposes with the help of ultrasonic cleanse. Deionized water rinsing is conducted between each step to gently remove the chemicals without introducing extra contamination.

A cleaned substrate is then ready for chemical etching, the last process technique to further remove oxidation layer of the substrate and expose the virgin layer for intrinsic chemical bonding. A wide varieties of etching solution can be found for different purposes. In this particular work, a mixture of solution comprised of H2SO4:H2O2:H2O in a ratio of 4:1:1 by volume was used. This solution was considered rather gentle for polishing and etching a very thin layer of GaAs on its surface while at the same time maintaining a relatively flat surface to allow film

deposition can be epitaxially performed. The etching time was set at 45s too just to make sure it works for the purpose and not over done it. The unavoidable surface roughness of etched substrate can be improved by in-situ annealing in the MBE chamber at high temperature. In this case 480 ˚-550 ˚for GaAs.

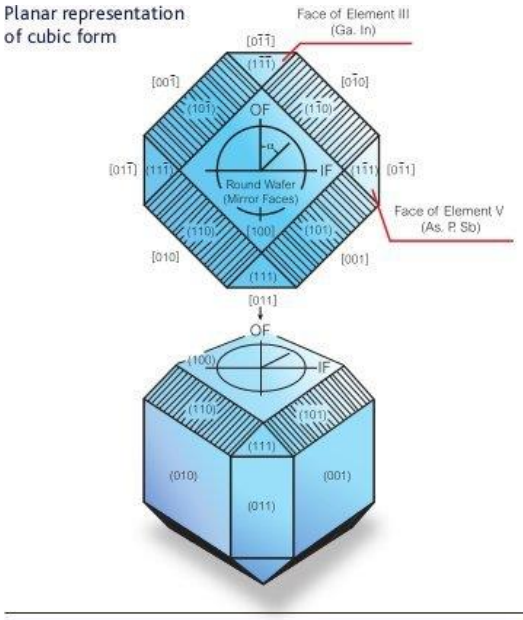

Counter Clockwise (EJ Option)			
	Off Orientation		
	General	Specific	α
Surface Orientation (100)x° off toward	nearest (110)	[1$\bar{1}$0]	45°
		[110]	225°
		[101]	135°
		[10$\bar{1}$]	315°
	nearest (111)A	[1$\bar{1}\bar{1}$] [0$\bar{1}\bar{1}$]	0°
		[111] [011]	180°
	nearest (111)B	[1$\bar{1}\bar{1}$] [0$\bar{1}\bar{1}$]	90°
		[11$\bar{1}$] [01$\bar{1}$]	270°

Counter Clockwise (US Option)			
	Off Orientation		
	General	Specific	α
Surface Orientation (100)x° off toward	nearest (110)	[10$\bar{1}$]	45°
		[101]	225°
		[1$\bar{1}$0]	135°
		[110]	315°
	nearest (111)A	[1$\bar{1}\bar{1}$] [0$\bar{1}\bar{1}$]	90°
		[111] [011]	270°
	nearest (111)B	[1$\bar{1}\bar{1}$] [0$\bar{1}\bar{1}$]	0°
		[11$\bar{1}$] [01$\bar{1}$]	180°

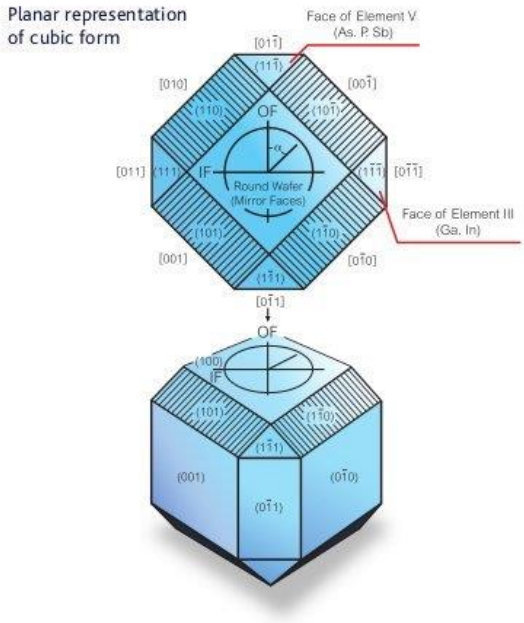

Figure 3.3. Schematic diagram of a GaAs wafer with different crystallographic direction defined with the EJ and the US option. [36]

3.4 Characterization Techniques

3.4.1 Reflection High Energy Electron Diffraction (RHEED)

Different from microscopic techniques, RHEED has much higher requirements of the vacuum system. All RHEED measurements must be conducted under UHV condition; and the image could only be observed on a fluorescent screen in a dark room. This technique is used to characterize the flatness and surface crystalline structure of sample material. Also, changes of RHEED image can be used as a confirmation or guidance of epitaxial growth of the film.

A RHEED system construction diagram is shown in Fig 3.4. It consists of an electron gun or electron source, a sample stage that is able to not only hold the sample but also rotate or tilt, and a fluorescent screen for visual observation. A CCD camera is optional for digital picture capturing. The basic working principle of RHEED is to project a beam of focused electron from a collimated electron gun, to strike the sample surface at a small angle of 1-2˚, the electrons will then be diffracted by the lattice of crystalline sample and the lattice image can then be viewed from a fluorescent screen.

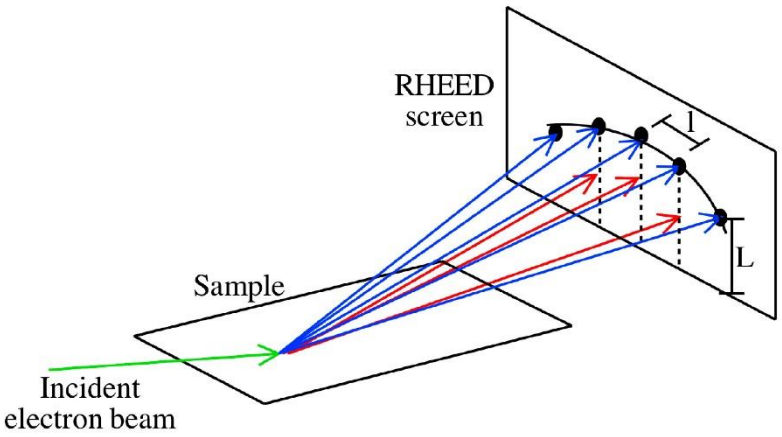

Figure 3.4. Schematic illustration of reflection high energy electron diffraction (RHEED). A high energy beam of electron impinges on the sample surface at a very small glazing angle and gets diffracted to form a diffraction pattern on a fluorescent screen. [37]

3.4.2 Scanning Electron Microscopy (SEM)

SEM is a type of electron microscopy that used widely for surface profile analysis. It scans the sample surface with high energy electron beam, those electrons interacts with atoms of the sample and the scattered electrons that carry the information about surface topography and composition.

The types of signals produced by an SEM include secondary electrons, back scattered electrons, x-ray, light, specimen current and transmitted electrons. Different of optical microscopy which uses light to view the sample, SEM has detectors for secondary electrons to generate sample surface topography image. This boosts the maximum resolution of the microscope beyond the limit of light wavelength. With larger accelerating voltage applied to electron beam, the resolution can be further increased to a few nanometres.

One of the major advantages of SEM imaging is that the analysable area of the sample can be quite big due to its large depth of field. The electromagnetic focusing lenses can be adjusted at an extremely fine level to allow precise focusing to the image. These two advantages offer to researcher more information to a certain part of the sample, and make SEM one of the most fundamental instruments for surface and material science.

There are also few disadvantages of typical SEM. Since the sample and detector were maintained at a normal vacuum chamber, with the pressure of about 10^{-5} mbar, the high energy electron beam would ionize carbohydrate floating in the air and cause carbon contamination on the sample. Also, for non-conducting material analysis, the electric charge would build up on top of the sample surface and in extreme cases making the experiment impossible. The best solution is to coat the non-conducting surface with a thin layer of carbon or conducting but chemically stable metal such as gold.

3.4.3 Atomic Force Microscopy (AFM)

The Atomic Force Microscopy is a type of scanning probe microscope that have a tip scanning across the sample surface and gather information of surface profile and generate topographical images.

The sharp tip of the AFM, held on the end of cantilever that made of silicon or silicon nitride, has a radius of curvature of a few nanometres. During AFM scanning, the tip is brought very close to the sample surface, and bended due to surface un-flatness. The bended angle was calculated by monitoring the movement of the reflection of a laser beam pointing at the end of the tip. The array of photodiode can sense the movement of the beam, and this information can be further transferred as surface topography. Fig 3.5 gives a simplified diagram of major components of a typical AFM.

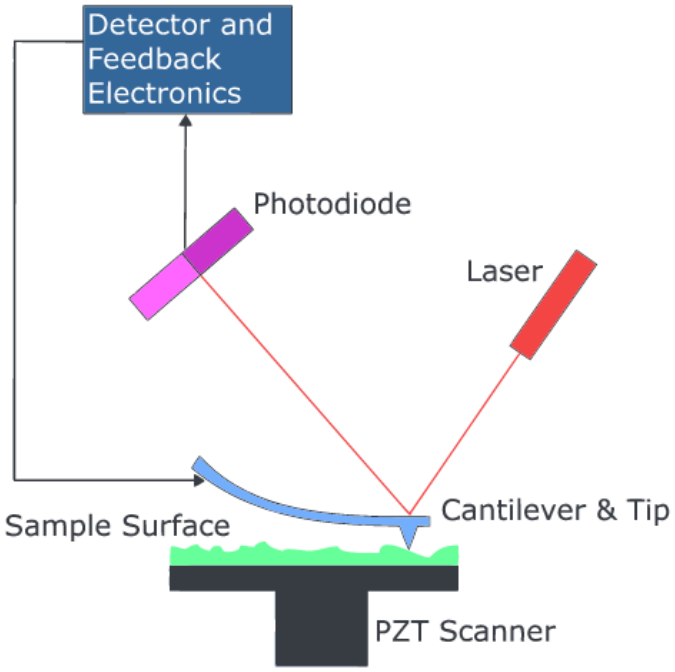

Figure 3.5. AFM schematic diagrams.

AFM usually comes with 3 different imaging modes: contact mode, non-contact mode and tapping mode. In contact mode, the less stiff cantilevers are used to reduce too much noise and drift caused by using hard cantilevers. However, the attraction force between the sample and the tip could be too strong to cause the tip snapped in the surface. Thus, a constant deflection must be maintained to ensure the total force during the scanning be repulsive.

In non-contact mode, the tip is oscillating at a frequency slightly higher than its natural resonance, as the distance between the tip and the sample surface changes, the force in between would change the oscillating frequency. This signal change is sensed by a feedback loop that then moves the position of the tip accordingly to maintain the frequency at a preset constant value. The movement distance can be used to construct the topographical image of the sample. Under this mode, there is no worry of bending the tip too much and eventually snap it and damage the sample especially when the sample is made of soft material. However, if not operated under vacuum environment, there could be a thin layer of moisture on the surface of the sample which would affect image quality of non-contact mode quite badly. However, contact mode tip would penetrate through this layer and get better signal from the surface.

The last scanning mode is called Tapping mode. In this mode, the AFM has the lowest scanning speed for same area size, the tip is oscillating above the sample at an even higher amplitude (over 10 nm), usually 100 to 200 nm. As the tip approaching to the surface, the interaction force applied to the tip would increase to reduce the amplitude of the oscillation. A feedback loop would monitor the change and control the height of the cantilever.

3.4.4 Transmission Electron Microscopy (TEM)

The TEM is the first electron microscope ever made that brakes the limit of optical light microscope and brings people to the world of nano scales.

Different from SEM generating image from secondary electrons, TEM has a much higher accelerated electron beam transmit through a very thin specimen and project onto an imaging device such as CCD camera or fluorescent screen. The biggest advantage of TEM is the extreme high resolution it could achieve. In fact, TEM is the only type of microscope that is capable of imaging single atom or atom array of examined material. This makes TEM the best instrument for surface material science as well as biological science. The detailed structure of TEM can be very complicated, thus is not discussed here. However, a general layout is illustrated in Fig 3.6.

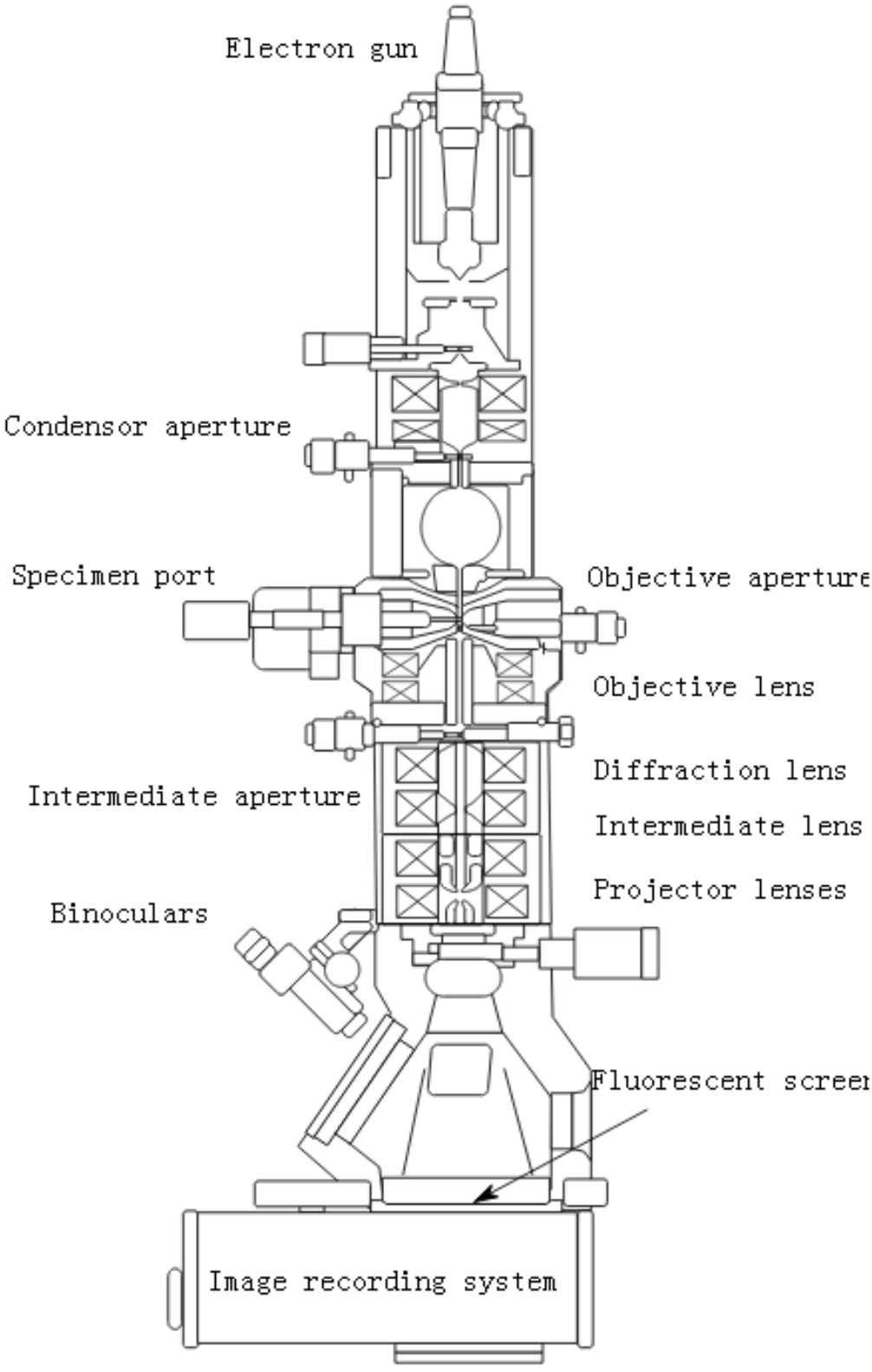

Figure 3.6. Layout of components in a basic TEM. [38]

It has been nearly a century since the first TEM was built. While the basic physical principle remains the same, the image quality has been improved dramatically. A TEM is composed of several major components, including electron source, vacuum tube, electromagnetic lenses and electrostatic aperture plates.

Electron Source is usually positioned at the top of the TEM. It is formed with a filament, a Wehnelt cap and an anode. The typical diagram can be found in Fig 3.7. The filament can be made of tungsten or LaB6, and is connected to a negative power supply. When heated up, electron beams would be pumped out from the filament surface and form electron cloud. The Wehnelt cylinder is a cap shaped metal covers the filament. As it is also heavily negative biased, the aperture in the middle can help focus electron cloud to form an electron beam with small crossover diameter. The anode plate works like an electron extractor since it is grounded or positively biased comparing to the filament. Below is a diagram for tungsten filament electron sources. LaB6 filament sources are with a slightly different design. Simply speaking it uses heating coil to heat the LaB6 rod to generate electrons. This type of filament generates more electrons at the same temperature, hence offers a brighter image at high resolution. However, the cost tends to be an order of magnitude more expensive.

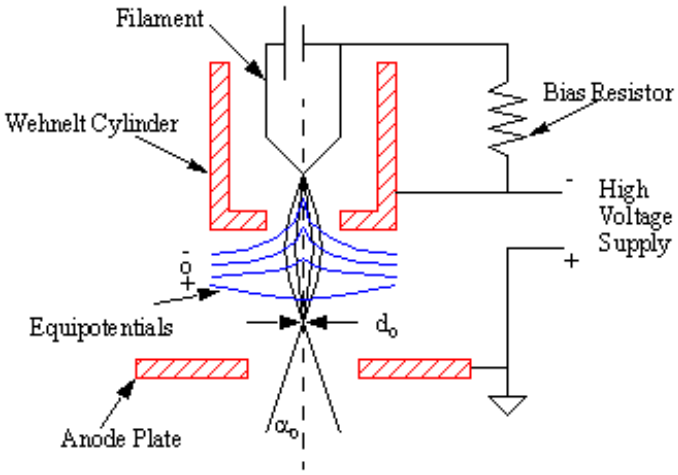

Figure 3.7. Tungsten filament electron source. [39]

Vacuum tube is made to reduce the mean free path of the electron gas interaction; good vacuum also prevent arc generated between positive anode plates to the ground. The specimen loading and unloading requires the TEM vacuum tube to have the mechanism of multi stage airlock to maintain the quality of the vacuum when replacing specimens. The vacuum level requirement mostly depends on the electron beam voltage of the TEM. High voltage TEMs generally require UHV environment to prevent electrical arc at the cathode, and sometimes has an independent pumping system for the electron gun isolated from the main tube.

Electromagnetic lenses and electrostatic apertures offers the operator fine adjustment of beam focusing and tilting. Different from optical lenses, electromagnetic lenses utilize electromagnetic coils to produce a radially symmetric magnetic field. During operation, current passing through the coils and generate quite a lot of heat. Therefore, not only these lenses must be insulated from any other component, but also have water cooling system to maintain the temperature.

3.5 Magnetic Optic Kerr Effect (MOKE)

Magneto-Optic Kerr Effect (MOKE) is a type of magnetometer that observes the optical reflection on a static magnetic material, traces the polarization rotation as a function of the varying magnetic field applied, and plot the hysteresis loop as the output for further studies.

3.5.1 Origin of MOKE

In1877, J.Kerr found a physical phenomenon about the relationship between magnetic materials and polarized light. He reported that if a beam of plane polarized light is probed onto the surface of a magnetized material; the reflection of that beam will have its polarization plane slightly rotated. And the magnitude of rotation is proportional to the magnetization of the material surface. [40]

3.5.2 Physical Expression of MOKE

To understand the physics behind Kerr effect, it's better to start with the nature of light. A beam of light is a form of propagating electromagnetic wave that has both an electric and a magnetic field. A linearly polarized light is the vector combination of left and right circularly polarized lights. When interacting with a magnetic medium, due to the difference of refractive index, the phase velocity of both left and right circularly polarized lights is changed. Assuming there is no absorption in this case, their combined vector, the linearly polarized light, will have its polarization angle rotated by a certain degree, while the amplitude stays the same as there is no absorption. This rotation is called MOKE rotation.

On the other hand, consider the absorption of the incident beam when passing through different mediums, the two circularly polarizations would experience different amount of absorption or scattering, and their relative amplitude changes along. When these two reduced amplitude vectors are combined, they would form a linear polarization with an ellipse.

In actual cases, the refractive index of any material has a real part and an imaginary part called the extinction coefficient. A complete form of complex refractive index can be expressed as:

$$\tilde{n} = n + ik \tag{3.1}$$

where n indicates the reduction of speed when light travels through different materials, and k represents a measurement of scatter and absorption of electromagnetic radiation. Unlike the real part affects the phase velocity of light, the extinction coefficient affects

the amplitude vectors. Thus the combination of the two would exhibit both rotation and ellipticity behaviour.

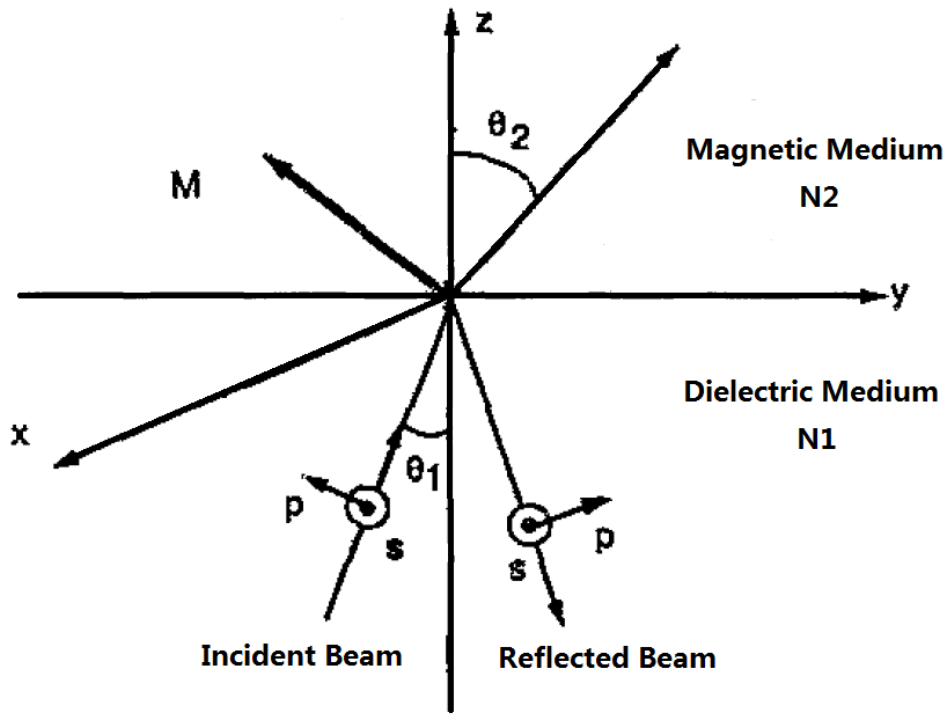

Figure 3.8. Geometry of Kerr effect. Plane xy is the sample plane, perpendicular to the plane of incidence; yz is parallel to the plane of incidence but normal to the material surface. ϑ1 is the incident beam angle, symmetrical as the reflective beam angle.ϑ2 is the generalization to complex numbers of the angle of refraction. M is the magnetization direction.

The permittivity tensor transformed into the above coordinate system for the orientation of magnetization M can be written as

$$\varepsilon = \varepsilon_q \begin{bmatrix} 1 & -iQm_z & iQm_y \\ iQm_z & 1 & -iQm_x \\ -iQm_y & iQm_x & 1 \end{bmatrix}$$

(3.2)

Where Q is the complex magneto-optical constant, m_x, m_y and m_z are the magnetization components along x, y and z axis respectively.

Since the incident beam is linearly polarized, it is defined that if the polarization plane is parallel to the plane of incidence, the light beam is p-polarized; if the polarization plane is perpendicular to the plane of incidence, it's called s-polarized. The Fresnel reflection coefficients are given as

$$r_{ps} = -\frac{i\mu_1\mu_2 N_1 N_2 \cos\theta_1 \left(m_y \sin\theta_2 + m_z \cos\theta_2\right) Q}{(\mu_1 N_2 \cos\theta_1 + \mu_2 N_1 \cos\theta_2)(\mu_2 N_1 \cos\theta_1 + \mu_1 N_2 \cos\theta_2)\cos\theta_2}$$

(3.3)

$$r_{ss} = \frac{\mu_2 N_1 \cos\theta_1 - \mu_1 N_2 \cos\theta_2}{\mu_2 N_1 \cos\theta_1 + \mu_1 N_2 \cos\theta_2}$$

(3.4)

$$r_{pp} = \frac{\mu_1 N_2 \cos\theta_1 - \mu_2 N_1 \cos\theta_2}{\mu_1 N_2 \cos\theta_1 + \mu_2 N_1 \cos\theta_2} + \frac{2i\mu_1\mu_2 N_1 N_2 \cos\theta_1 \sin\theta_2 \, m_x Q}{\mu_1 N_2 \cos\theta_1 + \mu_2 N_1 \cos\theta_2}$$

(3.5)

$$r_{sp} = -\frac{i\mu_1\mu_2 N_1 N_2 \cos\theta_1 \left(m_y \sin\theta_2 - m_z \cos\theta_2\right) Q}{(\mu_1 N_2 \cos\theta_1 + \mu_2 N_1 \cos\theta_2)(\mu_2 N_1 \cos\theta_1 + \mu_1 N_2 \cos\theta_2)\cos\theta_2}$$

(3.6)

Where $r_{pp}, r_{ps}, r_{ss}, r_{sp}$ are the magneto-optical Kerr effect reflection coefficients; and the subscripts denote the scattering plane dependence of each element. For example,

r_{ps} describes the ratio between the complex electric field amplitude of p-polarized reflected light and that of s-polarized incident light.

3.5.3 MOKE Configurations

There are commonly three types of arrangements to set up an optical system for MOKE observation. They are defined by the measurements of magnetization components with the respect of the plane of incidence.

Polar effect

Polar MOKE measures the magnetization component vector perpendicular to the reflecting surface plane, but parallel to the plane of incidence. The Polar is the only geometry that MOKE can be observed and studied at near-normal angles of incidence and reflection to the reflecting surface. Generally, it provides the largest rotation angle, thus the strongest signal. But it's not popular for thin film research applications; considering that it requires a considerably large external field to fully saturate the films out of the plane.

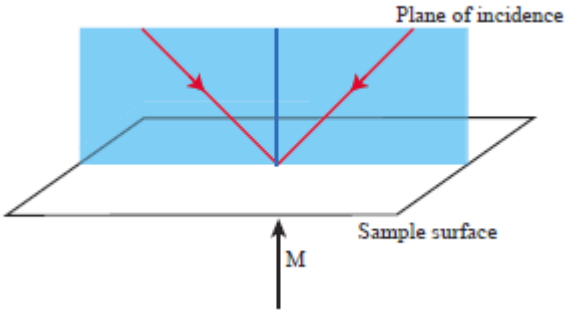

Figure 3.9. Polar MOKE Arrangement.

Longitudinal effect

Unlike the previous arrangement, longitudinal MOKE has the magnetic field applied in the same plane of the reflecting surface, and measures the components within the plane parallel to the sample surface. It usually requires a pair of magnets with the opposite poles facing each other in order to generate strong and unified field. This arrangement is more welcome for thin film studies, mostly because the saturation field is comparably smaller across the film surface.

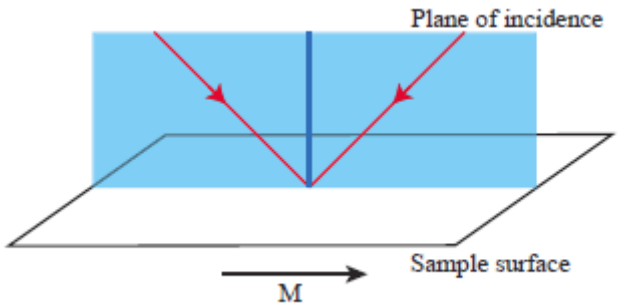

Figure 3.10. Longitudinal MOKE Arrangement.

Transverse effect

For the transverse MOKE set up, the magnetic field is applied perpendicularly to the plane of incidence. This configuration measures the reflectivity change which is proportional to the change of magnetization components within the plane of reflectivity but normal to the plane of incidence.

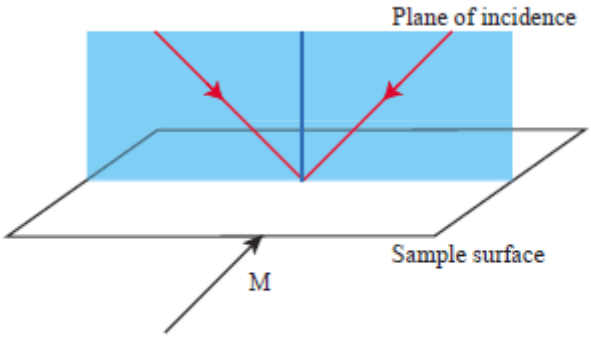

Figure 3.11. Transverse MOKE Arrangement.

3.5.4 Laboratory in-situ MOKE Setup

In order to detect the changes of polarization of the light, a pair of polarizers that are adjusted to be nearly perpendicular to each other is positioned on the light path. The first linear polarizer limits the polarization of the incident beam to one direction only, allows the beam to hit on the magnetic medium and interact with the electric field in the atoms. A polarization component that is perpendicular to the polarization direction is generated and reflected to the second polarizer. This polarizer attenuates the original polarization component of the incident beam to the minimum, while allowing the component generated through the magneto-Kerr effect to pass to the detector.

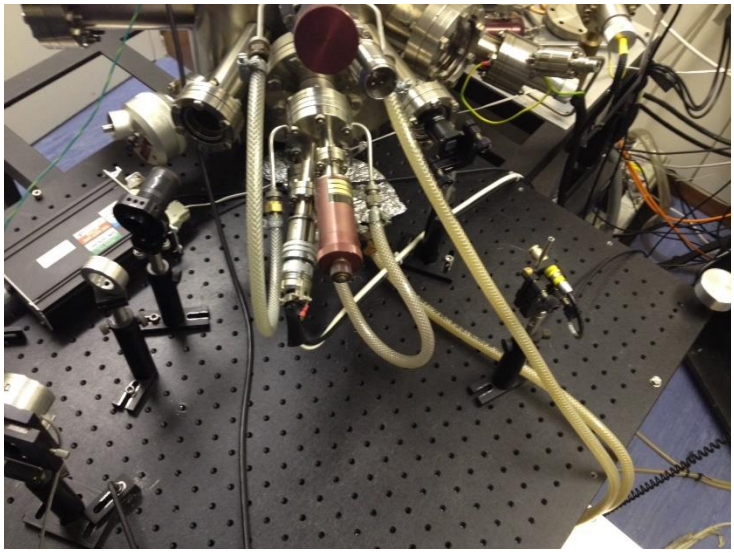

Figure 3.12. In-situ MOKE lab setup.

For the in-situ MOKE application in the lab, a diode laser with 670 nm wavelength and output energy of 5mW is used as the light source. The polarizer and the cross analyser offers up to 10^{-7} of the extinguish ratio. The detector is powered by a pair of 9-volt batteries, and connected to the computer through NI Labview ports.

Such MOKE setup can be then extended to the MBE growth chamber, working with the magnet built inside, form a fully functional in-situ MOKE as shown in Fig 3.12. Comparing to ex-situ measurements, in-situ MOKE allow the target material to stay within UHV environment throughout the measurement process, thus preserve its intrinsic properties and remove any impact from anti-oxidation coating layers.

The performance of the in-situ MOKE has a few limits, one of which is the inconveniences of manipulation of the sample. Without direct control and adjustment by bear hands, it is required to use wobble stick to reach into the centre of the chamber to adjust the target sample to the desired position. Such operation is heavily restrained by the free movement range of the wobble stick. The other trouble that could make negative impact to the measurement is the vibration. Since the sample is sit on the bottom tip of the manipulator, mechanical vibrations conducted through the chamber may affect the stability of the sample. This can be vital to some of the measurements when the film is very thin and the magnetic properties signal is really weak. Improved isolation of vibration source could be helpful in this situation.

Chapter 4

Artemis Project

4.1 Introduction

The Artemis Project was taken place at the well-known Rutherford Appleton Laboratory, in the ultra-fast laser station Artemis. The project was initialized based on the interests on the microscopic origin and mechanisms of laser induced ultrafast demagnetization.

My role in this very first beam time project at the Artemis facility was in both instrumentation and characterization. I was in charge of the assembly of a new MBE chamber to be attached to the main characterization chamber and taking part in setting up an in-situ time-resolved magneto optical Kerr system alongside with the time-resolved photoemission spectroscopy. I have done the MBE growth and then performed time-resolved photoemission spectroscopy of the single-crystal Fe thin films. I have taken part in the time-resolved in-situ MOKE measurements on these single-crystal Fe thin-films. I have also performed the static MOKE and AFM measurements for these Fe thin films to confirm the single-crystal growth and the thickness calibration. In TR-MOKE data, an ultrafast rise in the reflectivity shows the electron temperature reaches its maximum around 300fs after laser excitation, which leads to a demagnetisation

maximum about 100 fs later the peak electron temperature. In photoemission measurements, a profound space discharge effect was presented due to the high intensity of both pump and probe pulses, which distorted the photoemission signals. By summing up the total photoelectron counts over a fixed energy window just below the Fermi level at each delay time after the pump pulse excitation, though the signal was very noisy, we could observe a trend of increasing in the counts after zero delay.

4.2 Artemis Facilities

Artemis is the code name of the CLF's ultrafast laser and XUV lab. It is based on ultrafast laser technology to bring together tuneable pulses across a wavelength range spanning the ultraviolet to the far infrared, few-cycle pulses at 800nm, and ultrafast XUV pulses produced through high harmonic generation. Vacuum beamline deliver the synchronized XUV pulses to the end-stations equipped with spectroscopic tools for time-resolved spectroscopic studies in condensed matter physics and gas-phase chemistry. It has been developed as a centralized facility with the aim to facilitate UK and European researches into the ultrafast science.

The fundamental technique exploited on the Artemis material end station is time- and angle-resolved photoemission spectroscopy, which enables the electronic structure of a material to be monitored as it responds to excitation by a laser pulse. In most of the cases, the target material is irradiated by a short laser pulse that induces structural/property changes. Such transient change could to be observed and analysed using another beam called a probe beam which in this case is the XUV beam line. The XUV pulse generates photoelectrons with information on the direction, speed and scattering process of valence electrons in the sample being studied. The XUV pulses are synchronized to the pump beam pulse and the photoemission spectrum are accumulated at a series of time delays between the pump and the probe, allowing time-resolved spectroscopic data collection being taken place and the temporal profile of the electronic structure of the sample surface after laser excitation being analysed afterwards. The major advantages of Artemis station comparing with other similar

facilities is that it uses ultrafast XUV pulses in the 10-100 eV energy range from high-order laser harmonics for photoemission. The higher photon energy enables electrons with a much wider range of energy and momentum space to be detected, meaning that each snapshot of electronic structure has a wider field of view. Furthermore the naturally synchronized ultra-short XUV pulses with high photo flux provide a unique tool to resolve structural/property dynamics in both solid, liquid, or gas phases.

The lab facilities can be divided into three major parts. The MBE and Material Science Station, Laser beamline and XUV generator. In this section, the functionalities of each and how they are connected to each other will be explained in detail, assisted with mechanical diagrams for illustration purposes.

4.2.1 MBE

As the supply end of the lab, MBE chamber is the source of loading and producing target samples. It allows operators to create customized samples in UHV environment when needed and transfer virgin samples to the Material Science Station for further analysis. This continuous UHV environment greatly preserves the initial state of the material, and minimizes any contamination from floating particles in less vacuum space. For semiconductor and magnetic materials, it prevents surface being oxidized as much as possible and thus offers researchers extensive amount of time for data collection, which can be extremely valuable on photoemission or any surface-sensitive measurements.

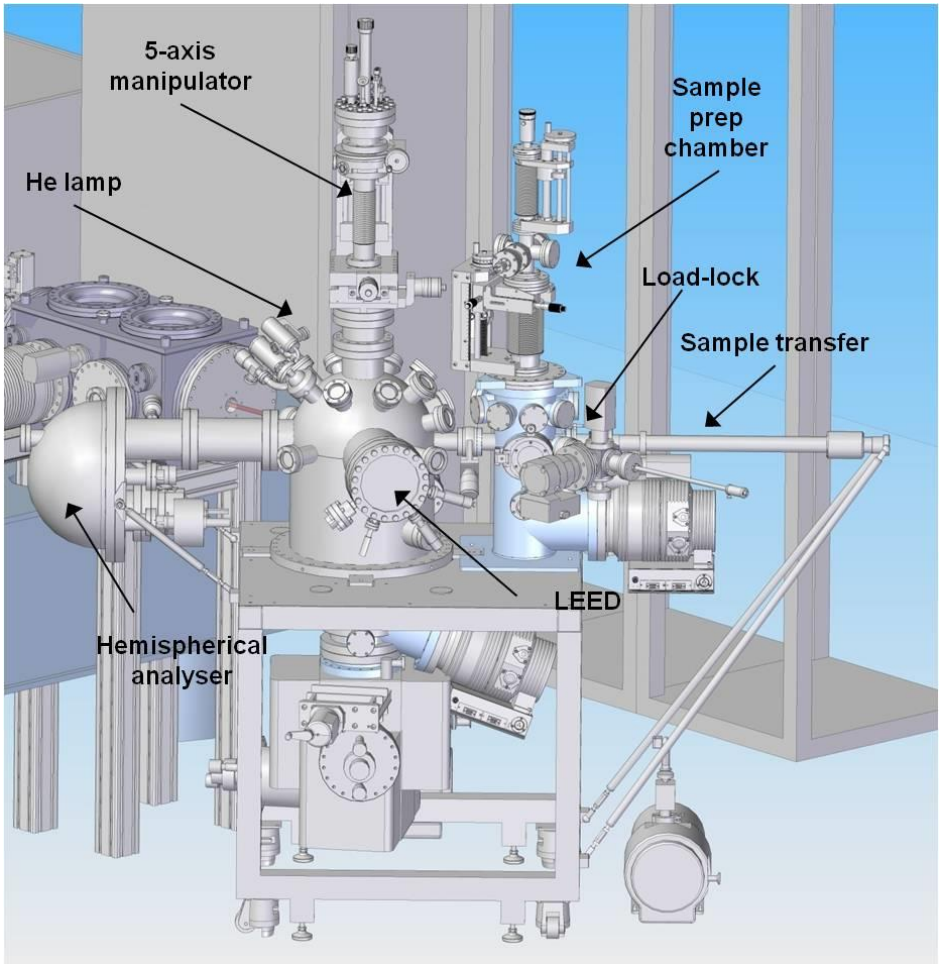

Figure 4.1. Mechanical diagram of MBE and MSS.

The above diagrams shows the major components of MBE and MSS. Starting from the right end, a piece of sample or sample substrate can be attached to the end of transfer arm in the load-lock. This small chamber is designed to be small and as a buffer between atmosphere and UHV. A small turbo pump with a rotary pump is connected to produce vacuums as low as 10E-8mbar. The average pumping down time is less than 1 hour. When the load-lock pressure is reaching to the limit, a gate valve that separates it to the MBE chamber will open to allow sample transfer being conducted. The sample will be caught by the manipulator that offers 5-axis movement (azimuthal and polar angles). Sample then can be produced in the MBE under the base pressure of 2x10E-10 mbar.

Same method can be performed again to transfer the sample into MSS chamber which is also separated by a gate valve. The MSS chamber is the place where sample will be analysed, thus it is connected with several analysing equipment.

First of all, the chamber has a 3-level pumping system. A high-speed rotation pump as backing pump that draws 1.5m3 of air per hour; a large scale turbo pump that operates at the rotation speed of 60000 per minute; and a cubic ion pump that exploits Titanium ions to attract floating particles and further push the vacuum level down to low 10^{-11} mbar.

Secondly, the manipulator that catches the sample not only has the same 5-axis movement to allow orientation the sample crystalline axis with the measurement plane, it also has a coolant tube that cools the sample to 14K and an e-beam heater that heats it to 1000K. This allows any temperature control within the range being possible and subsequently any temperature dependency measurements.

A LEED port is designed to make it possible to study the structure and symmetry of sample surfaces. It generates a beam of electrons of well-defined low energy that

incident normally on the sample surface. A back-scattered electron beam was then generated and reflected to the florescent screen to create a diffraction pattern. The low energy beam is preferred at this state to minimize the bombarding damage to the sample.

Lastly, the photoemission measurements is carried out in this chamber. A hemispherical electron analyser (SPECS Phoibos 100) is connected to the left end of the station. The energy- and angle-resolved measurements are performed with a 2-dimentional CCD detector, achieving an ultimate energy resolution of ~5meV and angular resolution of <1 °. In practice, the energy resolution is set at 130meV, limited by the bandwidth of the XUV harmonic generated with a 30fs pulse.

4.2.2 Laser Beamline

The Artemis lab provides three ultrafast, synchronized laser beamlines which can be configured flexibly either to generate XUV or as pump and probe pulses spanning the UV to far infrared spectrum.

A Ti: Sapphire CPA system operating at the wavelength of 785nm is the core system of the laser beamline. It generates a pulse of 30fs, a repetition rate of 1 kHz and a maximum energy of 14mJ/pulse. Two grating compressors are implemented to allow the pulse durations of pump and probe beams being adjusted independently. The output energy can also be used to drive a widely tuneable optical parametric amplifier system, which provides 30-100fs pulses spanning the spectral range from 230nm to 20um. A split part of the output energy can be guided into a gas-filled hollow fibre and recompressed to produce pulses down to 7fs with energies of 0.5mJ.

4.2.3 XUV Generator

The XUV is produced through high harmonic generation in an Argon gas target. The laser is firstly focused to an intensity of ~10^{14}Wcm^{-2} in a gas-jet and only about 1 in 10^6 of the energy is converted to short pulses of XUV radiation in the 10-100nm range. The XUV pulses should have the same pulse duration to the source pulse and are then synchronised with sub-fs resolution. Performance-wise, the conversion efficiency is of 10^{-6} at 30eV, and a photon flux of ~10^{11}/s per harmonic can be achieved.

There are two XUV beamlines in Artemis, one for monochromatised XUV pulses and the other for broadband XUV radiation.

In the monochromatised beamline, the harmonics pass through a specially designed XUV monochromator which enables one single harmonic to be selected from the entire spectrum without changing the pulse duration of the beam.

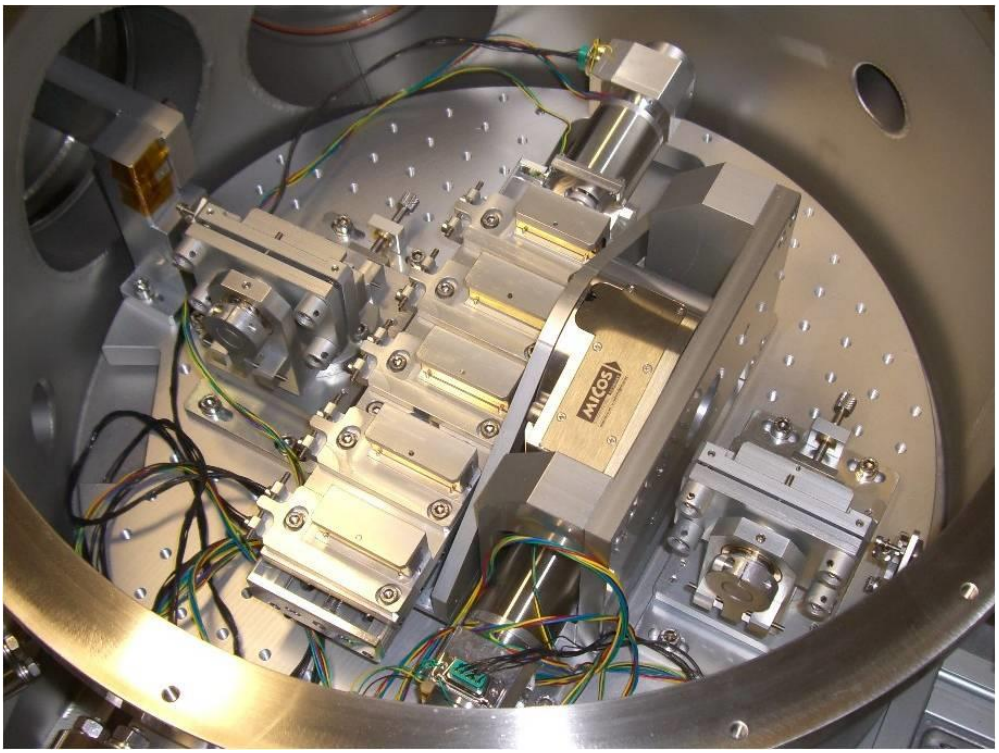

Figure 4.2 Inside structure of monochromator.

The monochromator has been designed to have four interchangeable diffraction gratings to cover the spectral range of 12-30nm with higher resolving power, or 30-90nm with shorter pulse duration. The peak transmission of the monochromator is measured as 30%, and the XUV flux after is up to $1.6x10^{10}$ photon/s in the 21^{st} harmonic (38nm), which also corresponds to an XUV energy of 80pJ/pulse.

The XUV pulses require to be refocused into the MSS chamber, and this was performed using a gold-coated toroidal mirror at grazing incidence. The toroidal mirror chamber also has another set of mirrors that combines the XUV with the laser pulses for pump-probe experiments.

The identical toroidal mirror can also image the XUV generation region to the interaction region in the MSS station and create the second XUV line without a monochromator. A flat-field spectrometer captures the HHG spectrum of 10-45nm in a single image. The advantages of this line is that the wavelength selection is only provided by filtering but not monochromator. This offers more flexibility in configuring the XUV generation condition and allows higher pulse energy being achieved.

4.3.4 TR-MOKE

TR-MOKE, also known as time-resolved MOKE, is an advanced measuring technique designed to capture the change in magnetization in a dynamic switching process. It is established based on the combination of pump-probe technique with traditional MOKE system. Instead of initializing the magnetization switching through external field, an ultrafast pulsed laser is introduced as the pump source that excites the sample, generating a non-equilibrium state. Another laser pulse, spited from the same source but with reduced power, acts as a probe to detect the change in magnetization by monitoring the pump-induced changes in the optical constants. The result plotted as a function of time delay between the arrival of pump and probe pulses contains information about the relaxation of electronic state in the sample.

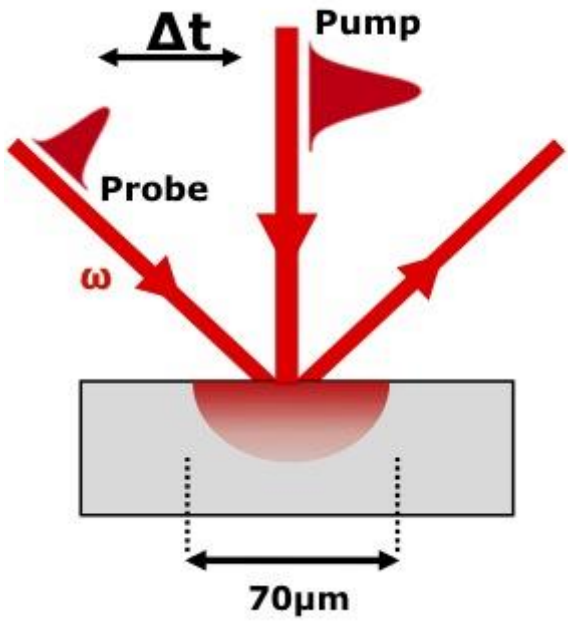

Fig 4.3. Simplified pump-probe diagram

In Artemis, the laser probe beam for TR-MOKE measurements was the same 30fs laser pulses used for XUV generation. However, the frequency was doubled to allow the noise from the scattered 800nm pump beam to be eliminated in the MOKE signal detection via a 400nm narrow-band filter. The 400nm probe beam (blue line) was linearly p-polarised and propagated along the same optical path as the XUV beam. It was focused by a toroidal mirror in the "Toroidal Mirror Chamber" placed right before the measurement chamber. The pump beam (red line) was focused by a 100cm lens before being directed to the D-shaped mirror (half mirror, half hollow) in the same chamber. The probe beam instead, passes through the hollow half of the mirror, and then travels in parallel with the pump beam. These two beams therefore became collinear and illuminate the sample at the same spot with an incident angle of 45º.

It is critical to ensure the overlapping of two laser beams on the sample. Before sending the sample to the measurement chamber, a pick-up mirror was rolled to the equivalent position as that of the real sample, which guides the reflection light to a CCD camera. A direct view was then possible to check the incident positions of both the laser beams. After adjusting the beams to overlap perfectly, the pick-up mirror was withdrawn and replaced by the real sample.

The reflected pump beam from the sample should be blocked as it has no other use. On the other hand, the reflected probe beam contains the information of the magnetization switching, and was filtered by a 400nm narrow-band filter to eliminate the scattered 800nm pump beam before being collected by an optical bridge detector. The bridge-detector consists a Wollaston prism, which splits the incoming probe beam into two linearly-polarised components in the orthogonal directions. The intensities of these two components are measured by two identical photodiodes respectively. The difference

between the two signals gives the Kerr rotation in the reflection of probe beam, while the sum provides the reflectivity.

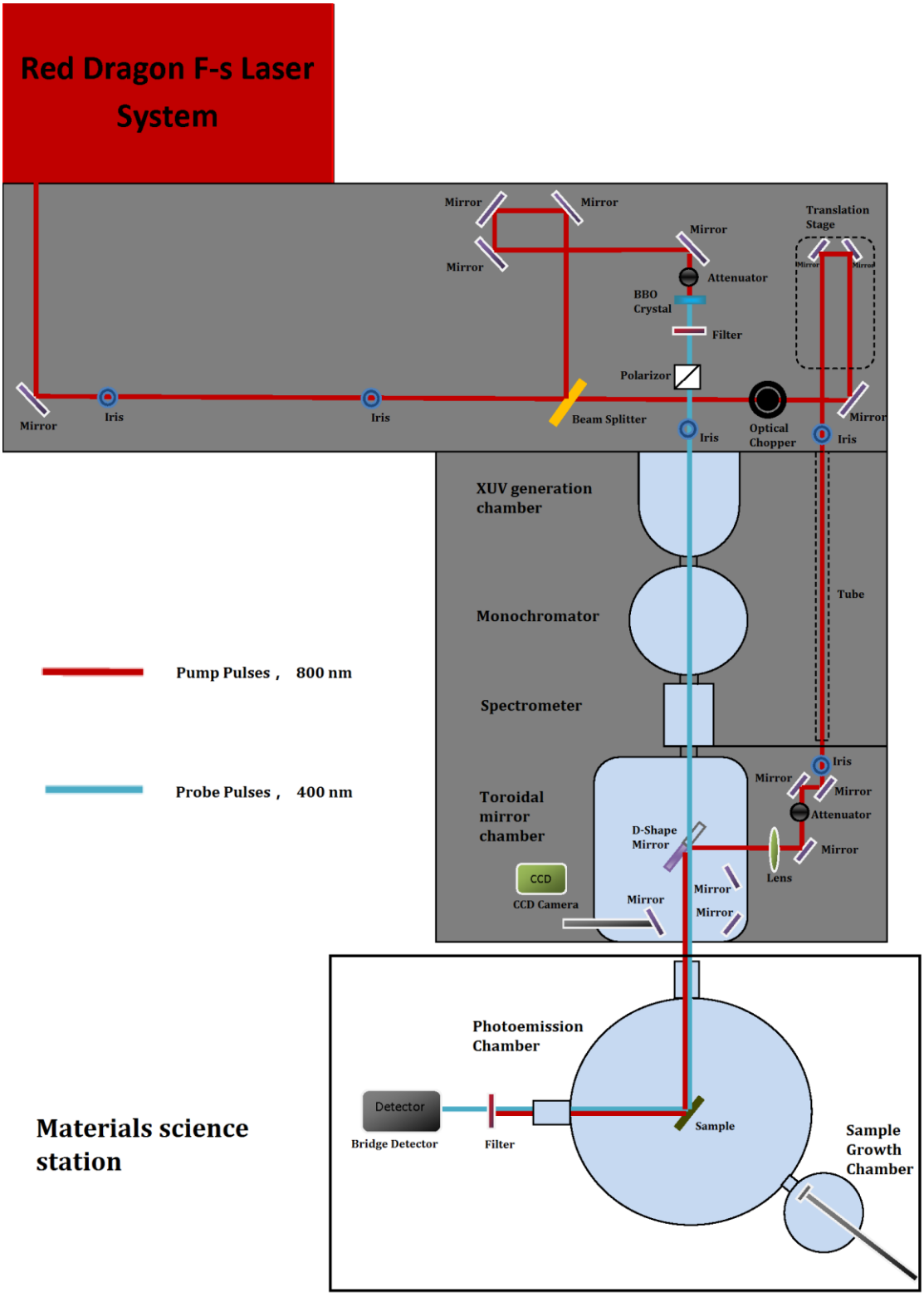

Fig 4.4. Schematic Drawing of Optical Pump-Probe Time-resolved in-situ MOKE system.

4.3 MBE System Build-up

4.3.1 System Components

The MBE system is a small chamber attached to the original photoemission measurement chamber in Artemis laboratory. The chamber has 4 layers of construction. Down at the bottom it is the pumping port. A Pfeiffer Vacuum turbo pump is attached on this port and have a backup rotary pump connected to the gas outlet. This pump is the best model of its size; the highest rotary speed is 1500 Hz, which offers over 600 L/min of pumping volume. A small burst disk is attached next to the pumping port to protect the mechanical constructs especially rotary blades inside of the pump.

Higher up there is a layer of ports designed for sample transport. An extended CF40 port is aligned to the gate valve between growth chamber and main chamber, and has an extended manipulator attached to it. Around this port, there are 3 CF40 and 2 CF63 ports available for mounting pressure gauge and view port windows. Since sample transport is completely manual operation without breaking the vacuum, it is all about precision. For this matter, the design was modified to ensure that there are at least 2 view ports from different angles at each stage of sample transport processes.

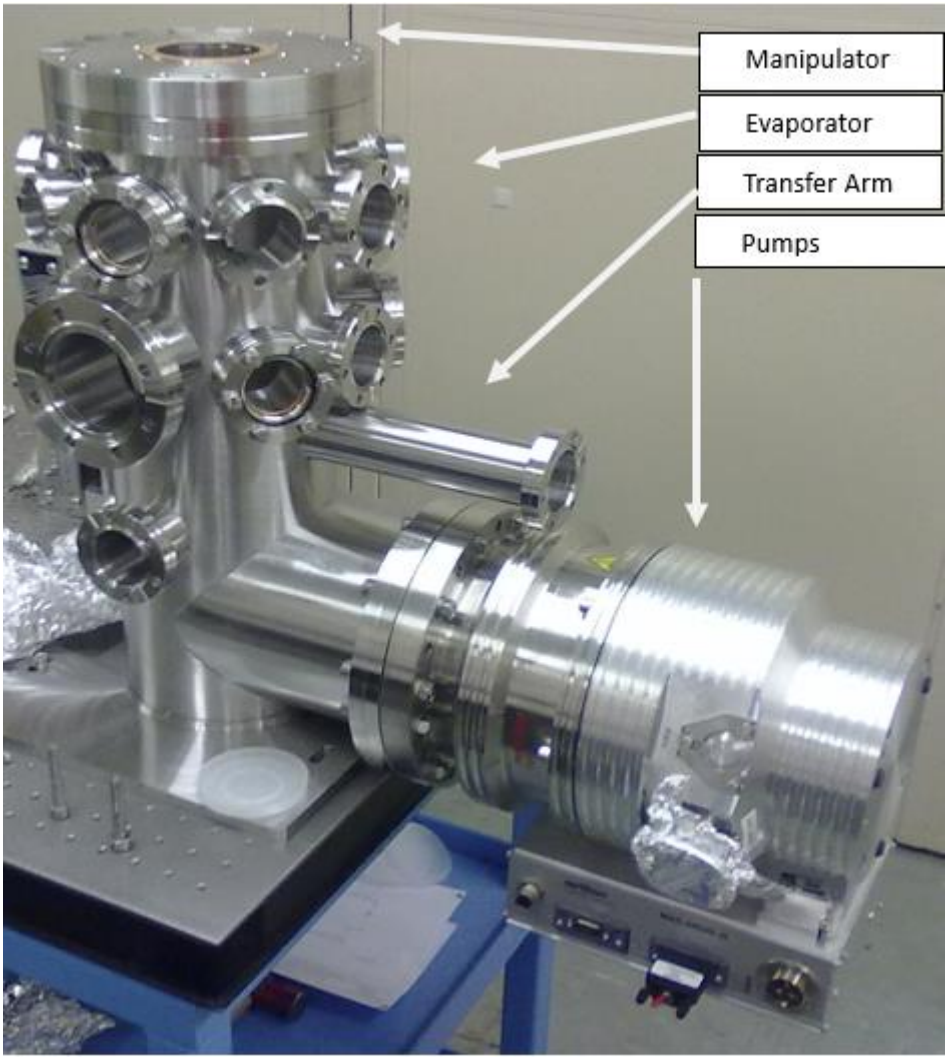

Figure 4.5. Growth Chamber.

Close to the top there is a circle of 9 CF40 flange ports built around the chamber's neck. This is the layer where all growth components are mounted. For the beam time, we used 6 of these ports, 2 for e-beam evaporators, 1 for ion sputtering gun, 1 for load lock chamber, and 2 for view port windows. The rest was sealed with blank steal flanges. Instead mounting all the above components next to each other, we chose to mount them separately. This not only formed a better layout for cable connection and system operation, but also allowed us to have view port at two very different angles to cancel visual aiming error during sample transport. The only problem for this set up is that the ion sputtering gun is facing opposite to both e-beam evaporators. It is very likely that small amounts of material vapour deposit on the ion gun filament and cause a potential of short circuitry. Also the material deposit on other mechanism in the ion sputtering gun could contaminate the equipment badly and causing unexpected problems. To avoid any hazards from happening, we have implemented a gate valve blocking in front of the ion gun head. This valve should always be closed to prevent ion gun from being contaminated, and it reduces the total volume and surface area of growth chamber, which has evidently positive effect to the chamber pressure.

Up on the very top of the chamber there is one big port facing upwards for main manipulator. The manipulator is connected to the sample stage through a long and straight aluminium stick. This offers sample manipulation along three axis and rotation around Z axis. All these movements are implemented by two manipulator stages. The lower stage is heavier and robust; it sits between the chamber and top stage, offers 40 mm of vertical stroke, and 15 mm of movement horizontally. This stage also has two

micrometre to indicate movement distance along x and y axis, making it extremely precise for fine adjustment.

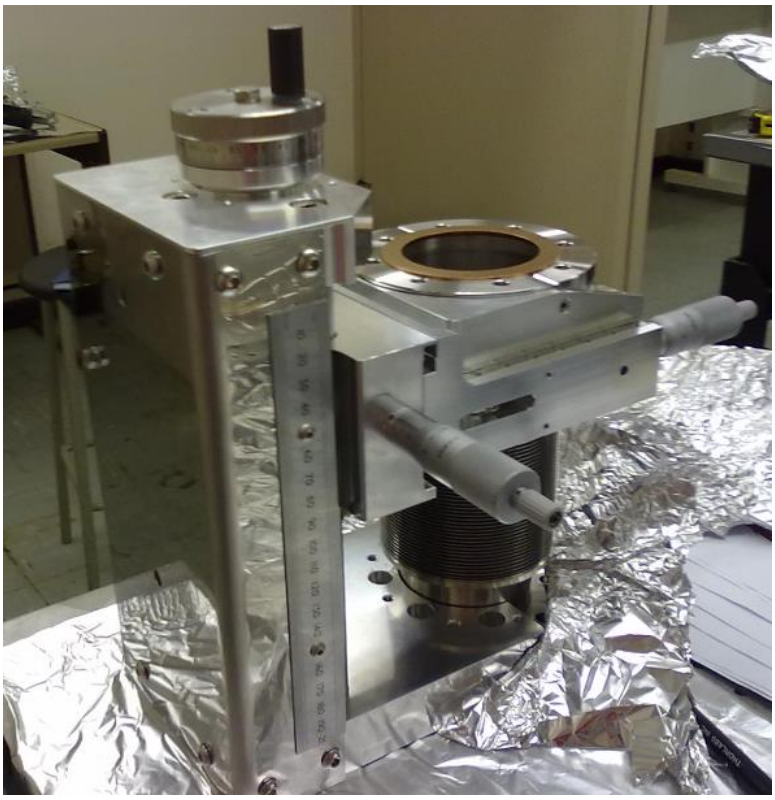

Figure 4.6. Lower Manipulator Stage.

The top stage has longer vertical stroke, and a precise rotary drive connected to the manipulator arm. It offers 360˚ free rotation with indication, mechanical lock, and 100 mm stroke.

Figure 4.7. Higher Manipulator stage.

There are totally 4 CF40 flange port on the neck of manipulator. They are working as electrical connection feedthrough to the sample stage. For the Artemis beam time project, only 3 of these ports were used, one for high voltage supply on sample stage, one for quartz thickness monitor, and one for e-beam heating filament current supply and thermal couple connectors. All cables connect to these feedthrough were safely insulated from each other, and carefully bind to prevent tangling problem inside the vacuum chamber.

The sample stage is mounted at the end of manipulator arm. This stage offers various mechanisms for sample plate mounting and connections. This stage could also be disassembled into 3 parts.

Figure 4.8. Sample Stage.

The upper layer is mainly a square slot for sample plate, two steel springs for stabilization. The screws to hold these springs could also be used for high voltage supply and thermal couple wires since they are very close to sample plate and have good contact to it. This layer is mounted using 4 other screws which have MACOR

ceramic insulator pieces. This type of ceramic is widely used in high vacuum and ultra-high vacuum systems. It is much more robust than other similar products, machinable with normal metal tools, does not have any degassing problem and can stand very high temperature of up to 1000˚C. The main body of sample stage holds the connectors for e-beam heating filament. This filament is made of 99.9% pure tungsten with diameter of 0.15mm. From our test it can easily stand 3A of DC current without breaking. The filament itself was mounted to two screws and adjusted to be close to the sample plate as possible; the current connections were attached on the back of sample stage, with good ceramic insulation. Next to the sample plate there is a stage for quartz microbalance. This microbalance is used to monitor the thickness and deposition rate of thin film. It is positioned very close to the sample, has good stability and protected with a thin piece of ceramic too.

Load lock chamber works as a vacuum buffer between UHV and atmosphere environment. This chamber is tiny compare with the growth chamber, thus it has much smaller venting volume and is easy to be pumped down to good vacuum. For this system, the load lock is attached on the same stage layer as the evaporators and has a gate valve mounted in between. There are four CF40 ports available on load lock cube; one for view window or gate flange, one for pressure gauge, one for turbo pump and one for burst disk. There is also a smaller sized transferring arm to transfer sample between load lock and growth chamber. The catch up head of transferring arm was designed by SPEC, it is incredibly precise and easy to use, and hold the sample plate very firmly.

4.3.2 System Assembly

The assembly of all components is a delicate job. Since all of the components had already been UHV cleaned, protection gloves must be ware at all time. The growth chamber was firstly mounted firmly next to the main chamber and connected through a gate valve before any components were connected to it. The assembly can be then further break down into four parts: sample stage, manipulator, load lock and evaporators.

Sample Stage

As described in the previous chapter, the sample stage has two insulated layers. The top layer holding the sample plate is also connected with high voltage and thermocouple wire. The high voltage cable we used is co-axial cable with Kapton coating. This layer of coating helps protecting the cable insulation and does not degas much in UHV environment. The thermocouple wire cable we used is a K-type wire, which is the most common case. This type of thermocouple has the sensing range of -180 to +1300 ˚C, the green cable is positive and white is negative. The ends of thermocouple wires were naked and tangled to a screw very close to the sample plate. This would greatly reduce the difference of measured temperature and actual value. In fact, spot wielding the thermocouple to the centre of sample plate would be the most optimized solution; however we did not have a spot wielder with that size.

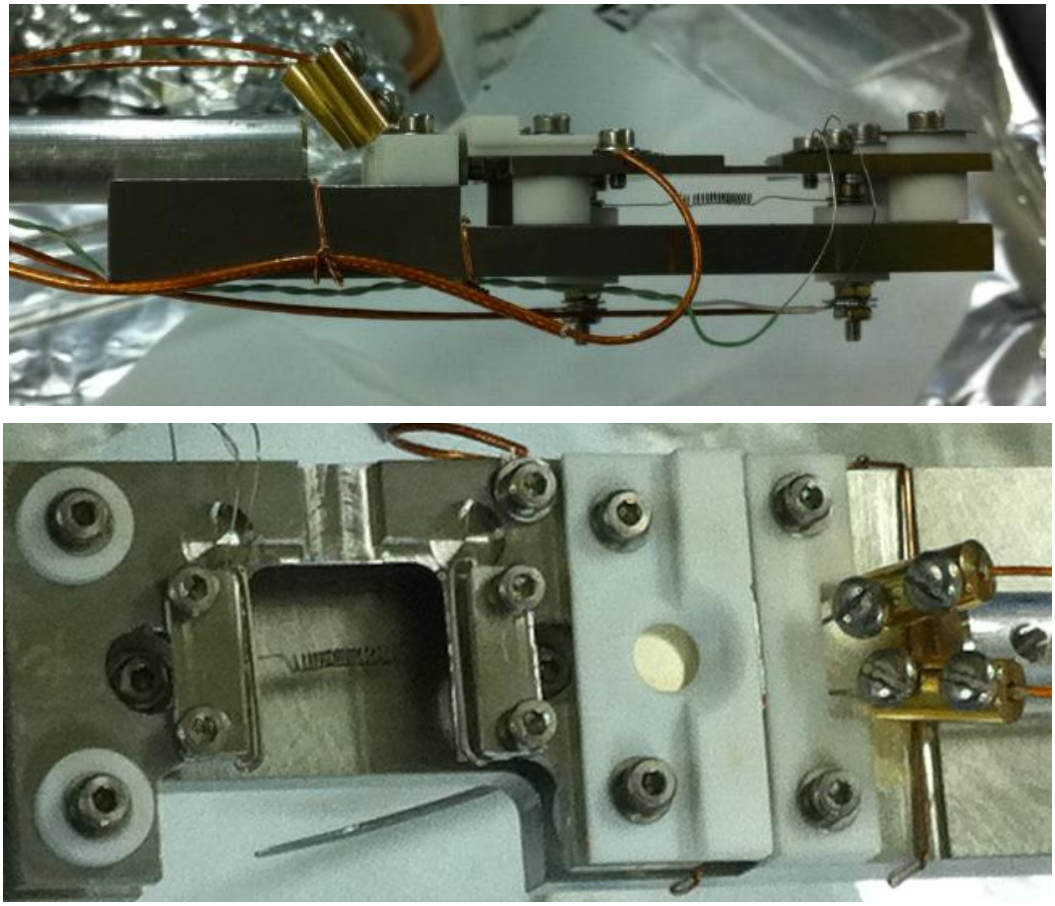

Figure 4.9. Sample Stage components.

The e-beam healing filament made of tungsten is positioned between the upper and lower layer of sample stage, and was slightly bended upwards for better efficiency. The stabilizing screws connected to it are isolated from the rest of sample stage with ceramic insulator, and has the current supply cable connected on the back. These cables are very similar to the high voltage cable, with Kapton coating but slightly thinner.

The quartz crystal microbalance sensor was positioned next to the sample plate, and was covered with a piece of ceramic. This ceramic is made to shadow the electrical connectors of the quartz sensor so that no material would be deposited on them and cause short circuitry. Through two copper connectors, the quartz sensor was connected wire Kapton wires to one of the flanges on the manipulator.

All components including screws, nuts, washers, ceramics were dipped in acetone and cleaned under ultrasonic bath for at least 10 minutes. And all cables were aligned to the manipulator arm and tightened with small copper wire rings to prevent them tangling each other. All connections were tested several times to ensure they are firm enough.

Manipulator

The manipulator has two mechanical movement stages combined. The lower stage with x, y and z direction of adjustments was made by UHV Design, and sits right on top of the chamber. The upper stage with 4 flange ports and rotary drive was mounted at the top of the system. Inside of it there are multiple electrical connections that must be taken extra care of. 3 out of 4 flange ports were used for all connections inside, one for high voltage on sample plate, one for thickness monitor, and one for both filament current supply and thermocouple.

Figure 4.10. Manipulator feedthrough flanges.

Load lock

Load lock, also call sample prep chamber, was mounted on one of the CF40 flange port on the top flange layer of the growth chamber. It is a small cubic shaped chamber with 6 standard flange ports on each side. These 6 flange ports are connected to transfer arm, pressure gauge, turbo pump, burst disk, window gate and the growth chamber valve. The suitable positions of each of these components were discussed many times to ensure easy and safe operation.

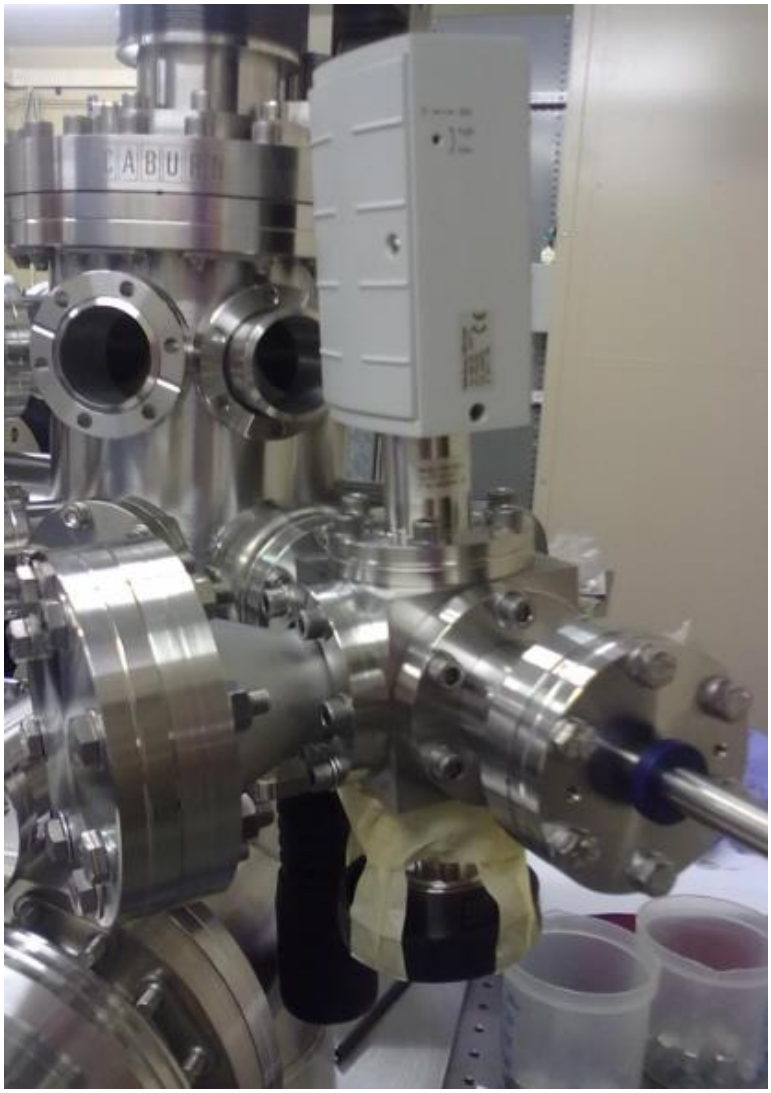

Figure 4.11. Load lock configuration.

Evaporators & Ion Sputtering Gun

There were totally two evaporators and one ion sputtering gun attached to the growth chamber. The evaporators have 99.99% of iron and 99.99% of chromium in each of them. They need separated current and high voltage supplies but share the same water cooling system and ground connection. The evaporators are the key components of the growth chamber. They produce high purity and uniform source material vapour and deposit it on the sample substrate. The water supply helps cooling the temperature of metal part close to the tungsten filament, and must be on at all time during deposition. The ion sputtering gun is used to generate a small beam of ion to remove invisible particles and contaminations on the substrate surface. And it has a gate valve implemented at the front end to prevent material vapour being deposited on ion gun.

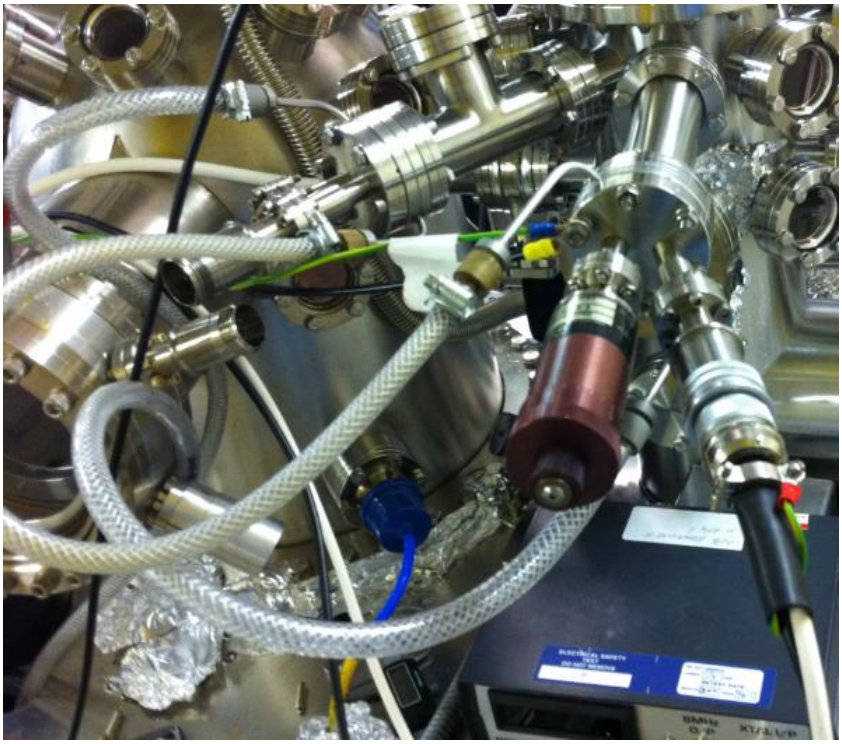

Figure 4.12. E-beam evaporators.

Figure 4.13. Ion sputtering gun.

The electrical supplies for both evaporators and e-beam heating sample stage were placed at a stable surface not far from the chamber. The current supplies have the maximum output of 6A and high voltage supplies have the maximum of 1250V and 5000V respectively.

Figure 4.14. Current and high voltage supplies.

4.4 Growth Rate Calibration

The amount of the material deposited on the substrate surface needs to be monitored for steady growth rate and thickness calculation. For Artemis beam time project, the growth rate is measured using a quartz crystal microbalance sensor.

Quartz crystal is a type of thin and fragile material that has the property of generating an electrical current with a fix oscillation frequency when electrically energized. When source material is being deposited on the sample, it is also applied to the sensor surface, increasing the total mass of the crystal and thus decreases the resonant frequency.

The quartz crystal we used has the natural vibration frequency of 6MHz, and the digital controller offers the precision of 0.01 Hz. This is extremely sensitive measurement device and must be maintained stable at all time. Since the signal generated from quartz crystal is tiny, the connection wires must be as short as possible and secured at fix position. The cables used inside of MBE chamber were bind along the manipulator arm, and the external BNC cables have the length of only 150mm.

Considering the growth rate of our e-beam evaporator was controlled by monitoring the emission current of source material, the total amount of material evaporated can be held at a very stable level and the flux rate is therefore uniform. This makes the thickness monitor calibration easier as the calculation can be expresses as the equation below.

$$Growth\ rate = \Delta thickness/time$$

$$Relation\ between\ QTM\ and\ thickness = \Delta actual\ thickness/\Delta frequency$$

Measurement of actually film thickness of calibration sample

A piece of silicon wafer was prepared as a thickness calibration sample using e-beam lithography technique. The surface of this sample was coated with a layer of PMMA that had been developed to form an array of square pits. These pits were made to create sharp edges so that when washed away, the remaining film edge would be equally sharp so the AFM would identify such depth profile more accurately. The sample was transferred in the MBE chamber for 25 minutes of Fe film growth at emission current of 15mA. After film growth, this layer of PMMA was easily washed away using acetone, leaving cubic shaped films on the surface. This sample was then examined under Atomic Force Microscopy, and the difference in height measured is the actual thickness of the film.

The AFM result in Figure 4.15 shows the thickness of Fe film was very close to 10nm. Therefore the growth rate of 15mA of emission current is

10nm/25min/0.14nm per ML = 2.8 ML/min

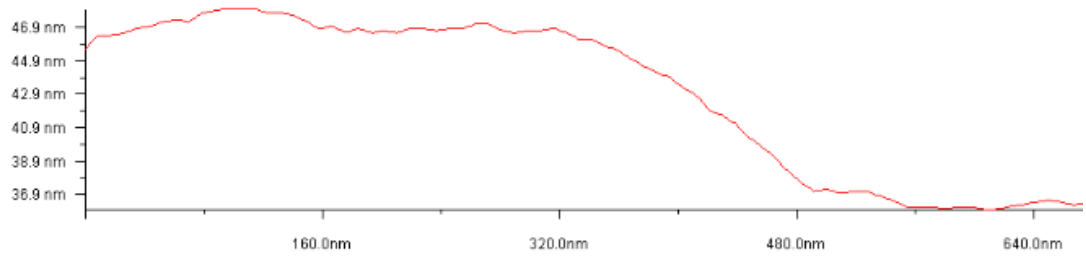

Figure 4.15. AFM step morphology.

4.5 Experimental Results

The experimental data presented in this section is divided into 3 catalogues. Starting with MOKE measurements. The hysteresis loops gave the first indication of the quality of the film. Though such information is not accurate, it would be sufficient enough to distinguish the most desired single crystalline iron sample. After deposition, all of the selected sample were then transferred to the analysis chamber. A series of TR-MOKE measurements were conducted when the zero delay between the pump and probe laser beams were identified. Ultrafast demagnetisation processes excited by the pump laser with increasing power were captured and put into comparison. Lastly, TR-photoemission was performed to further look into the mechanism during the demagnetisation process. The meaning of such results are discussed in the relevant section.

4.5.1 MOKE Hysteresis Loops Measurements

There were in total 6 pieces of samples made before any measurements were taken place. One of the main reasons of producing multiple samples was to explore the most desired recipe to produce single crystalline Fe films. All samples were removed from UHV environment and coated with 3nm of Gold in thermal evaporator to preserve the Fe film as much as we could. Longitudinal MOKE measurements were conducted through all samples along 4 different angles 45º apart. The best sample was selected and the recipe was used as standard for the rest of sample preparation. This sample has reasonable MOKE hysteresis loops (Figure 4.16). The film was expected to be 56 monolayers thick, or around 8 nm. The result shows that the film has an easy axis along 45º and a hard axis at 135º. The intermediate measurements were neither too easy nor too hard. This is a clear indication that the film exhibit uniaxial anisotropy.

The rest of samples have various qualities regarding to the hysteresis measurement and were not discussed here. The reason of non-consistent sample quality was because the growth was plagued by equipment failures – irreparable in the time available due to the nature of UHV systems. Firstly, the Ion gun sputter failed; meaning we could not completely clean the sample surface prior to growth. Secondly, the sample could not be placed close enough to the Auger electron spectrometer for detailed chemical analysis of the surface and finally, the thickness monitor also failed. Altogether, while we were able to grow the desired films – by applying our previous experience and growing calibration samples - the surface quality appears to have been undesirable. The above is the best sample we have successfully grown in the Artemis station, with its easy axis along [011] (corresponding angle: 90 degree) orientation and hard axis along [0-11] orientation (corresponding angle: 0 degree). The following time-resolved MOKE and photoemission results are taken from this sample.

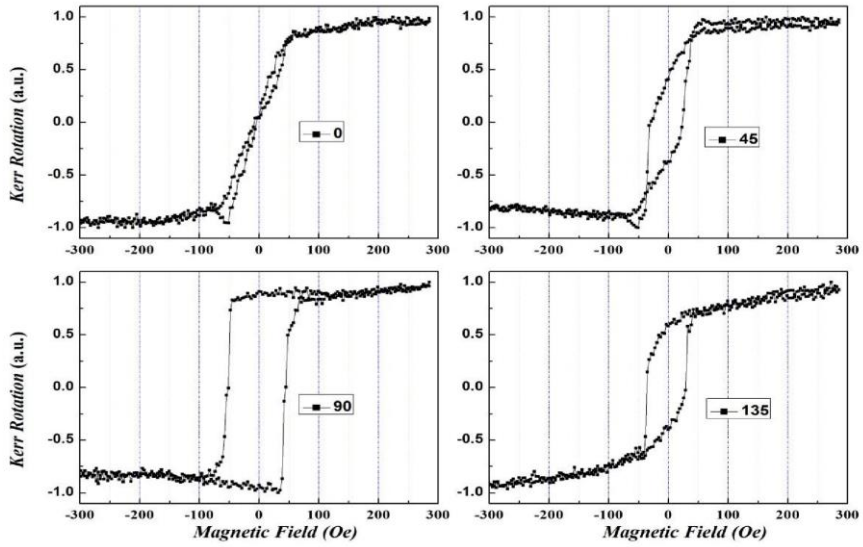

Figure 4.16. Hysteresis loops of thick Au (3nm)/Fe (56ML)/GaAs (100). The average emission current of 14.9 mA, growth pressure of 2.74x10^{-9} mbar, 20minute deposition.

4.5.2 Time-resolved MOKE measurements

The in-situ TR-MOKE portion of the experiment was successful. The zero time-delay between the XUV probe pulse and the 800nm pump pulse was precisely located by time-resolved MOKE using the zero-order light of XUV as the probe. Clear time-dependent MOKE and reflectivity signals were obtained at various laser influences for determining the relationship between the dynamic magnetic reversal and the electronic structure. The demagnetisation process is a response to the local temperature increment. Such increment would result the reflectivity of the sample to vary and being detected.

The time resolved reflectivity data taken under various pump excitation power is shown in Figure 4.17. The data indicates the electron temperature of the excited Fe films reaching its maximum at 300 fs after the 800 nm pump excitation regardless of different pump power, while the peak amplitude of the electron temperature increases with the pump power. It was expected that the electron temperature increasing linearly with the input power, and this linearity is shown the red curve of Figure 4.19, except the highest power point where we think the sample is burnt. After reaching the peak temperature, the electron system starts to cool down and transfer its energy in to the lattice till both electron and lattice temperature reaches an equilibrium in a couple of picoseconds. The time-resolved Kerr rotation data taken at the same time as the reflectivity data is shown in Figure 4.18. The magnetization of the Fe sample has undergone an ultrafast demagnetization after the pump excitation. The demagnetization reaches its maximum at around 300fs delay, which is 100fs lag behind the peak of the electron temperature. This is as expected because this demagnetization is heat-driven after the thermalizing of the electron system. The peak amplitude of the ultrafast demagnetization increases with the pump power, and its value is plotted as a function of the pump power in Figure

4.19. Higher pump powers burnt the sample surface resulting in much smaller signals. The time-resolved MOKE was not only used to locate the zero delay between the pump and probe pulses, but also provide enable us to choose the optimized pump power and delay time slots to maximise the TR- Photoemission signal.

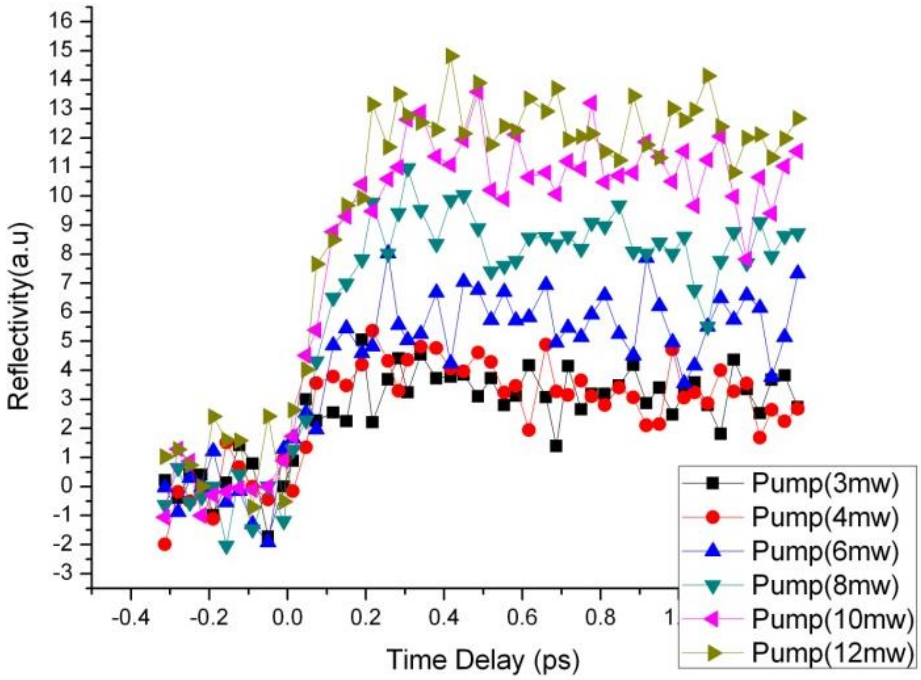

Fig 4.17. Reflectivity versus time delay between probe and pump for 56ML Fe/GaAs.

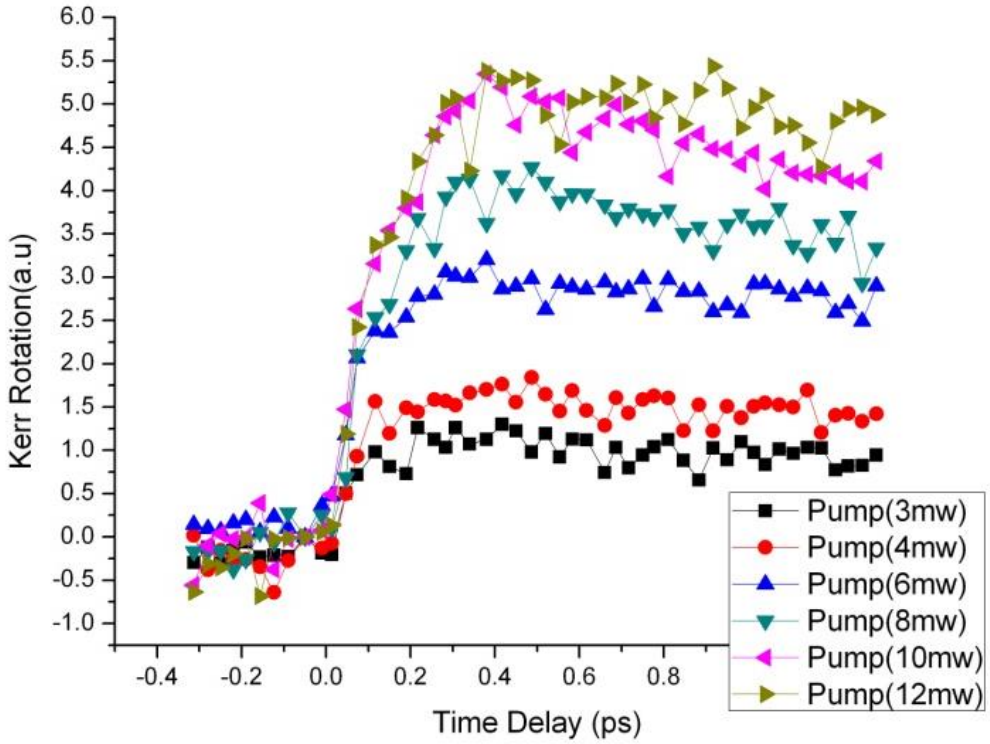

Fig. 4.18. Kerr Rotation against pump and probe time delay for 56ML Fe/GaAs.

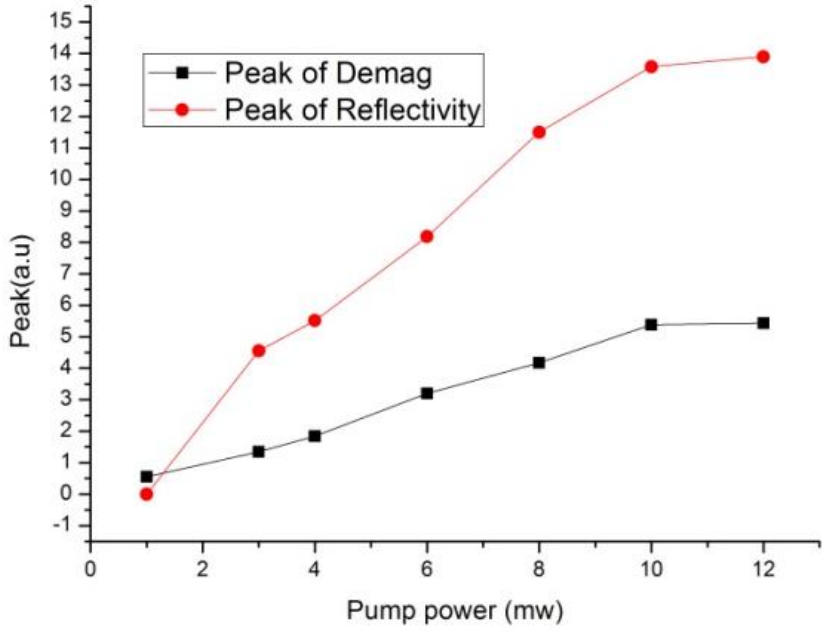

Fig 4.19. Peak demagnetisation and reflectivity signals versus pump power.

4.5.3 Photoemission Spectroscopy

Since both TR-MOKE and photoemission spectroscopy share the same probe path, when performing the photoemission spectroscopy, optical components that used before for doubling frequency, reducing intensity and blocking the original 800nm IR (BBO crystal, wheel attenuator, 400nm narrow-band filter and polarizer) needed to be taken out from the probe part, to let the 800nm laser pulse hit the gas jet for XUV generation. The XUV position is well defined by looking at the zero order light and it has been a successful technique in previous Artemis experimental runs.

The photoemission spectroscopy refers to the techniques based on the photoelectric effect that observed by Hertz (1887) and later explained by Einstein (1905). He defined that when light is incident on a sample, the surface electrons can absorb the photon energy and escape from the material. The kinetic energy hv- φ (where v is the photon frequency and φ is the material work function). Typically, the work function can be seen as the potential barrier at the material surface to prevent valence band electrons from escaping, which is usually 4-5eV.

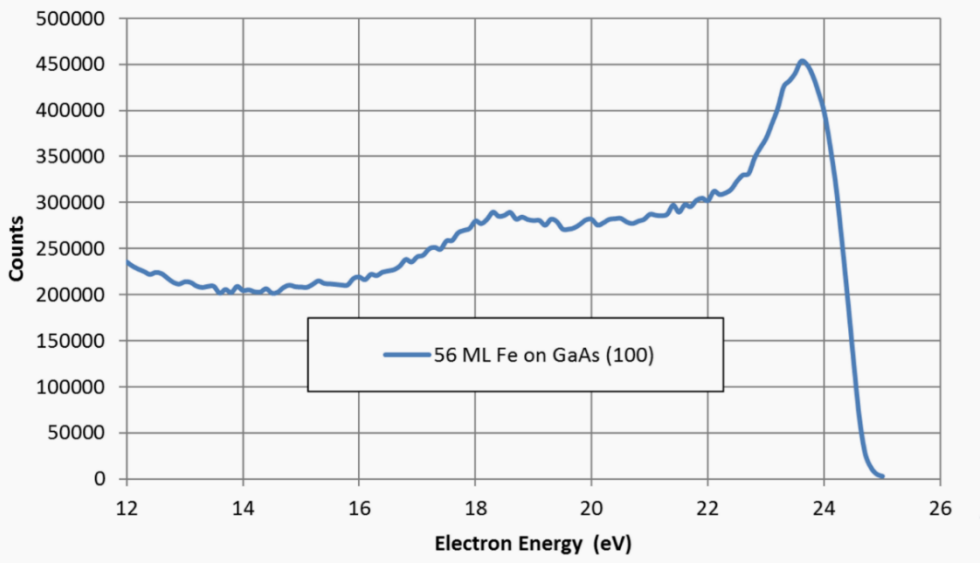

Figure 4.20. A raw photoemission spectrum obtained from 56ML Fe/GaAs.

Photoemission spectra taken from the previous sample (56ML Fe/GaAs) is shown in Fig 4.20. The right-most peak is the Fe 3d electron peak. Despite being sampled very soon after growth, oxidation is already starting to affect the spectra visible at 18.2 eV. Signal levels were reasonable but more attention needs to be focussed on minimising surface contamination in order to obtain low noise, reproducible data with fast scans. Time resolved photoemission has been performed. The spatial overlap of the pump and the probe beams was confirmed on the sample using a CCD camera to visualise the zero order light spot and the pump spot. The XUV position is well defined by looking at the zero order light and it has been a successful technique in previous Artemis experimental runs.

During initial testing, TR-MOKE was performed in situ by frequency doubling the zero order light. The time zero clearly visible in the TR-MOKE signal was then translated to the XUV system such that, by knowing the BBO and filter thicknesses, we predicted the photoemission time zero with good precision (+/- 0.1mm – equivalent to +/- 0.6 ps). Pump-probe photoemission was then recorded over the expected region around zero delay with a high temporal resolution (step sizes down to 30 fs). Examples of the photoemission spectra around the Fermi edge taken 11.25 ps before the pump excitation (-11.25ps), 0.05 ps after pump excitation (+0.05 ps), and 8.75 ps after pump excitation (+8.75 ps) are shown in Fig 4.21, together with a spectrum without pump beam present. The shift of the Fermi edge between the three spectra with pump present and the spectrum with XUV only indicate the space charge from the pump beam produce a 0.4 eV shift in the spectra. The red spectrum taken at 8.75 ps after pump excitation does show a decrease in the photoelectron count around 22 eV energy level. Considering the photon energy of the pump pulse is 1.5 eV, this decreasing at an energy level 1.5 eV

below the Fermi edge suggests the excitation of electrons due to absorption of the pump photons.

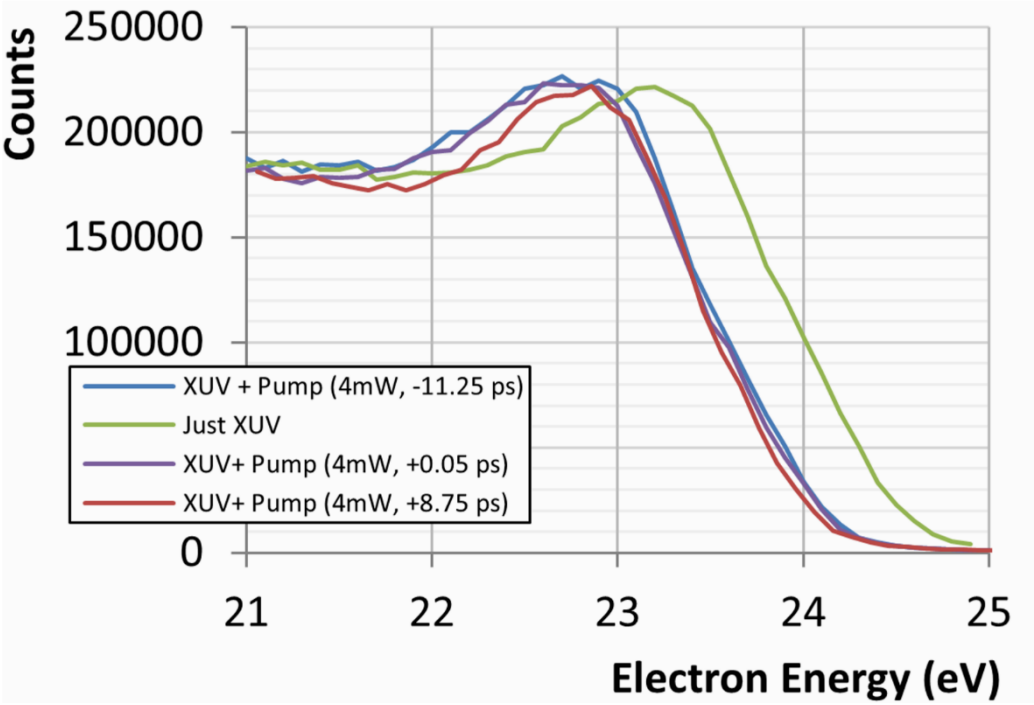

Figure 4.21. Four photoemission spectra of the 3d peak taken from a 56ML Fe sample. One spectrum was measured without the pump beam and the others with the pump at various delays. The variation visible in the pumped spectra is no larger than the time-domain noise - with an average standard deviation of ~6000 counts. N.B. At negative delays, the probe arrives on the sample before the pump. At t=0, the pump and probe arrive simultaneously and at positive delays the probe arrives after the pump.

In the spectra taken at other earlier time delay, there isn't such obvious decreasing in electron counts below Fermi edge. To trace up any trend in the time-resolved spectra data, an average value was taken over the region bounded in red as shown in Fig 4.22 for each spectrum recorded at each delay time. The counts integrated over the kinetic energies of 22.5 to 24 eV around the Fermi level indicate a variation of the energy density curve (EDC) at different time delay as shown in Fig 4.23. A decreasing just below and an increase just above the Fermi edge would be expected after time zero due to 1.5 eV pump photon excitation. In Fig 4.23, there is a trend of signal decreasing in the integrated count just below the Fermi edge, though the signal to noise ratio is not good enough to make a solid statement.

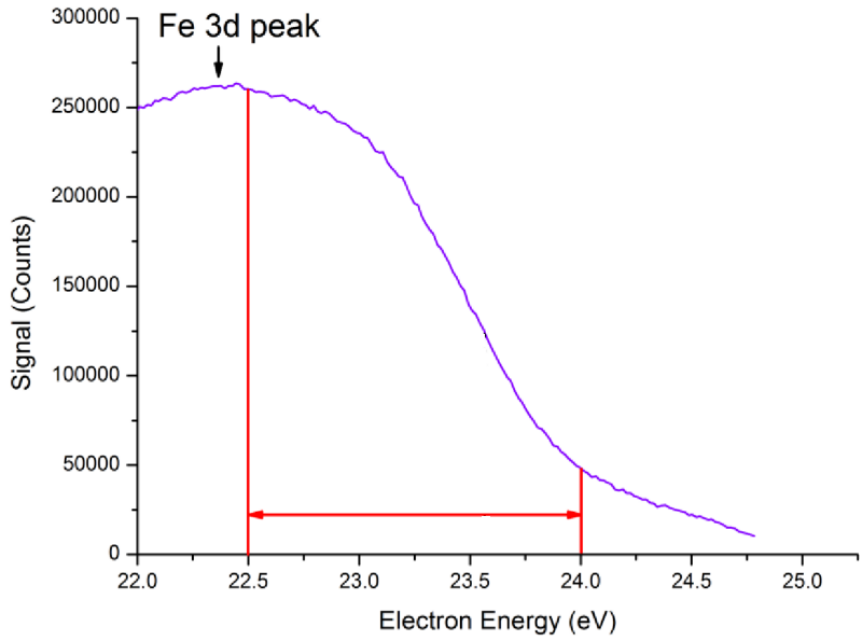

Figure 4.22. An example curve from the time-resolved photoemission work focusing on the 3d peak and Fermi edge on a 56 ML sample. An average value was taken over the region bounded in red for each spectrum recorded at each delay time.

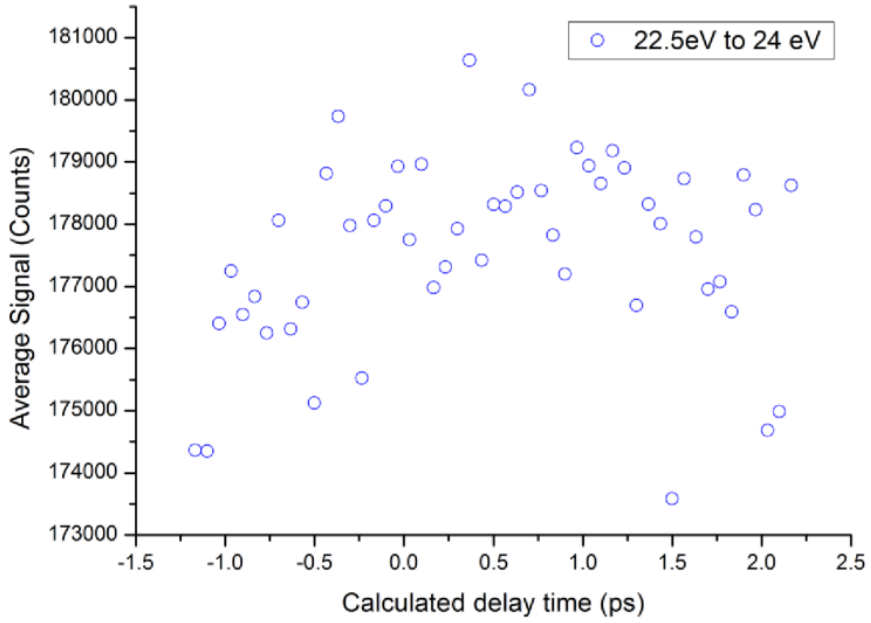

Figure 4.23. The average counts within the bounded region for each spectrum plotted against the predicted delay time at which it was measured. N.B. At negative delays, the probe arrives on the sample before the pump. At t=0, the pump and probe arrive simultaneously and at positive delays the probe arrives after the pump.

Space charge effects from both the XUV and the pump pulses were observed as is reported in Fig 4.24 and 4.25. Interestingly, as the pump intensity increased, a negative shift was observed but as the XUV probe intensity increased, a positive shift was observed. Of note is our observation that the effect of the pump did not degrade over the time between laser pulses – no matter what the delay between the pump and the probe was, the effect measured (by the probe) was the same. While this data is not primary to the experiment, the presence of the charging effects shows that we were able to achieve a good pump-probe overlap that was maintained throughout the complete time-domain sweep. As such, it is fair to conclude that the lack of time resolved data is once again a result of surface contamination while the time domain noise is a result of very slight movements of the pump on the non-uniformly contaminated surface.

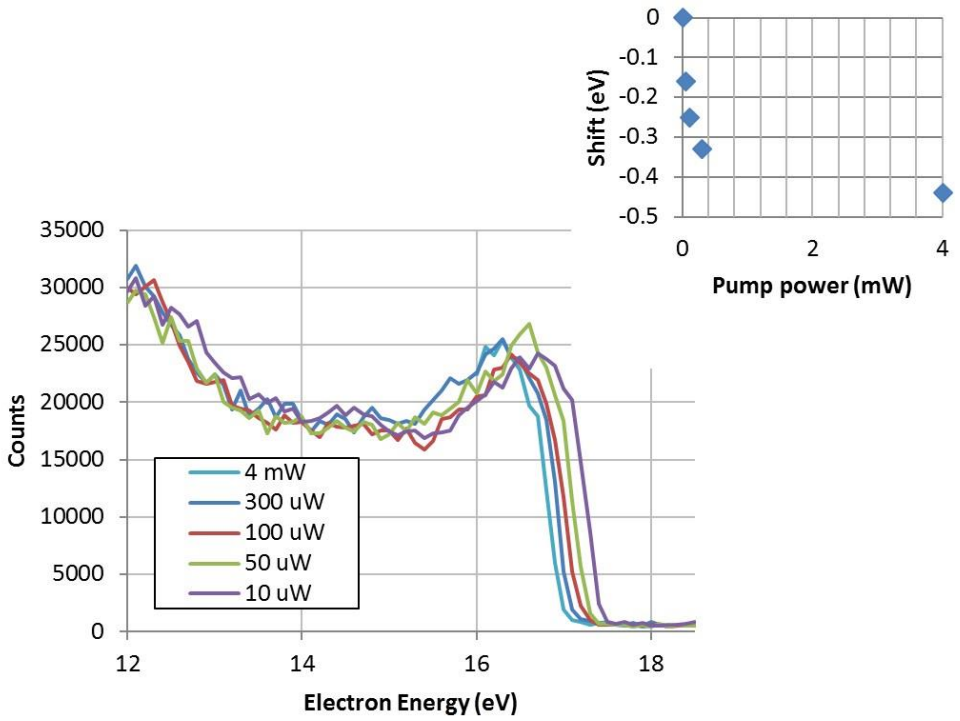

Figure 4.24. A series of spectra of the 3d peak taken with different pump powers illustrating the increased electron screening with increased pump power on a 56 ML sample. Inset; Shift at half peak height versus pump power, referenced to the 10uW pump power spectrum.

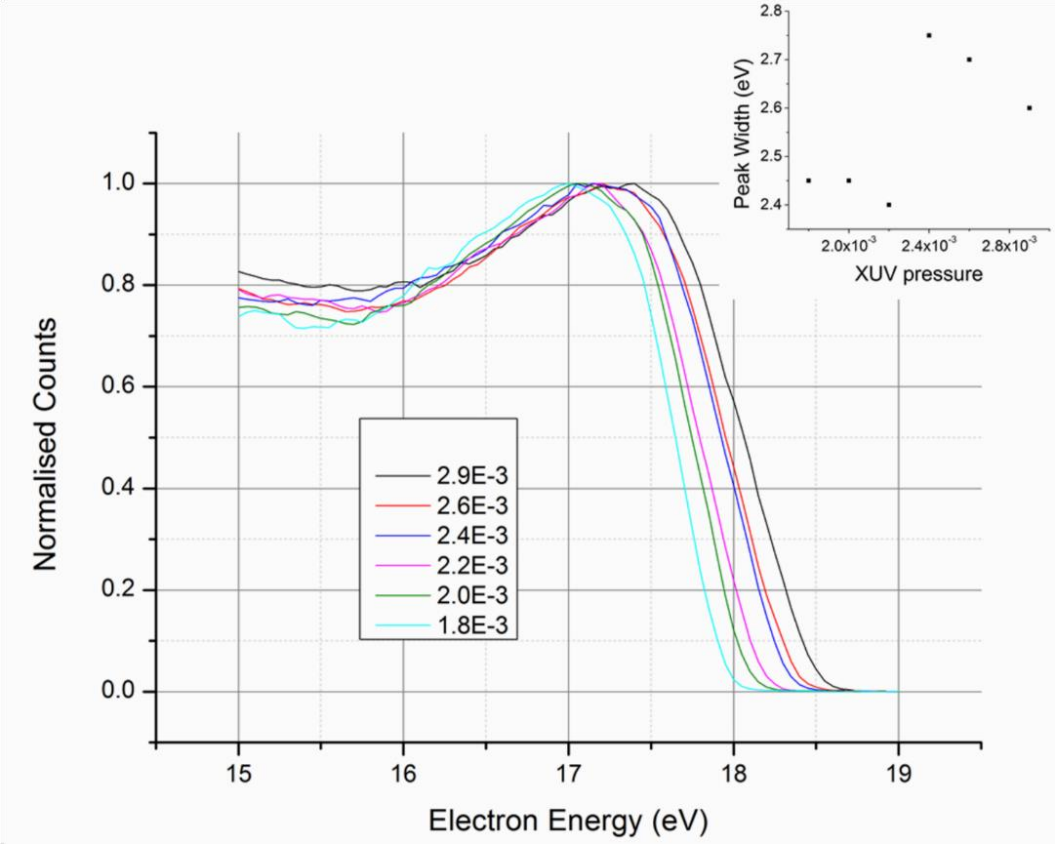

Figure 4.25. Normalized 3d peak photoemission curves demonstrating the energy shift at different XUV probe intensities. At 2.9E-3 mbar gas pressure, there are 2E6 photons per pulse incident on the sample. Inset: Peak width versus gas pressure.

4.6 Summary

For the Artemis project, firstly, we have made great achievement in instrumentation. We have successfully assembled a MBE growth system attaching to the main characterisation chamber. We have also set up a time-resolved in-situ MOKE apparatus to enable parallel measurements of time-resolved globe magnetisation dynamics together with time-resolved electron band spectroscopy by photoemission in XUV region. Good quality single-crystal Fe thin films have been grown for the in-situ measurements, which is essential for doing time-resolved measurements at sample magnetic remnant state. The zero delay between the XUV pulse and the pump laser pulse has been precisely located by performing time-resolved in-situ MOKE measurements. The TR-MOKE portion of the experiment was largely successful and an ultrafast demagnetisation of Fe films has been observed. The ultrafast demagnetisaton reached its maximum at 400 fs after the pump laser excitation, and the degree of the demagnetisation was found increased with the pump power. The time-resolved reflectivity data was also recorded which provided the temporal profile of the electron temperature of Fe films after the pump laser excitation. The peak temperature of the electron system was found at about 300 fs time delay. This suggests that laser-induced ultrafast demagnetisation is a heat-driven effect.

The parallel time-resolved photoemission spectroscopy measurements were performed with the aim to get insight of the microscopic mechanism underlining this ultrafast demagnetisation phenomenon. While good photoemission spectra were observed for each of the samples at different delay time between the XUV and the pump pulses, both the pump and the probe were found to induce an effect of electron screening, which

depends on the power of the beam. The spectra taken from a 56 ML Fe sample at various time delays were compared with each other.

A trend of decreasing of integrated electron counts from a region just below the Fermi edge was presented in the spectra taken after the zero time delay, which suggesting the depopulation of electron density due to the pump excitation. This project provided a valuable tool to explore the origin of ultrafast demagnetization in Fe thin films by combining both macroscopic and spectroscopic measurements performed in the femtosecond time domain. The ultrafast temporal evolution of the correlation between the global magnetization loss and the band structure could potentially give us an insight into the mechanisms of the laser induced ultrafast demagnetization.

We have successfully demonstrated the feasibility to probe the time dependence of the density of states. The results gathered for this project, however, have also proved that the photoemission measurements under this resolution could not give indication of significant change of DOS of electrons within the demagnetisation process. If there really is a change, it would be every small (< 200meV) and would not be detected under current experiment condition.

Chapter 5

Magnetic Properties Development of Fe and Ni on GaAs(100)

5.1 Introduction

The ferromagnetic metal/semiconductor hybrid structures have been one of the most extensively studied hybrid spintronic materials and the research activities in these area still continues due to the good electrical/thermal conductivities and high Curie temperature of those materials. There are mainly three types of magnetic materials to construct the hybrid magnetic/semiconductor spintronics structures; and these three types of magnetic materials include:

i) Ferromagnetic metals and alloys, such as Fe, Co, FeNi etc,

ii) Heusler alloys such as NiMnSb and CoMnGa, and

iii) Half-metallic magnetic oxides including Fe_3O_4 [41-47].

The spin-injection from ferromagnetic materials/electrodes is critical process for realising future spintronics devices, like spin-transistor, and the spin injection process and magnetic properties of ferromagnetic electrodes are closely linked with interface condition [48,49,50]. However, the effect of the substrate surface preparation to the

magnetic properties of the films is still not clear at all. In this chapter, different methods of surface treatment were implemented aiming to modify the properties of subsequently deposited ferromagnetic metals, particularly the MBE growth of Fe on GaAs. One focus was the growth of epitaxial ferromagnetic metal/semiconductor hybrid structures (Fe/GaAs). This is due to the fact that the lattice constant of bcc Fe (a_o=2.866Å) is almost exactly half that of GaAs (a_o=5.654Å). The purpose is to explore the impact from the semiconductor surface prepared using different procedures to the magnetic properties of the Fe films, and in particular to get insight in the origin of the novel uniaxial magnetic anisotropy if Fe/GaAs(100), which is still an open issue.

As for Ni growth on GaAs (100), research over the years has reported various results regarding to the epitaxial deposition. A. Lahav has reported the interfacial reactions between Ni and GaAs, proven that it can be epitaxially grown on (001) and (111) GaAs substrates [51]. W.X. Tang later reported that the epitaxial growth of Ni on (001) GaAs has the limit of up to 2.5nm [52]. C.S. Tian successfully performed angle-resolved photoemission measurement of bcc phase of Ni film on GaAs (001), and calculated its ferromagnetic anisotropy [53]. S.A. Haque though did not produce single crystal Ni film on GaAs (001), his group discovered an anomalous temperature dependent magnetization [54] and an enhancement of the coercivity at 60nm of thickness [55]. However, all the above measurements were performed without mention of anti-oxidation coating of the film, so that the oxidation depth of the film were unknown.

This chapter has a section covering the observation of Ni film magnetic behaviours throughout growth process, including MOKE and RHEED measurement. The purpose is to explore the thickness dependency of Ni film on GaAs(100), and this is also the first study of the magnetic properties of the Ni/GaAs system using the in-situ technique.

5.2 In-situ MOKE Measurements for Fe/GaAs

5.2.1 Substrate Preparation for Fe/GaAs(100)

For this experiment there were two GaAs substrates prepared with an identical recipe except one were treated with ion-milling. The process was carefully conducted to ensure no other factor could differ the quality of these samples. Both samples were sliced from the same commercial wafer and cleaned in ultrasonic bath using RBS, acetone and isopropanol for 5 minutes respectively; followed by acid etching in H_2SO_4:H_2O_2:H_2O (4:1:1) solution for exactly 45 seconds. The residual solutions were rinsed off by DI water and substrates were blown dry using Nitrogen. All these were performed in a level 100 clean room to prevent any dust particles contamination. The etched substrates were immediately transferred to an MBE chamber with base pressure of $2x10^{-9}$ mbar, and heated to 200°C for 12 hours to completely remove any water molecules and gas attached onto the surface. In addition, both of the substrates were required to be annealed at 480°C for 45 minutes to further remove natural oxides and create unified surface reconstruction. But one of the samples was treated with ion-milling before annealing. Low energy Argon ion beams were sputtered onto the substrate surface for 10 minutes and gently removes a thin layer of surface material, exposing the virgin layer of the substrate.

Cleaning Process	Duration
RBS, Acetone, Isopropanol ultrasonic bath	5 minutes respectively
Acid etching H_2SO_4:H_2O_2:H_2O = 4:1:1	45 seconds sharp
DI water rinse and Nitrogen Blow	Thoroughly and blown dry
Outgassing at 200°C	12 hours
Ion-milling at $5x10^{-6}$mbar	Non/10 minutes
Annealing at 480°C	45 minutes

Table 5.1 Comparison of preparation process of two different substrate.

5.2.2 RHEED Patterns

Since the substrates stays in a UHV environment, there only way to examine the surface quality is to observe the RHEED (Reflection High Energy Electron Diffraction) patterns. The advantages of RHEED are mainly because it's in-situ, fast, and surface sensitive. Multiple RHEED patterns were recorded throughout film deposition for monitoring purposes.

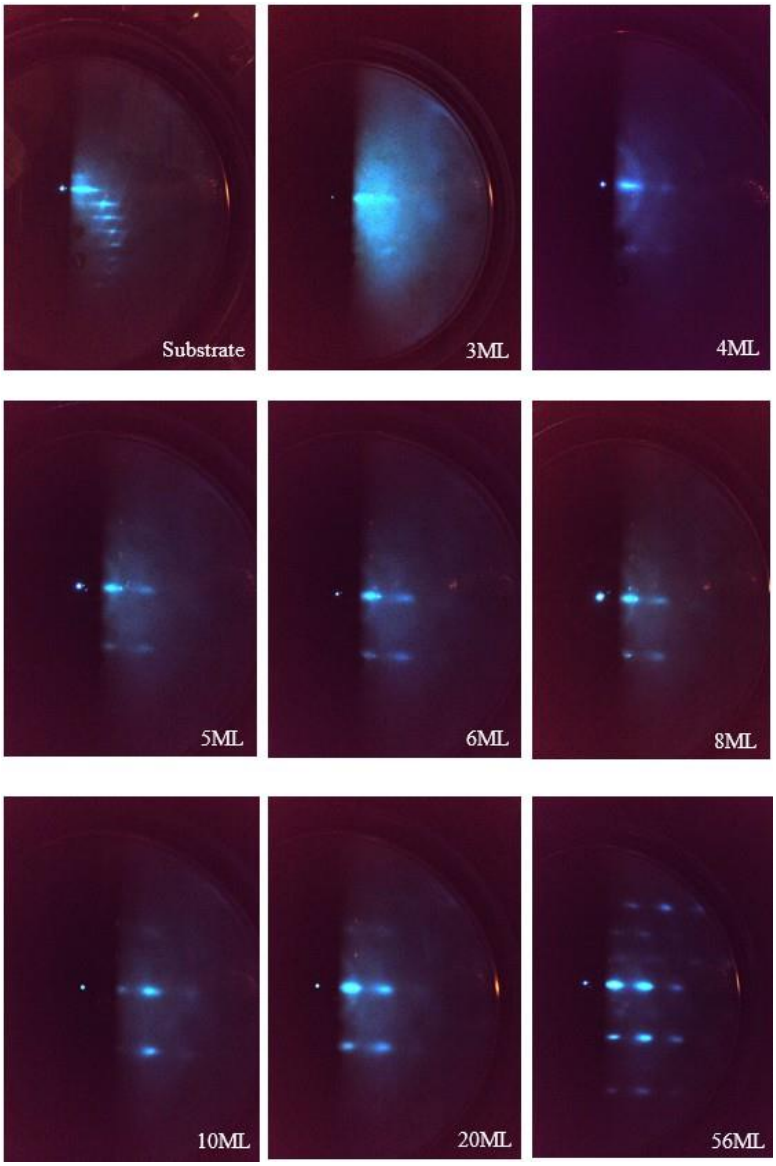

Figure.5.1 RHEED patterns taken from Fe films grown on substrates with wet chemical etching only.

Fig.5.1 shows the first series of RHEED patterns of various atomic layers of Fe grown on chemical-etching-only substrates. One can see that a clear RHEED pattern was observed for the GaAs. After the deposition of 4ML RHEED pattern from Fe film appeared and the clearness is drastically increased with the increasing of the thickness of Fe. These RHEED patterns show that Fe grows epitaxially on GaAs (100) at room temperature with an epitaxial relationship of Fe (001) <100>||GaAs (001) <100>.

Fig.5.2 is the second series of RHEED patterns from the sample that has been ion milled before annealing. Due to the fact that the ion milling process not only helps removing natural oxidation layer but at the same time causes certain roughness to the surface, the RHEED pattern was dimmed by such roughness. This is presumably the reason that though the photos below still indicate the single crystalline of the substrate, the illumination is much weaker even under higher beam energy. The sharpness of the pattern is also blurring in this case.

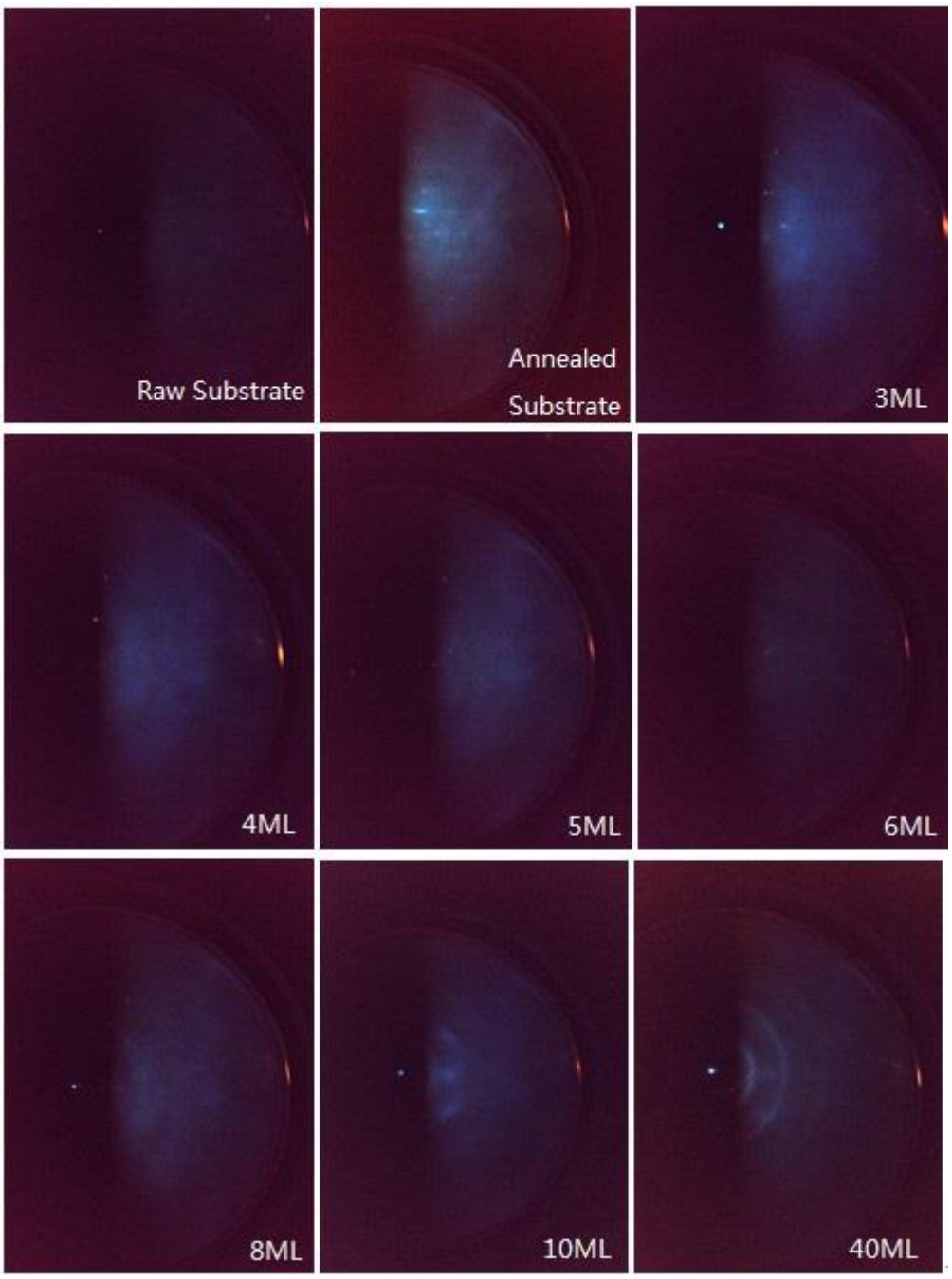

Figure.5.2 RHEED patterns taken from Fe films grown on ion milled substrate. Diffraction patterns appeared later than that of the un-milled sample, and a combination of single and poly crystalline pattern was observed.

Comparing with the previous sample RHEED patterns which occurring at 4 ML of thickness, the single crystalline diffraction of the ion-milled sample started to appear much later at 10ML of thickness. The film did not continue epitaxial growth and turned to poly crystalline at higher atomic layers. It is also worth noticing that, though poly crystalline diffraction started to appear and became dominant, the single crystalline diffraction was always observable at this thickness. During experiments, it was also found that single crystalline diffraction was only observable when the incident angle of RHEED beam was large. Glancing incident beam angle does not reveal such pattern. Consider that the penetration depth of RHEED beam is usually between 100-1000Å dependent on the angle of incidence, the different pattern at different angles of incidence reveals the thickness dependence of the crystalline structure of the film. It is believed that the Fe film deposited on this substrate was of a hybrid Crystallinity, which display a net result as poly crystalline but consists with large well-ordered grains.

5.2.3 In-situ MOKE Hysteresis Loops

Same as recording RHEED diffraction pattern images, in-situ Magneto-Optical Kerr Effect (MOKE) measurements were conducted for each stage of thickness during film deposition. The change of evolving of magnetic properties of both samples were closely monitored and the results are plotted in comparison with each other. The analysis of in-situ MOKE measurements were divided into two with different purposes. For the early stage of film deposition, it is more focused on identifying the appearance of ferromagnetic properties; and for the later stage of film deposition, anisotropy became an interesting issue to look into.

When the Fe material being deposited onto the substrate surface, it took a certain amount of time to form a complete layer of film that covers the whole surface. This is because that the MBE system offers UHV environment, allowing film deposition rate to be maintained at low level. The material vapour would condense on the substrate first and start self-alignment according to the surface reconstruction. Local grains were then formed before connecting into a continuous film. In this case, the Fe film deposition was performed at the rate of 1ML/min. Figure 5.3 shows the plot of the early stage hysteresis loops of two samples. At the first few monolayers, there was no clear ferromagnetic switch observed. This can be explained by island-growth-induced nano-sized magnetic particles and the formation of such super paramagnetic un-continuous clusters. The Fe film deposited on the un-milled substrate started to show ferromagnetic properties at the thickness of 8ML, and at 10ML, the MOKE signal enhanced even more, with sharper magnetisation switch near the origin. However, for the ion-milled sample, there was no clear ferromagnetism signal even at the thickness of 10ML, but at

20ML, a sharp ferromagnetic switch has been observed. The author believes that the delay of ferromagnetism of the films is due to the delay of film formation of a complete Fe film, and the possible factor that prevents the super paramagnetic clusters from magnetic coupling with the neighbouring clusters may related to the surface roughness cause by ion-milling process.

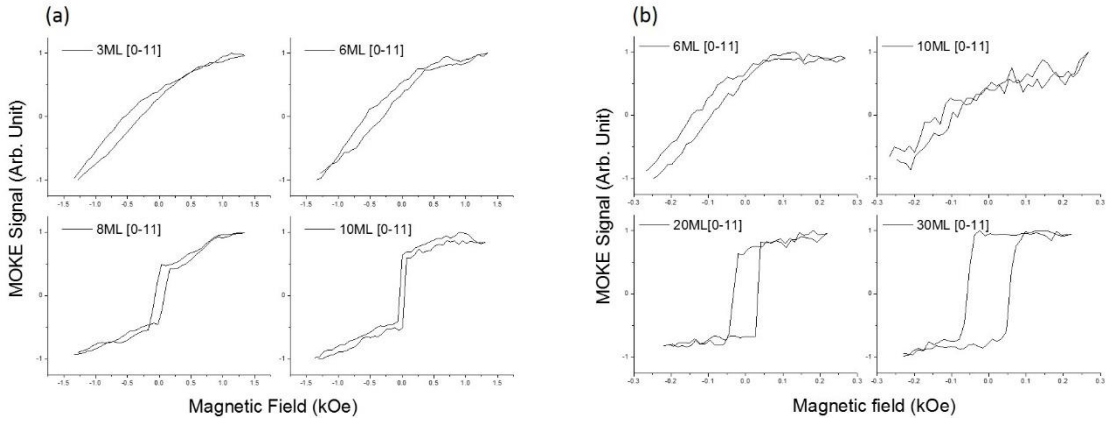

Fig. 5.3. Hysteresis loops of un-milled (a) and ion-milled (b) sample with various thickness. All of the loops are measured along the [0-11] orientation in the plane. (a) shows the ferromagnetic property became measureable at the thickness of 8ML. (b) illustrates the delayed appearance of ferromagnetic property at the thickness of 20ML.

With more Fe being deposited, in-situ MOKE measurements were performed at each thickness node and along both [011] and [0-11] directions in order to reveal the anisotropy properties of both samples (Figure 5.4). It was discovered that for Fe film deposited on the un-milled substrate, nearly identical hysteresis loops are found for both [011] (easy axis) and [0-11] (hard axis) for the film with thickness reaching 20ML. This indicates that the interface-induced effect in the film is relaxed already at this growth stage and bulk cubic anisotropy starts to be defined in the film plane. In contrary, the Fe films on substrates with ion-milling treatment show a strong uniaxial anisotropy when the film thickness is below 30ML, indicating that a strong chemical bounding is an important factor for developing this interface-induced effect. `This interface-induced uniaxial anisotropy decreases when the film thickness is further increased. This result suggests that the interface roughness due to ion milling has delayed the development of ferromagnetism in Fe film, and prevented the film remain a single crystal structure at atomic layers above 10 ML. However, again due to the ion-milling cleaning process, the better chemical bounding between the substrate and the first few Fe atomic layers enhanced the interface-induce uniaxial anisotropy. Such assumption is explained and supported by the Atomic Force Microscopy (AFM) images in the next section.

Figure.5.4. Hysteresis Loops of thicker Fe deposited on both un-milled (a) and ion-milled (b) samples. (a) shows nearly identical loops along [0-11] and [011] orientation with atomic layers at 10 and 56 ML.

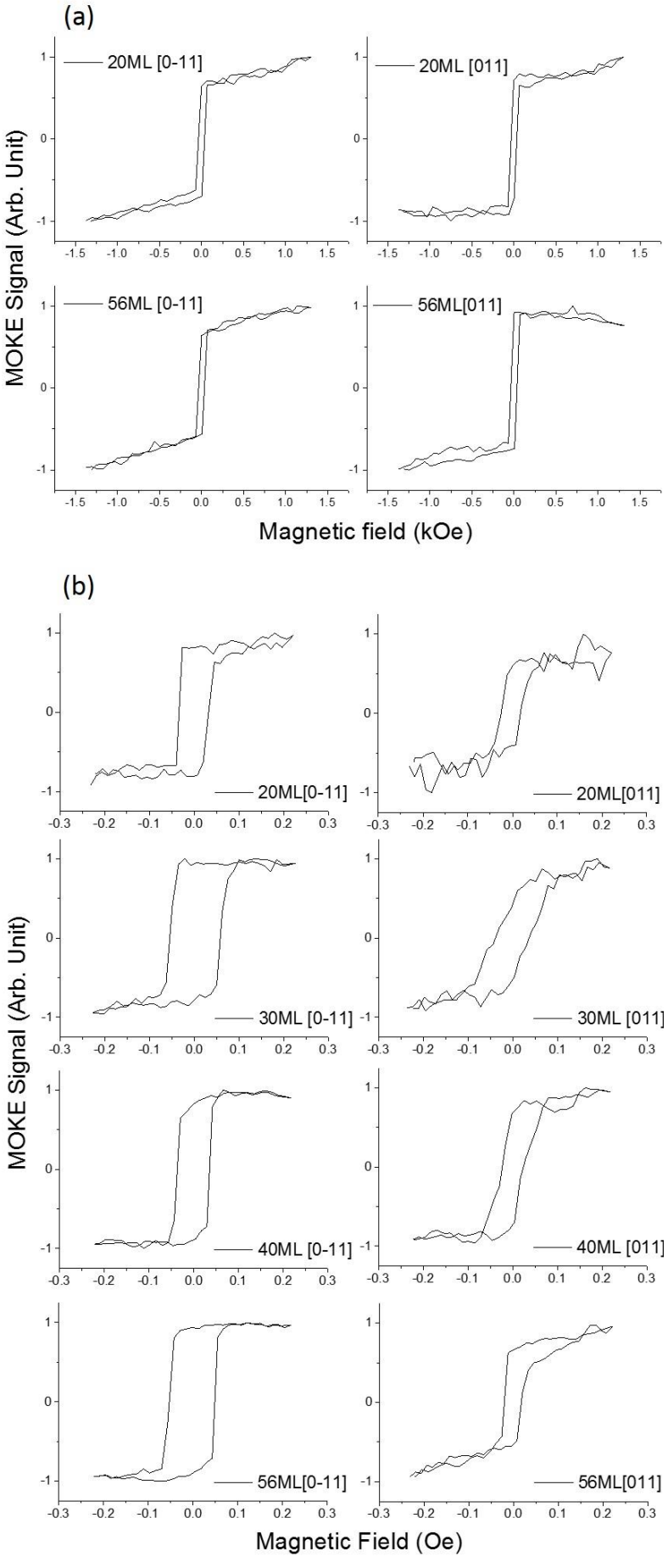
(a)
20ML [0-11]
20ML [011]
56ML [0-11]
56ML[011]
MOKE Signal (Arb. Unit)
Magnetic field (kOe)
(b)
20ML[0-11]
20ML[011]
30ML [0-11]
30ML [011]
40ML [0-11]
40ML [011]
56ML[0-11]
56ML[011]
MOKE Signal (Arb. Unit)
Magnetic Field (Oe)

5.2.4 Morphology by AFM

Based on the assumptions from previous sections, the delayed expression of ferromagnetic properties and strong uniaxial anisotropy displayed by a polycrystalline film were both related to the ion-milling treatment. Judging by the fact that ion-milling does not induce any other contamination to the substrate but only roughness by removing a thin layer of surface material, AFM surface morphology scanning were performed to look for possible evidences (Fig 5.5). Both images were taken after film deposition.

The AFM scanning area was selected as a 500x500 nm section near the central area of the samples, and the scanning rate was limited at 1Hz. Linear profile was analyzed in such area. Figure 5.5(a) shows the result for sample made with un-milled substrate. The contrast ratio of the surface area is unified, showing there is little surface roughness. The linear profile backs up this statement, indicating that the maximum roughness for this sample is $\pm$0.59nm. On the other hand, results shown in Fig 5.5(b) is the profile for sample made of ion-milled substrate. The contrast ratio is rather larger in this case, and the section roughness is much greater, with the maximum roughness of $\pm$1.26nm. There may have been nano clusters with diameter of around 50nm and the thickness of 1-2nm formed on this sample surface. It might help to explain the reason that the ferromagnetism of film on ion-milled substrate was developed at a later stage.

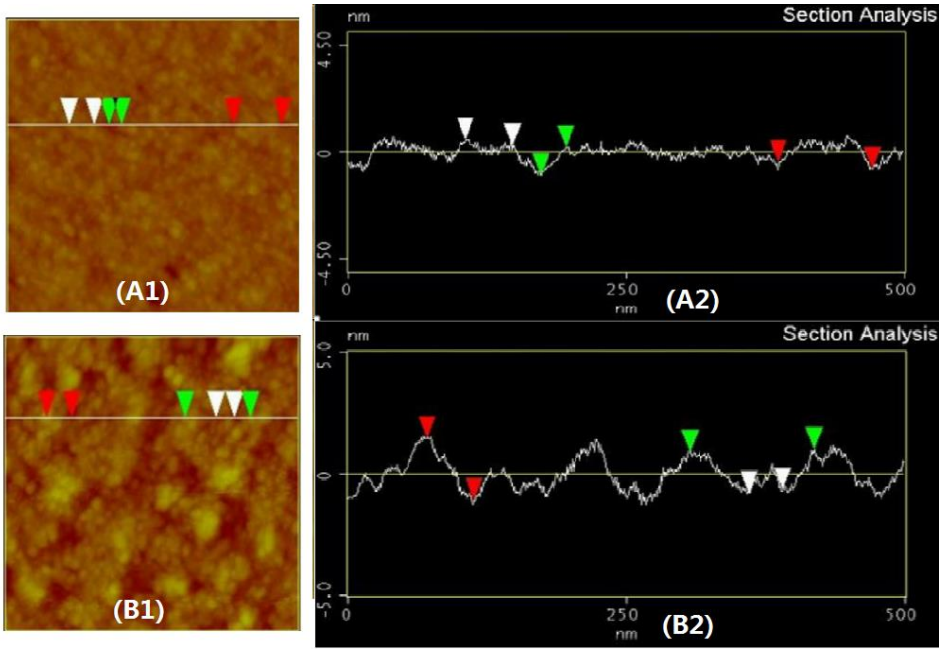

Figure. 5.5. AFM surface morphology of sample with un-milled substrate (A1) and ion-milled substrate (B1); and the respected linear cross-section profiles (A2) and (B2).

5.3 Thickness Dependency Measurement of Ni/GaAs(100)

5.3.1 Substrate Preparation and RHEED

As the substrate used for Ni deposition is the same as that for Fe, the substrate cleaning and preparation processes were exactly the same. Two pieces of GaAs substrates were prepared but annealed at 380º and 480º respectively. The deposition rate for Ni was also adjusted to 1ML/min, and the growth was conducted at room temperature. The rate was pre-calibrated by TEM.

5.3.2 Structural Properties

Since the lattice mismatch between Ni and GaAs is over 14%, epitaxial growth was not expected in this case. However, a series of RHEED diffraction patterns were still recorded along [0-11] and [011] direction only for the purpose of confirmation.

The following Figure 5.6 shows the process of RHEED diffraction development at the early stage of film deposition. The substrate showed well-ordered and sharp diffractions along both [0-11] and [011] direction. After 1.3nm of film deposition, the substrate diffractions became blurry and almost. At this stage of deposition, the Ni film has not fully cover the surface of the substrate yet, it is divided into local clusters of various dimensions and spread across the surface. With additional Ni atoms arriving to the substrate, the size and thickness of those clusters keep expanding and a complete film is formed. The RHEED pattern was then reappeared on the screen and the ring shape pattern indicating that the film did not form an epitaxy along either [0-11] or [011] direction, and a polycrystalline film was produced.

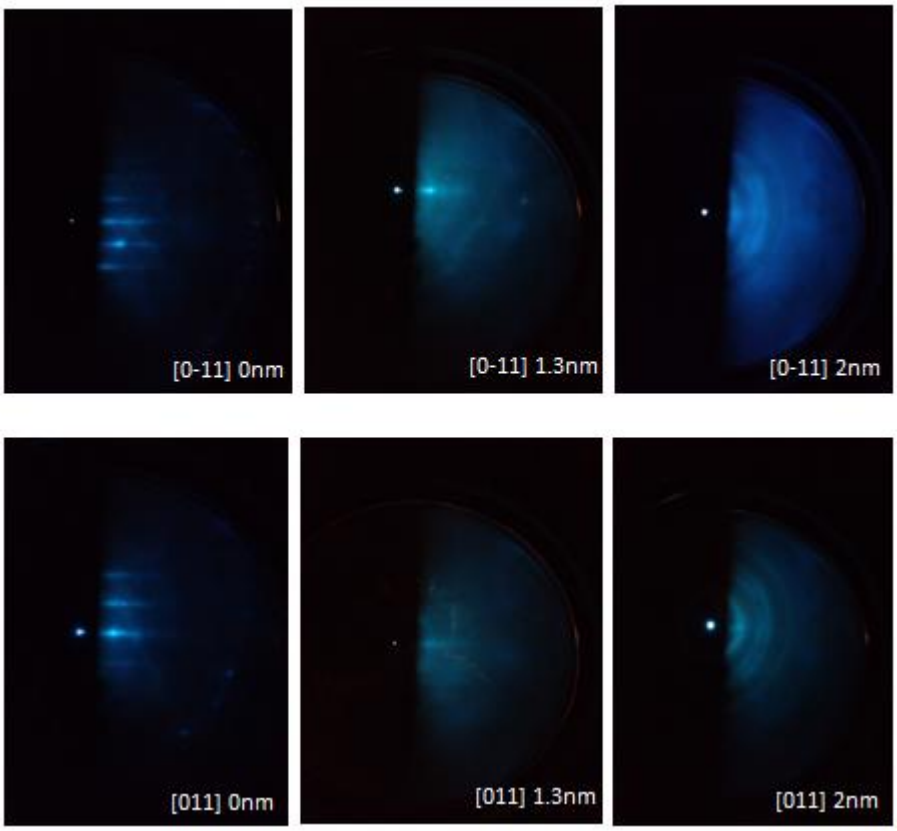

Figure 5.6. RHEED patterns along [0-11] and [011] direction at three different thicknesses.

5.3.3 In-situ MOKE Hysteresis Loops

In order to explore the influence of arsenic rich surface to the magnetic film, in-situ longitudinal hysteresis loops were measured in the process. All the measurements were taken place for certain stages of thickness throughout the deposition at room temperature.

The first interest would be the development of ferromagnetism of the film. Similar as other magnetic film deposition, it took a certain amount of time for Ni to film to fully cover the surface of substrate. For this project, the Ni film took extensively long time to develop ferromagnetic properties. On the substrate that has been annealed at 480°C, paramagnetic hysteresis loop started to develop at the thickness of 1.76nm, but until the thickness reached to 10.56nm, there has been no evidence of ferromagnetic signal detected. Though as the thickness keep accumulating, the signal to noise ratio was improved greatly, indicating that the magnetic properties are enhancing along with the increment of thickness.

For the substrate that has only been annealed at 380°C, the magnetic properties were developed differently. At 1.76nm of thickness, though the film started to show paramagnetic properties as the other sample did, the signal to noise ratio was much lower; and at the thickness of 10.56nm, there was found no clear evidence of ferromagnetic properties appearing from the MOKE measurement. At a later stage of film deposition, a hysteresis loop different from typical ferromagnetic was detected at the thickness of 15.84nm and 17.6nm respectively. The mentioned hysteresis loops are plotted in the next page in Figure 5.7.

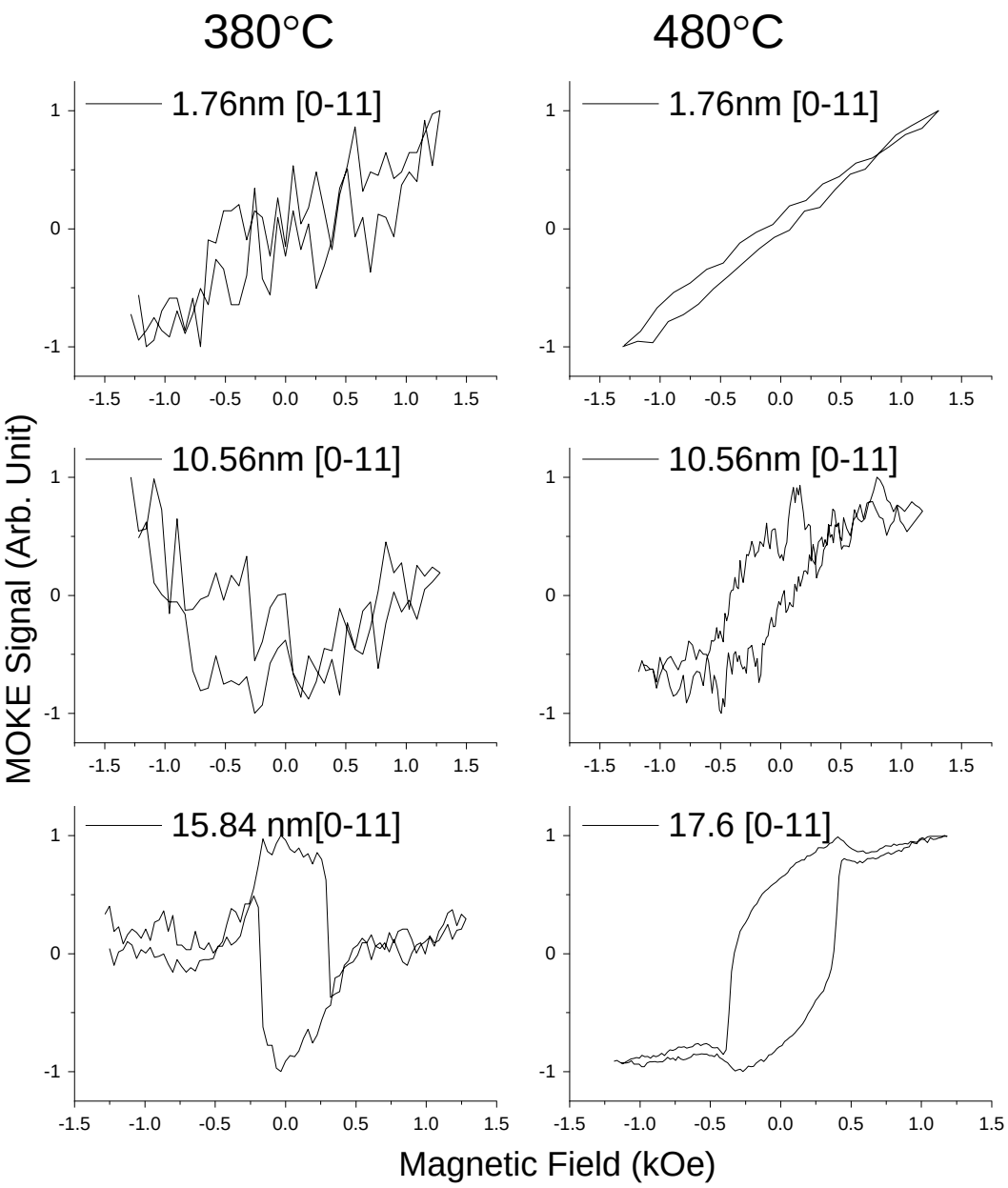

Figure 5.7. MOKE hysteresis loops along [0-11] axis development of Ni films deposited on GaAs (100) substrates with different annealing temperature.

Additional Ni material had been deposited on the substrate that was annealed at 480°C to explore further development of hysteresis. There are 4 individual loops shown below in Fig 5.8, though there is no obvious difference with the saturation field, the coercivity did drop greatly. These 4 hysteresis loops are also combined together for better illustration of the differences in Fig 5.9. And the trend of the coercivity change are plotted in Fig 5.10, with comparison to result published by S.A Haque et al [55], who observed little coercivity for the same thickness range of polycrystalline Ni/GaAs(001) at 100°C, but an enhancement at the higher thickness.

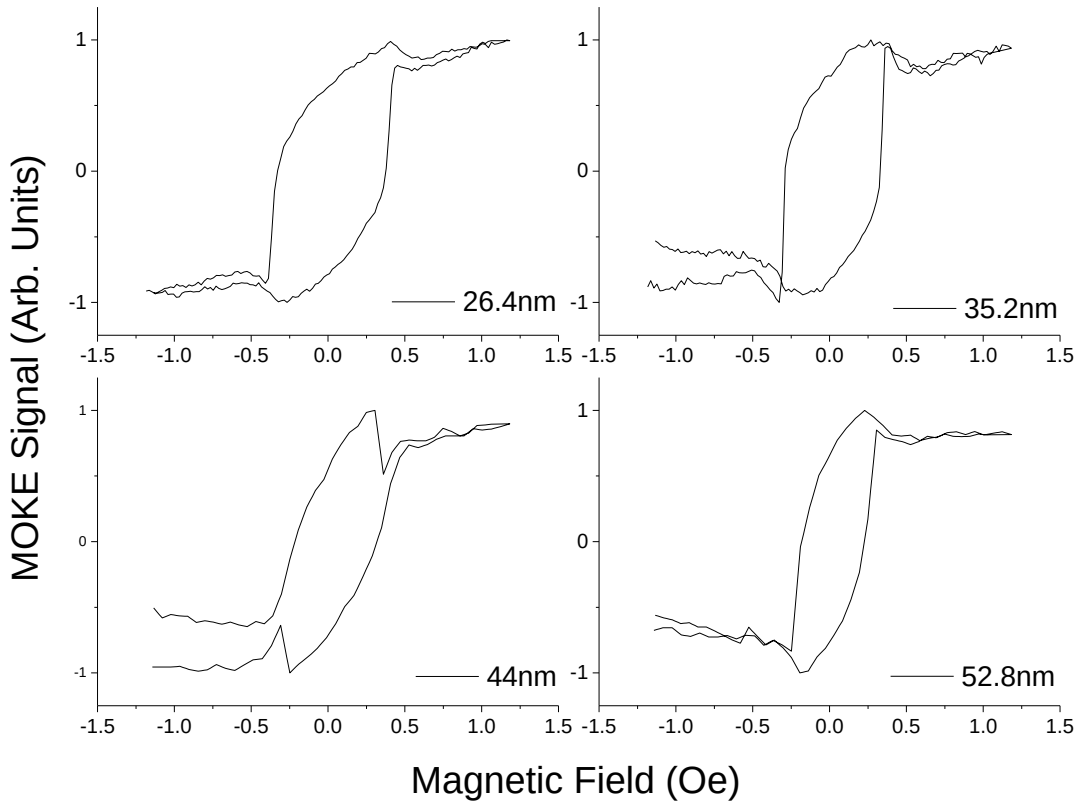

Figure 5.8. MOKE hysteresis loops at various thickness of Ni film on GaAs substrate annealed at 480°C along [0-11] direction, showing the thickness profile of ferromagnetic magnetic properties.

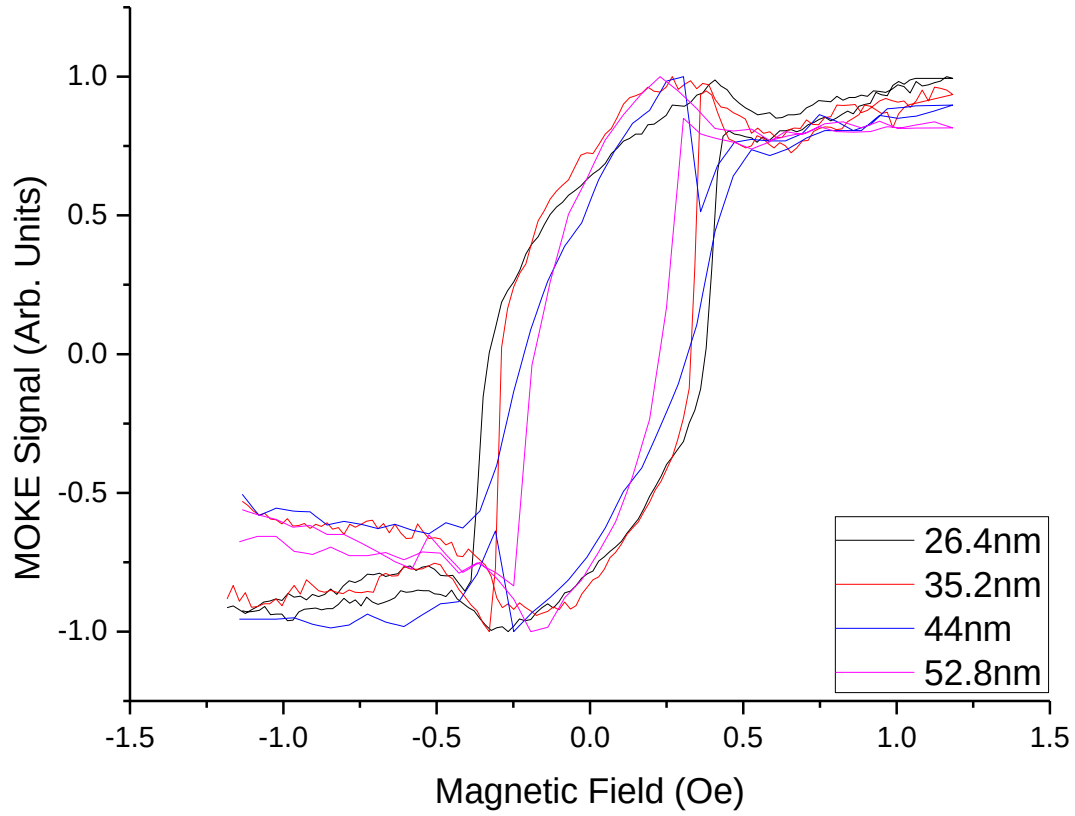

Figure 5.9. A comparison plot of the magnetic hysteresis loops of 4 different thickness of Ni film along [0-11] axes. Indicating a reducing trend of coercivity with increasing thickness.

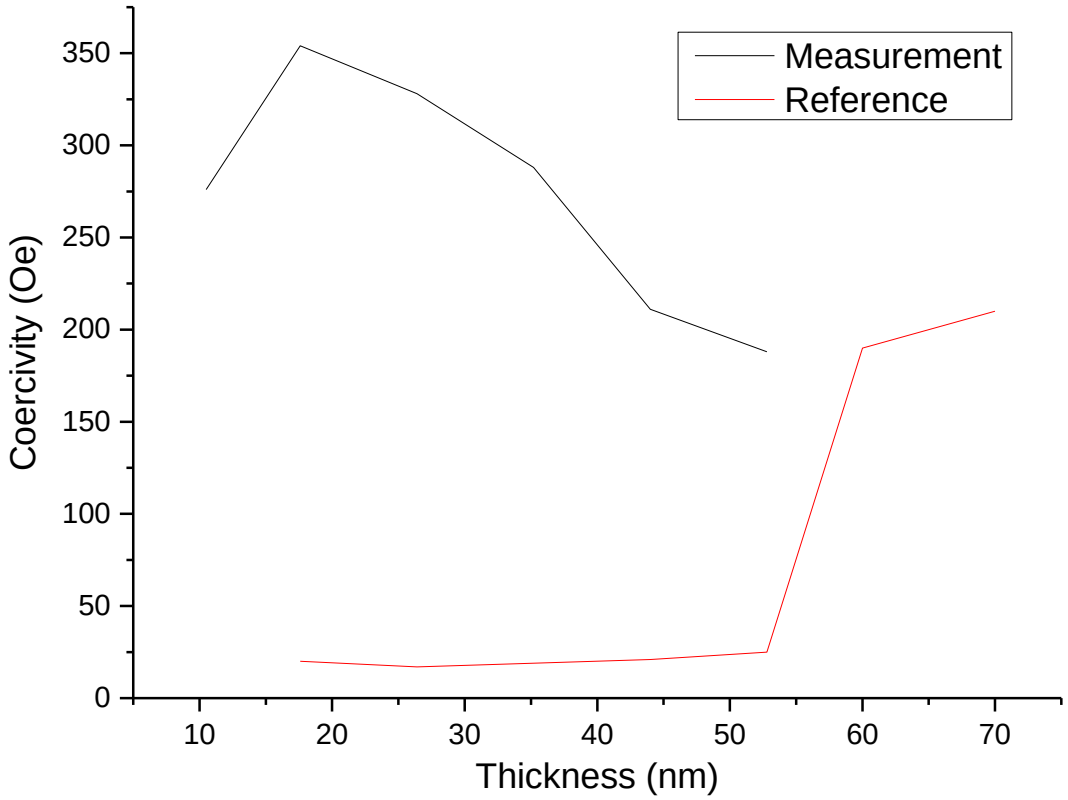

Figure 5.10. Saturation Field and Coercivity thickness dependency. Reference plot is for comparison purposes, and the result is reported by S. A. Haque et al.

For the other sample which has an Arsenide- rich surface, the situation was quite different. From the point the un-typical loop was obtained, the sample was rotated by 45° and 90° , and the magnetic properties along two other crystalline directions were measured. 3-axes hysteresis loops measurements were performed for each 1.76nm of film deposited until the thickness reached 24.64nm. The interesting result is anisotropy was discovered along each axis. The results are shown as the following.

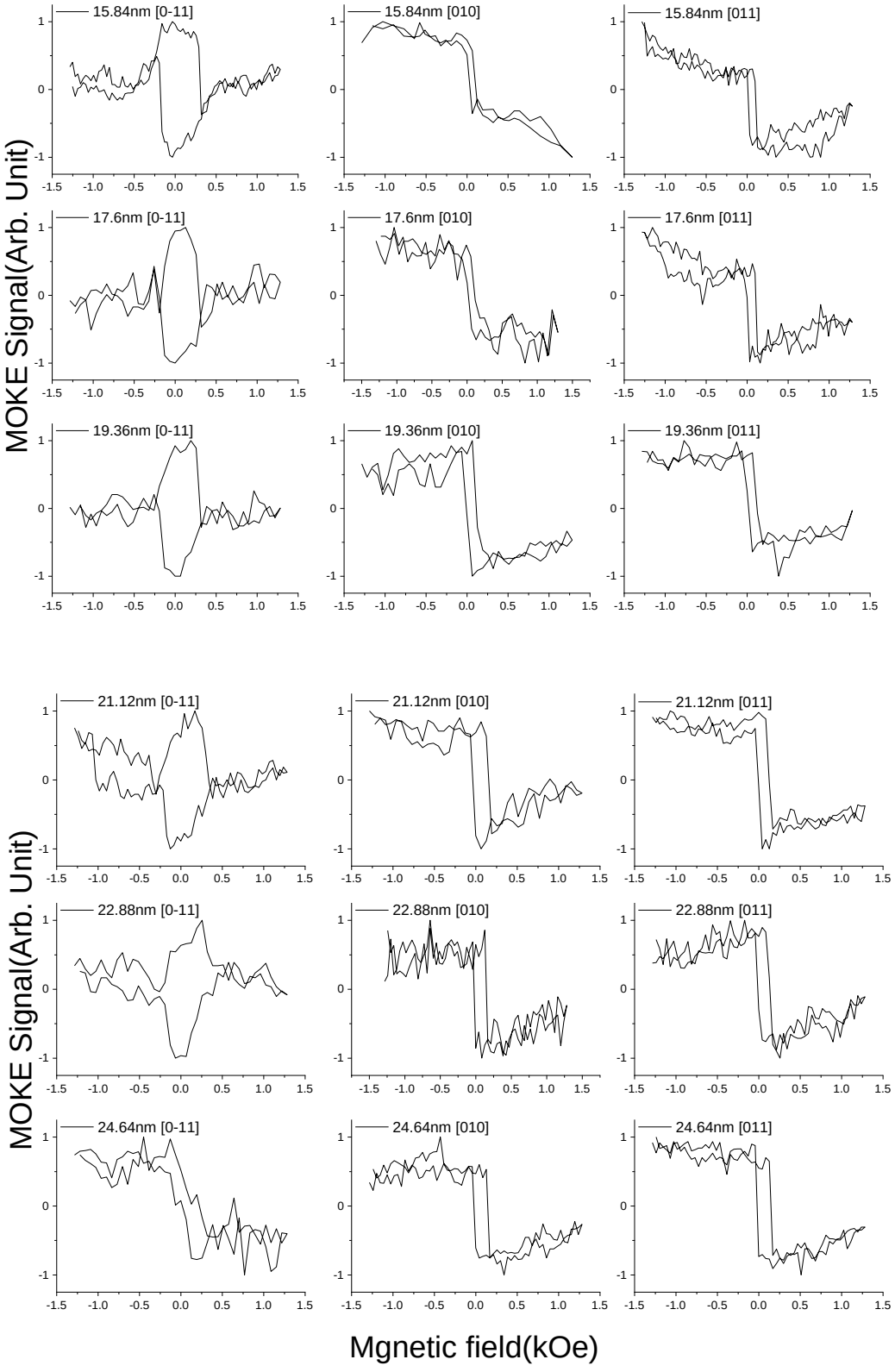

Figure 5.11. MOKE hysteresis loops of Ni film grown on arsenic rich GaAs substrate at various thickness along 3 different directions

5.4 Discussion and Conclusion

In the Fe film section, we discussed a topic that is rarely reported, the UMA relation to the surface treatment. We applied two different methods to treat semiconductor surface and found that their magnetic properties can be very different. Such difference were then found to be corrected with their structure and morphology. For the sample with un-milled GaAs, the RHEED patterns were much clearer and the film is flat as from the AFM measurement. The ferromagnetism thus also developed earlier at the thickness of 6-8ML. For the sample with ion-milled GaAs, there are clearly nano clusters formed and the RHEED patterns indicated that the film is a mix of single- and poly-crystalline phase.

	Un-milled Substrate	**Ion-milled Substrate**
Crystallinity	Single Crystalline	Hybrid
Ferromagnetism Development	Early (6-8 ML)	Late (10-20 ML)
Magnetic Anisotropy	Biaxial Anisotropy	Uniaxial Anisotropy
Surface Roughness	±0.59nm	±1.26nm

Table 5.2 Summarized comparison of samples made from different substrate.

Our results here are important to address the origin of the UMA, unexpected from the crystal symmetry of the bcc Fe, observed in Fe/GaAs (100) [49, 50]. There are three possible mechanisms responsible for the UMA observed in Fe/GaAs: 1) Shape anisotropy as the films show 3D island growth, 2) Intrinsic anisotropy due to the unidirectional nature of Fe-As and Fe-Ga bonds and 3) Magneto-elastic interactions due to strain in the ultrathin epitaxial films caused by lattice mismatch. These three mechanisms are still considered as the origin of the UMA in Fe/GaAs.

Our AFM images show no evidences of shape anisotropy due to the 3D island growth. Thus we can exclude the shape anisotropy as the origin of the UMA. While the sample with the un-milled substrate has better epitaxial growth, its UMA is much weaker. The sample with the ion-milling etched GaAs, however, shows clearly UMA, even though the film might be polycrystalline dominant. The ion-milling process not only removes surface oxidation and contaminations, but expose the raw layer of GaAs for film deposition, and thus enhances the chemical bonding between Fe-As and Fe-Ga. Our results have thus demonstrated for the first time that the surface contamination plays a more important role than the surface roughness in terms of the UMA in Fe/GaAs(100). In General, the results support the mechanism of "the unidirectional nature of Fe-As and Fe-Ga bonds", which means the atomic scale structure related to the semiconductor surface is responsible for the novel uniaxial magnetic anisotropy of the Fe/GaAs (100) system. From the application point of view, in order to control the magnetic switching of Fe films as the spin injection pads, the UMA is better to achieve a single switching of the Fe pads for the Fe/GaAs based spin-FET. Our work here suggests that the interface must be clean while the roughness is not that critical in this regard.

In the Ni film section, two GaAs (100) substrate were annealed at different temperature to create an As-rich surface and a clean one. Such surface difference were found to be important for the development of magnetic properties of Ni film. The crystalline structure of Ni/GaAs using our deposition recipe was confirmed. For the sample grown on the substrate that has higher annealing temperature, the ferromagnetic properties was developed at close to 16nm of thickness, and the coercivity kept dropping with more material being deposited on. This suggested that the film was more relaxed at higher thickness.

For the sample grown on Arsenide rich surface, there are two discoveries. One being the delay of ferromagnetism approximately 5nm later than the one grown on a cleaner surface; and anisotropy was observed even when the film is confirmed to be polycrystalline. The anisotropy along [011], [010] and [0-11] axes found at such thickness can possibly be uniaxial anisotropy, and is believed to be originated from the surface since the pinning effect between the boundaries of grains within the film is weak.

The mechanism behind the magnetic behaviour of polycrystalline Ni on GaAs is still a mystery since there are different results being published without confirmed theories. The author is also limited by the lack of any simulation and modelling work to further analysis the result and look for an explanation when compared with existing results. This could be a breakthrough of this research area and is hopefully be completed in the future.

Chapter 6

CoFeB Films on GaAs

6.1 Introduction

Ferromagnetic films on semiconductors exhibit an interface-induced UMA as discussed in above chapter[69]. However, due to the magnetocrystalline anisotropy and long range structural order of FM film in Fe/GaAs or Fe/InAs systems, the interface induced UMA is partially obscured[70]. To exclude the contribution from magnetocrystalline anisotropy of a body-centred cubic (bcc) FM film and focus on the origin of this UMA in FM/SC, the crystallinity of the film is required to be eliminated while the ferromagnetism remains undisturbed. An effective method would be alloying metalloid material into the ferromagnetic compound to form amorphous phase. Approximately 20% of Boron alloyed with CoFe compound has been proven desirable. The additional Boron only slightly reduces the Curie temperature and saturation field while completely destroy its crystallinity, making the alloy amorphous[71]. Over the years, research

attentions have been favouring to CoFeB due to the presence of UMA as an amorphous material.

Also, its high tunneling magnetoresistance (TMR)[4] and low-current induced magnetization switch[73] have been routinely studied and proven to be suitable for Magnetic tunnel junctions (MTJs)[74] with ferromagnetic electrodes possessing a perpendicular magnetic easy axis. The feasibility of CoFeB/MgO-based 40-nm-scale MTJs with sufficient thermal stability in high performance has been demonstrated[75].

Therefore, to impel the development of next-generation high-density non-volatile memory and logic chip based on CoFeB, it is urgent to investigate the fundamental magnetic properties of this novel material which is deposited on semiconductor. In this chapter, three CoFeB samples prepared on different orientations of GaAs substrates had been studied extensively using VSM, XMCD and TEM to investigate the possible origin of the UMA behaviour. The XMCD is capable of probing the orbital moments, which is correlated with the magnetic anisotropy. At the same time, TEM will provide the detailed about the interface, which is very often responsible for the magnetic anisotropy in the thin films.

6.2 Experimental

6.2.1 Synchrotron

A synchrotron is a type of large scale circular particle acceleration device. It was developed at GE research lab in 1947. The performance along with the scale has been evolving since. To this day, there are over 70 working synchrotrons all over the world for wide range of research.

The very fundamental mechanism of synchrotron is that it accelerate charged particles through a sequence of magnets that form into a ring until their speed reach almost to the speed of light. During the process, the movement of particles generates an X-ray dominant beam of light that is powerful enough to allow scientist to study the properties of particles. The synchrotron radiation is produced when the particles pass through a series of bending magnets and insertion devices that they are centripetally accelerated towards the centre of the tunnel by the Lorentz force.

A typical third generation synchrotron consists of a linear accelerator, a storage ring and a station ring. The linear accelerator is a short and straight tunnel for electrons to be generated and accelerated initially. The prepared electrons are injected into a small storage ring that has linear and curved sections. The linear sections are the insertion devices, which is a periodic array of magnets with alternating polarity of transversal or helical structure. The curved sections are bending magnets that tune the projectile angle of electrons to the desired direction. The energy loss during the change of direction will be replenished by a radio-frequency accelerator cavity in the insertion devices. The outer station ring contains multiple research stations that use a certain energy and phase regime of XUV and X-ray for various research purposes.

6.2.2 XMCD techniques

The magnetism research related to transition metal thin films are commonly determined by the sample structures and the presence of their interfaces. The crystal structures deviated from the interface would have different orientations and thus change the magnetic properties. Such changes are commonly determined by exploit magneto-optical Kerr effect (MOKE). The basic principle is based on defining the linear polarized light as a combination of two circular polarisation light. The magnetisation of the sample would have different absorptions between the two, causing the total ellipticity of linear polarised light to change after reflection[76].

X-ray magnetic circular dichroism (XMCD) is also a magneto-optical effect. In the regime of X-ray, the optical transitions are influenced by both initial and final state densities at the solid surface. Synchrotron radiation sources provides X-ray beams with tuneable energy and polarisation, allowing the magneto-optical effect being extended to X-ray regime [77]. Moreover, XMCD provide shell-selective information because the energy of the core levels is characteristic for each element. It is therefore a powerful tool to determine each constituent individually in complex magnetic compounds or multi-layer structures.

Typically, XMCD is defined as the difference in the absorption coefficients for right and left circularly polarised X-rays[78].

To put in an equation, it would be

$$\Delta\mu(E) = \mu^{+}(E) - \mu^{-}(E) \qquad (6.1)$$

The work of this chapter focuses upon the L_3 and L_2 edges of 3d transition metals. Fig 6.1 is the XMCD absorption spectrum for Fe from the sample deposited on GaAs (110).

It is one of the most typical spectra of X-ray absorption spectroscopy (XAS) for 3d transition metals. The red and black plots represent the result for positive and negative phases of X-ray polarisation. The phase of X-ray determines the circular polarisation direction, and in this case, positive phase means the X-ray is right polarisation, while negative phase stands for the opposite. The absorption spectrum was governed by the resonances occur when 2p core electrons get excited into unoccupied 3d valence state above the Fermi level. It is important to know that 2p state is further split into $2p_{1/2}$ and $2p_{3/2}$ levels due to the spin-orbit interaction. Because these two levels have different occupation numbers of electrons, namely 2 and 4, the absorption spectra is commonly consists of two peaks. The configuration of energy band states is illustrated in Fig 6.2 for better understanding of the mechanism.

When 2p to 3d electron transitions occurs due to the influence of polarised light, the transitions also exhibits the property of polarisation. This effect is governed by the transition selection rules [79]. For a certain phase (or helicity) of polarisation, the quantity of electrons of one spin get excited into higher band states is different than those of another spin. This is the reason that there is an absorption height different for two different helicity of incoming X-ray.

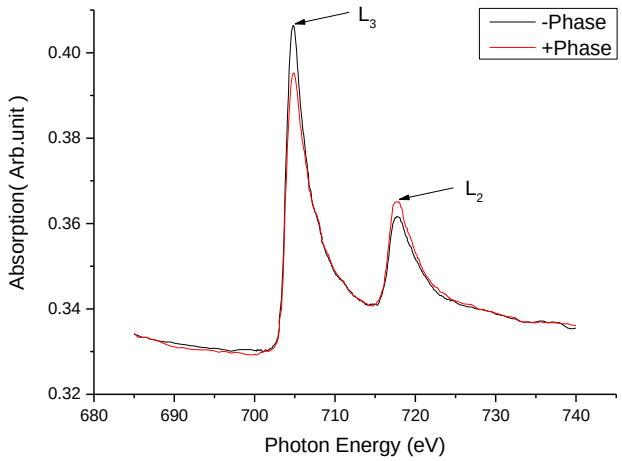

Fig 6.1. XAS of Fe in CoFeB/GaAs (110) under 2000 Oe of applied field. Two plots represents the spectra obtained for positive and negative helicity of the X-rays. The two absorption peaks occurred at the L2,3 edges respectively.

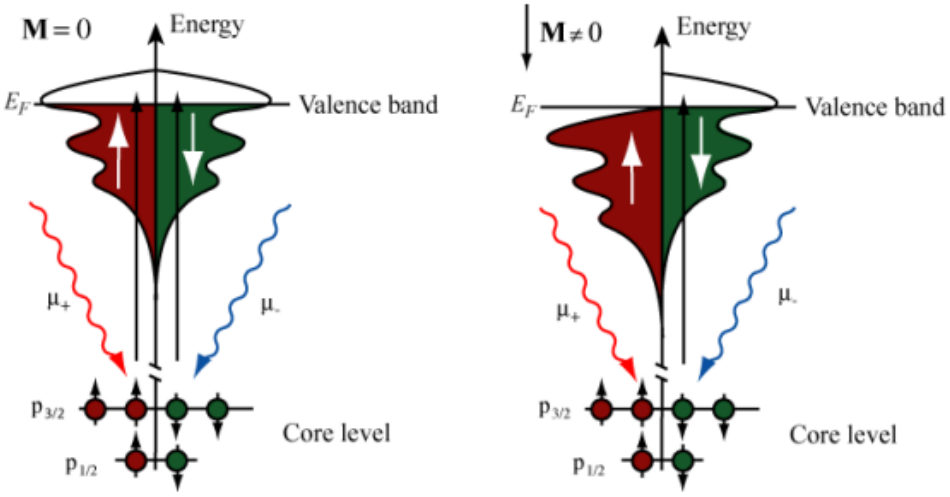

Fig 6.2. The change of spin up and spin down electrons distribution at 3d states of magnetic material when subjected under an external field and circularly polarised X-ray light.

The XMCD is calculated as the differences of the XAS of different helicities. The two non-zero peaks are exactly the absorption edges of the material. This difference can be quantitatively relate to the polarisation of the unoccupied valence density of states, which is leading to the calculation of the spin and orbital magnetic moments. This method can be summarised as the sun rules. The spin and orbital moments can be obtained by

$$\mu_L = -\frac{2}{3C}(A+B)\mu_B \qquad (6.2)$$

$$\mu_S = -\frac{1}{C}(A-2B)\mu_B \qquad (6.3)$$

where A, B are the area under the difference peaks, and C is a constant.

By denoting the height of the difference peaks as *h1* and *h2*, it can be derived from the above equations that

$$h_1 \propto \mu_L \; and \; h_1 \propto \mu_S \qquad (6.4)$$

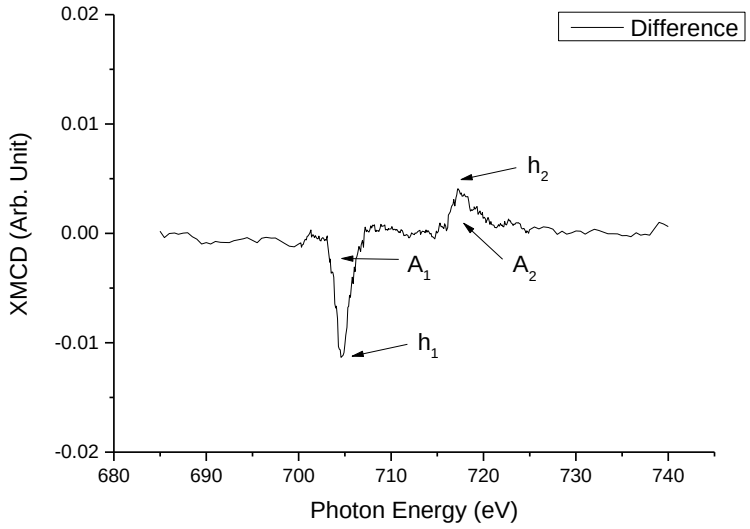

Fig 6.3. The XMCD dichroism of Fe in CoFeB/GaAs (110). It is effectively the differences of +phase and –phase plots from Fig. 6.1. The absolute value of peak height is denoted as h1 and h2, where the area covered by them are A1 and A2.

To further identify the exact value of spin and orbital moment, a method called the Sum Rules is required to be established. The Sum Rules is a well-defined quantitative approach developed precisely for the measurements of spin and orbital moments for the 3d transition metals. The theoretical approach had been pioneered by researchers in the early 1990s, and by 1995 when Chen *et al* published their experimental confirmation [80], a definite method of applying the Sum Rules had been developed.

According to the Sum Rules, the orbital and spin magnetic moments can be determined from the XAS and XMCD spectra by the following equations [81]:

$$m_{orb} = -\frac{4\int_{L3+L2}(\mu_+ - \mu_-)d\omega}{3\int_{L3+L2}(\mu_+ + \mu_-)d\omega}(10 - n_{3d}) \qquad (6.6)$$

$$m_{spin} = -\frac{6\int_{L3}(\mu_+ - \mu_-)d\omega - 4\int_{L3+L2}(\mu_+ - \mu_-)d\omega}{\int_{L3+L2}(\mu_+ + \mu_-)d\omega}(10 - n_{3d})(1 + \frac{7\langle T_z\rangle}{2\langle S_z\rangle})^{-1} \qquad (6.7)$$

Where m_{orb} and m_{spin} are the orbital and spin magnetic moments in units of $\mu_B/atom$; n_{3d} is the 3d electron occupation number of the respective transition metal atom. The L_3 and L_2 denotes the integration range. $\langle T_z\rangle$ is the expectation value of the magnetic dipole operator and $\langle S_z\rangle$ is equal to half of m_{spin} in Hartree atomic units.

To assist in the understanding and evaluation of the require XMCD integrals, Fig 6.7 gives an example that consists of 3 new terms *p*, *q*, and *r*, as the replacement of integrations in the above equations.

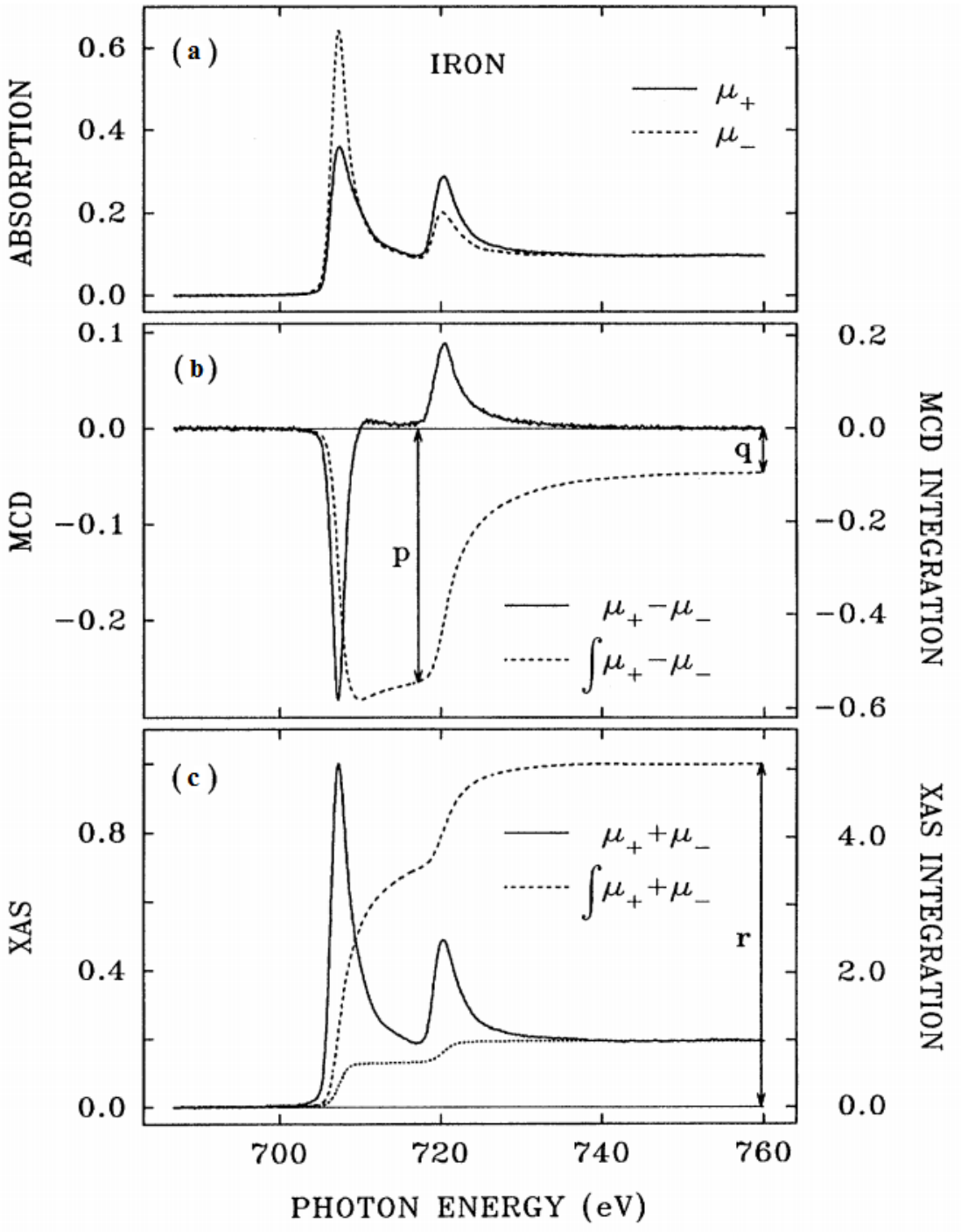

Fig 6.4 Example of Iron XAS absorption spectra

The dotted lines in Fig 6.4 indicates the integration area of XMCD and XAS spectra, whereas

$$p = \int_{L3}(\mu_+ - \mu_-)d\omega \qquad (6.8)$$

$$q = \int_{L3+L2}(\mu_+ - \mu_-)d\omega \qquad (6.9)$$

$$r = \int_{L3+L2}(\mu_+ + \mu_-)d\omega \qquad (6.10)$$

Since first-principle band structure calculations give $\langle T_z \rangle / \langle S_z \rangle$ values of -0.38% for Fe, and-0.26% for Co, this term can be neglected in the Sum Rules equation for simplification purposes. Thus, the ratio of orbital and spin moments can be stated approximately as $2q/(9p - 6q)$.

6.2.2 MAX Lab I1011 Station

MAX Lab synchrotron has been serving the researchers globally for over 25 years. The research potential of the synchrotron is based on a linear accelerator and three electron beam storage rings call MAX I, MAX II and MAX III. Each storage ring operates on different beam energies for broad area of research coverage. MAX I has the beam energy of 550 MeV, and is mainly devoted for ultra-violet wavelength and nuclear physics experiments. MAX III storage ring runs at 700 MeV. It provides synchrotron lights in the IR and UV region for advanced accelerator technology research. MAX II, the biggest and mostly used of the three, has a diameter of 90 meters and operates at 1.5 GeV of beam energy[82].

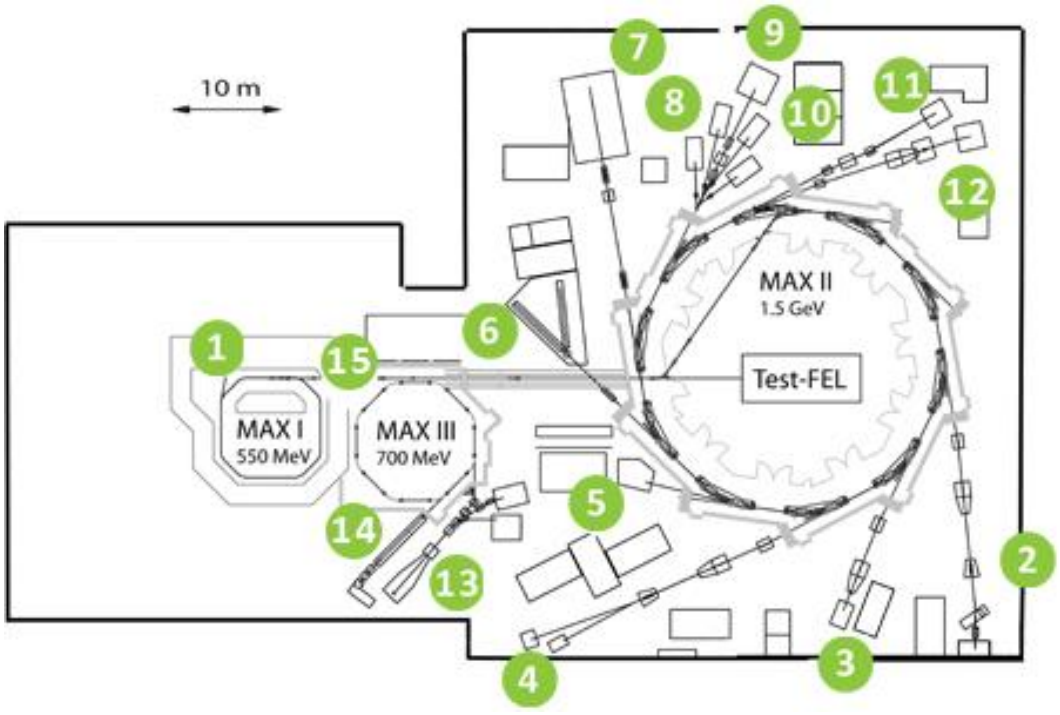

Fig 6.5. MAX Lab storage rings diagram and end station map.

MAX II storage ring started running since 1996. It was initially designed for the purpose of UV and soft X-ray researches. Over the years, 12 end stations were established along the circumference. The insertion devices also have been upgraded using superconductor magnetic undulators, allowing the production of hard X-ray light possible.

Beamline I1011 is a soft X-ray beamline at MAX II ring, with the energy range of 200-2000 eV. It uses an Elliptically Polarizing Undulator (EPU) light source to produce X-ray beams of a variable polarisation state[83]. The beamline in particular delivers high flux and brightness of X-ray light covering the L-edges of 3d elements and is therefore the best suit for this project.

Fig 6.6. Beamline I1011 intermediate section. The beam enters this section from the left end, passes through the collimating mirror, the grating monochromator chamber, a series of focusing mirror and enters the octupole station (not shown) connecting to the right end.

Another unique feature of I1011 beamline is the end station. The analysis station located at the end of the beamline is designated as the Octupole end station. An octupole UHV chamber contains eight water-cooled electromagnets were specifically engineered to offer unlimited optical accesses for the X-ray beam. These eight electromagnetic cores were spaced equidistantly over the surface of a sphere, the effective magnetic field region in the central region is a vector sum of magnetic field generated by each magnetic pole. This setup allows the magnetic field to be rotated

freely without obstruct the X-ray beam path. By working in conjunction with 5-axis manipulator and the possibility to rotate the whole chamber allows measuring the magnetic properties with effectively limitless geometry of applied field, X-ray and sample orientation.

Fig 6.7. Octupole analysis chamber. Eight magnetic coils are mounted inside of the rotating chamber in a cube-corner geometry.

6.2.3 Sample Preparation

Four samples of CoFeB thin film were produced for this project. Magnetron sputtering system were used to grow $Co_{56}Fe_{24}B_{20}$ onto GaAs (100), (110), (111); and $Co_{56}Fe_{24}B_{20}$ on InAs (001) substrates respectively. The substrates were firstly rinsed in acetone, ethanol and DI water in turn to remove bulk and organic surface contaminations, followed by a 50s wet etching in the solution of HCL:H2O (1:1) to further remove any oxides impurities[84]. After blown dry with nitrogen gun, the substrates were rapidly transferred to the UHV chamber with the base pressure of $6x10^{-8}$mbar. The substrates have undergone two stages of annealing, with the first 15 minutes under 450ºC and another 30 minutes under 580ºC. The deposition were carried out at normal incidence after the samples cooled down to room temperature. No magnetic field was applied during this process, and the Ar pressure were kept at $3x10^{-3}$mbar. The deposition rate was stabilised at 1.2nm/min until the film thickness reaches 3.5nm. A layer of 2nm Ta was later coated to prevent film oxidation.

6.3 Results and Analysis

Before conducting XMCD measurements and TEM inspections, all three samples had their hysteresis loop measured routinely. The hysteresis loops shown in Fig 6.8 was taken by VSM. And they indicate that there is strong uniaxial anisotropy for all three samples. The measurements were performed 90 degrees apart for each of the sample. The results shows that not only both of the coercivity and the saturation field of sample on GaAs(100) substrate are much larger than those of sample on another two oriented substrates, the magnetisation switch along the hard axis is clearly slower too. With the reason behind the differences remain unknown, these measurements confirms the uniaxial anisotropy of amorphous film layer grown on top of GaAs.

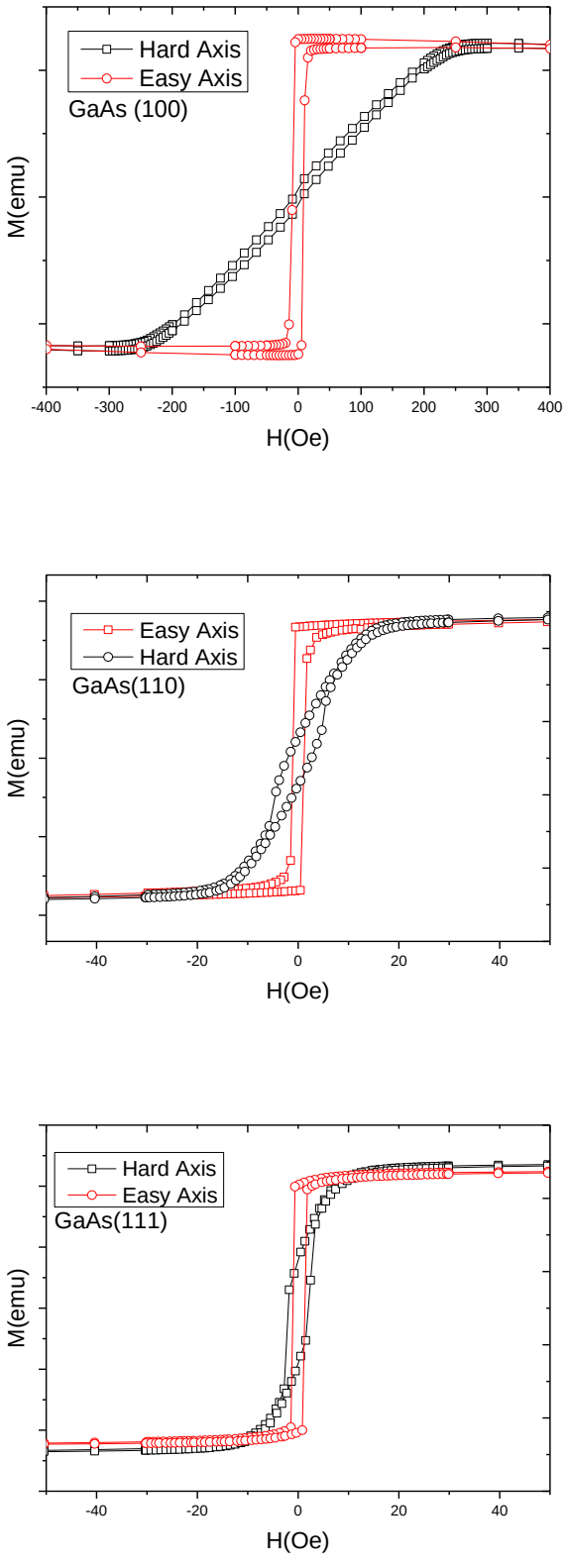

Fig 6.8 VSM hysteresis measurements along two perpendicular axis of 3.5nm CoFeB films on GaAs (100), (110) and (111) substrates.

XMCD measurements were performed at normal incidence for CoFeB/Ta films on GaAs substrate. The data is collected by Total Electron Yield (TEY) detector in the analysis chamber, under the magnetic field of 2000 Oe. The limit of magnetic field was defined as the temperature of the magnet. Higher field could be achieved by the octupole magnet but the time lapse would be greatly reduced. Consider the measurements performed on these samples requires extended time for low noise, high resolution scan, the magnetic field was set as rather low level.

The XMCD of each of the above samples under investigation was measured at both positive and negative applied field. The results were made even and plotted below, with table 6.1 summarising the calculated value of m_{orb} and m_{spin} using the Sum Rules.

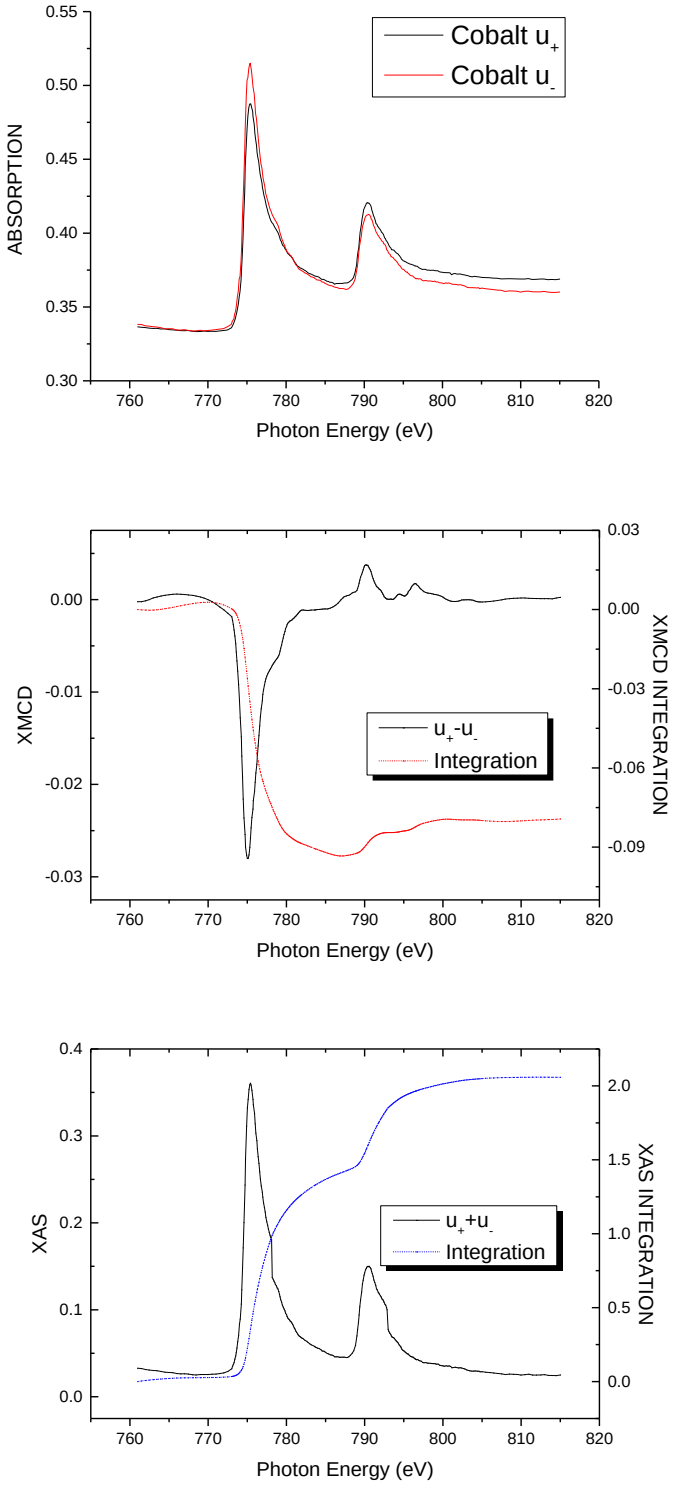

Fig 6.9 X-ray absorption of both positive and negative phases, XAS and XMCD spectra of Co for film grown on GaAs(100) substrate.

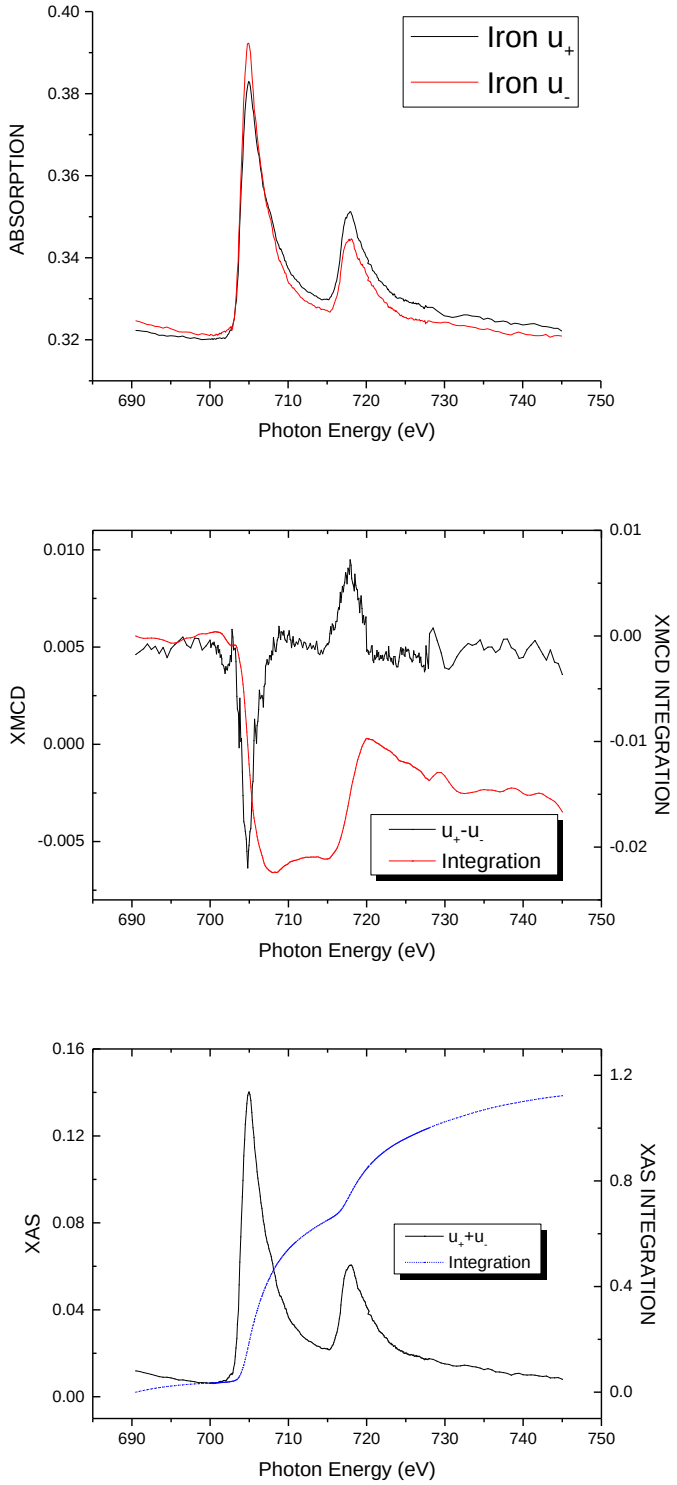

Fig 6.10 X-ray absorption of both positive and negative phases, XAS and XMCD spectra of Fe for film grown on GaAs(100) substrate.

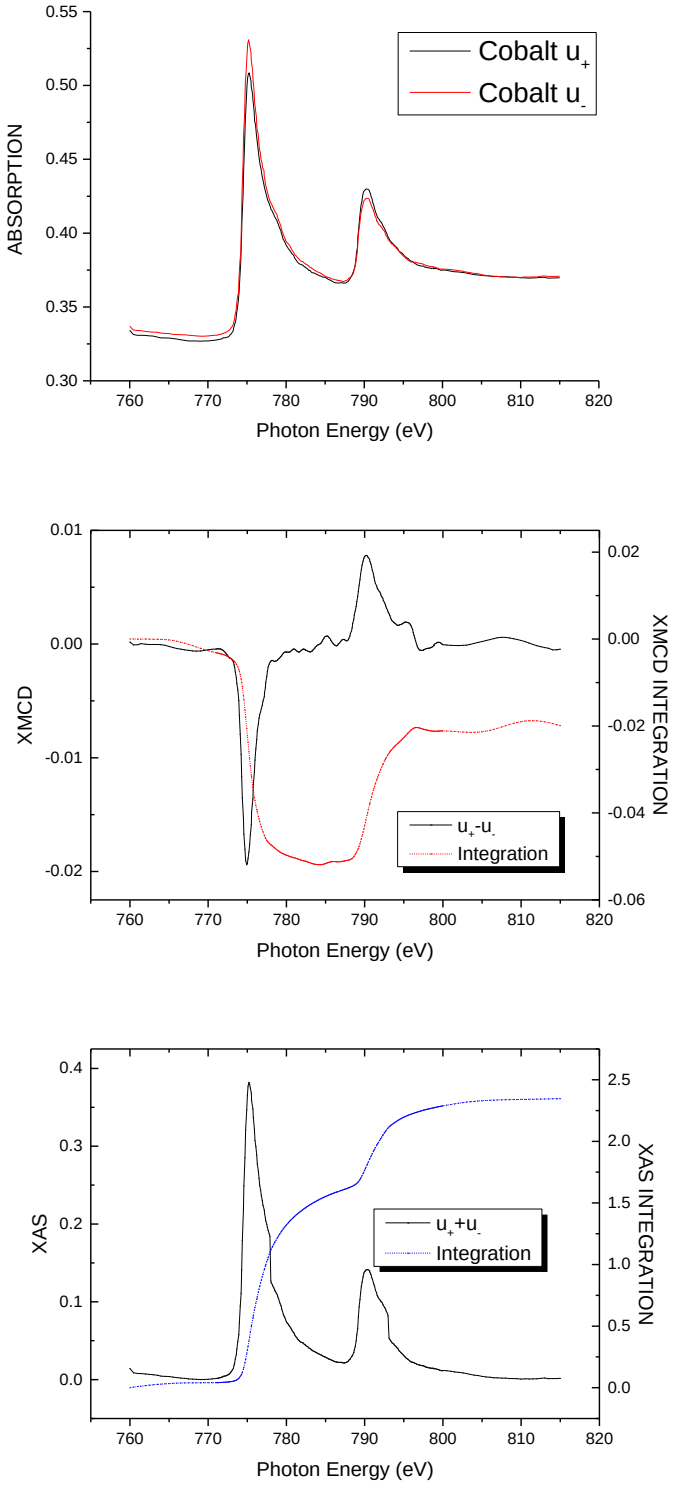

Fig 6.11 X-ray absorption of both positive and negative phases, XAS and XMCD spectra of Co for film grown on GaAs(110) substrate.

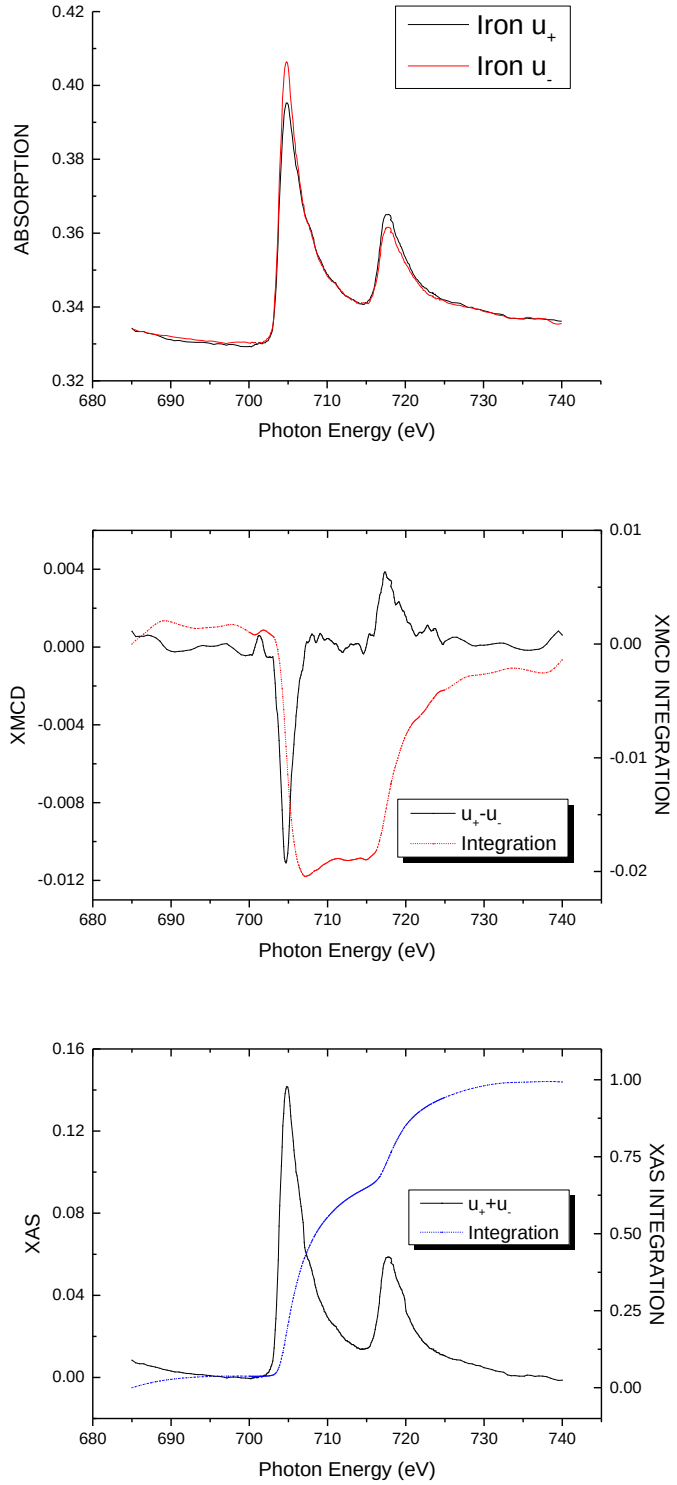

Fig 6.12 X-ray absorption of both positive and negative phases, XAS and XMCD spectra of Fe for film grown on GaAs(110) substrate.

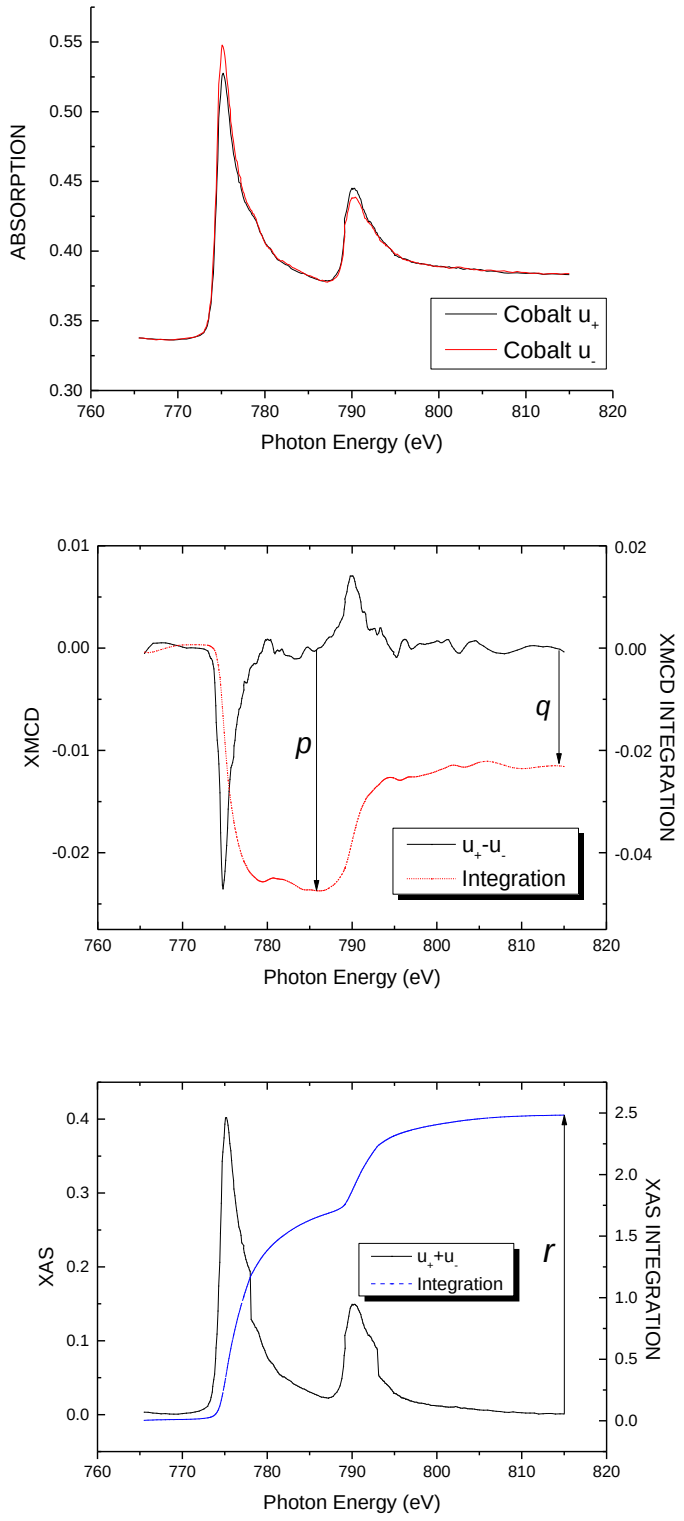

Fig 6.13 X-ray absorption of both positive and negative phases, XAS and XMCD spectra of Co for film grown on GaAs(111) substrate.

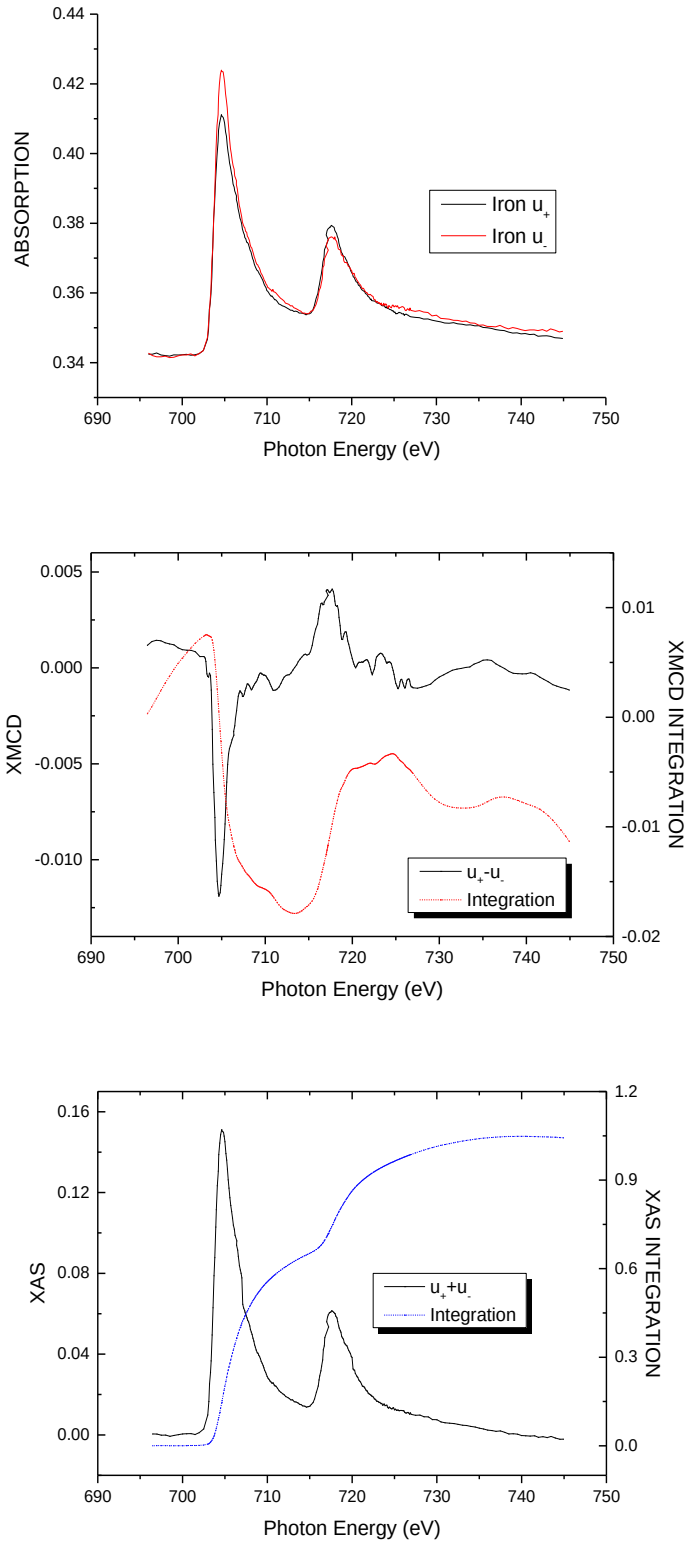

Fig 6.14 X-ray absorption of both positive and negative phases, XAS and XMCD spectra of Fe for film grown on GaAs(111) substrate.

The p, q and r value of from each of the above XMCD spectra was brought in the Sum Rules equations to evaluate the m_{orb} and m_{spin} of both Cobalt and Iron. Such results are listed here. (Unit:μ_B)

Substrate Orientation	Elements	m_{orb}	m_{spin}	m_{total}	m_{ratio}
(100)	Fe	0.05876	0.22942	0.28819	0.25614
	Co	0.12728	0.29909	0.42637	0.42557
(110)	Fe	0.01183	0.38236	0.39419	0.03095
	Co	0.02872	0.24486	0.27358	0.11727
(111)	Fe	0.03336	0.25082	0.28418	0.13299
	Co	0.03089	0.19314	0.22403	0.15922

Table 6.1 Calculated orbital and spin moment of both Fe and Co in three samples under the out-of-plane magnetic field of ±0.2T.

It is worth noticing that the measurements were taken at the normal incidence angle of X-ray beam. Additionally, the magnetic field applied was kept at 0.2T limited by the magnet of the Station. For a CoFeB film thickness of 3.5nm, such external field would not be sufficient enough to saturate the film out of the plane. The ratio of applied field to the saturation field should be the multiplicand of measured magnetic moments to the actual value. However, the ratio of the spin to orbital moments is expected to be independent of the external magnetic fields since the multiplicand applies to both of the terms. As shown in table 6.1, the values of the m_{ratio} of both the Fe and Co of the film grown on GaAs(100) are significantly larger than those of the films grown on GaAs(110) and (111). This might explain the fact that the film grown on GaAs(100) has the largest UMA, as shown by our VSM studies.

The structural properties of the sample were investigated through TEM cross-section observation. Only samples deposited on GaAs(100) and (110) were successfully prepared for TEM. It is worth mentioning that the samples for the TEM are the new sets of samples. The growth conditions were kept unchanged to the best possible. The results are shown below.

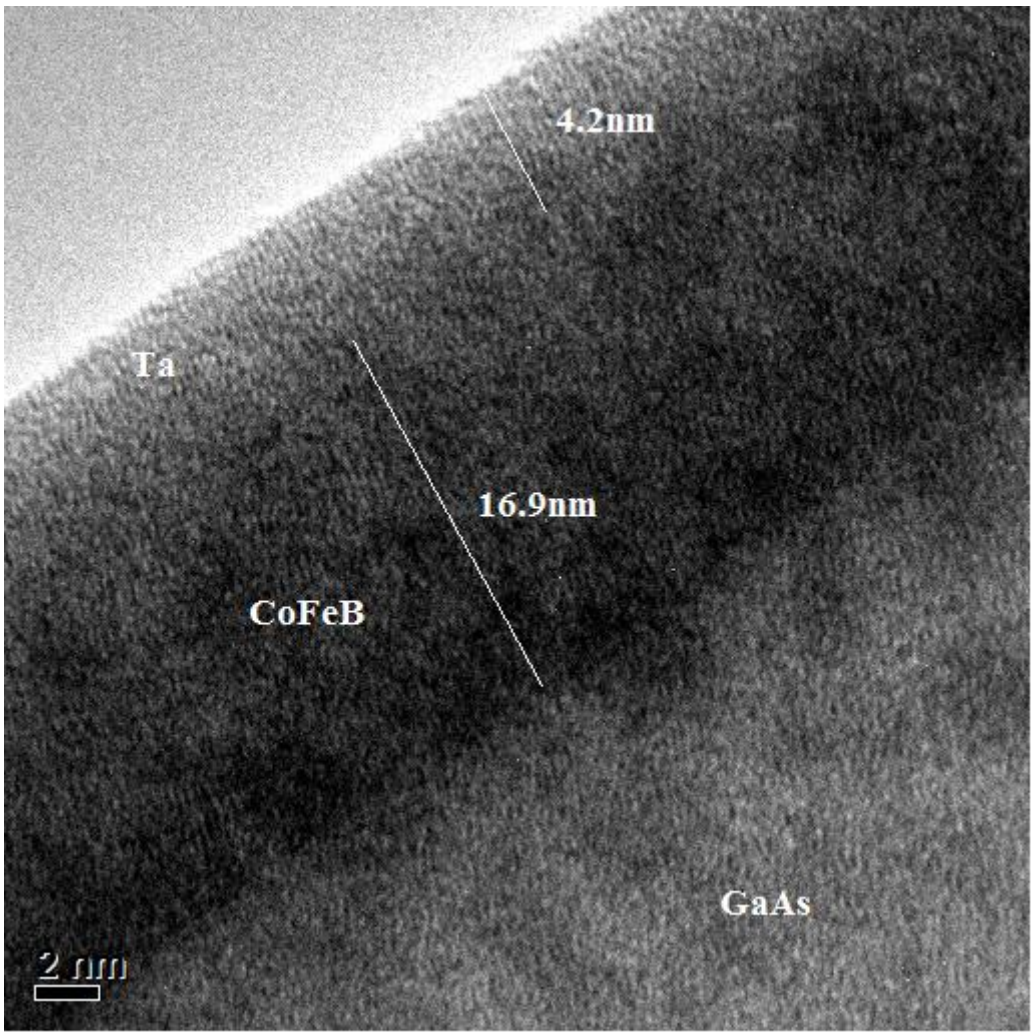

Fig 6.15. TEM cross-section of CoFeB/GaAs(100).

The film structure accumulates from the substrate region at the bottom right corner. The interface is clearly distinguishable between CoFeB film and the substrate but not so between the film and the capping layer. The total thickness of deposition is measured as 21.1nm, while the CoFeB film is approximately 16.9nm and the capping is 4.2nm.

Under this scale, one can observe that the surface of GaAs substrate is very smooth, with cross-section roughness of <0.5nm even at the worst area. The resolution of the image is not good enough to recognise the atomic orientation. This is due to the thickness of this specimen being slightly too thick.

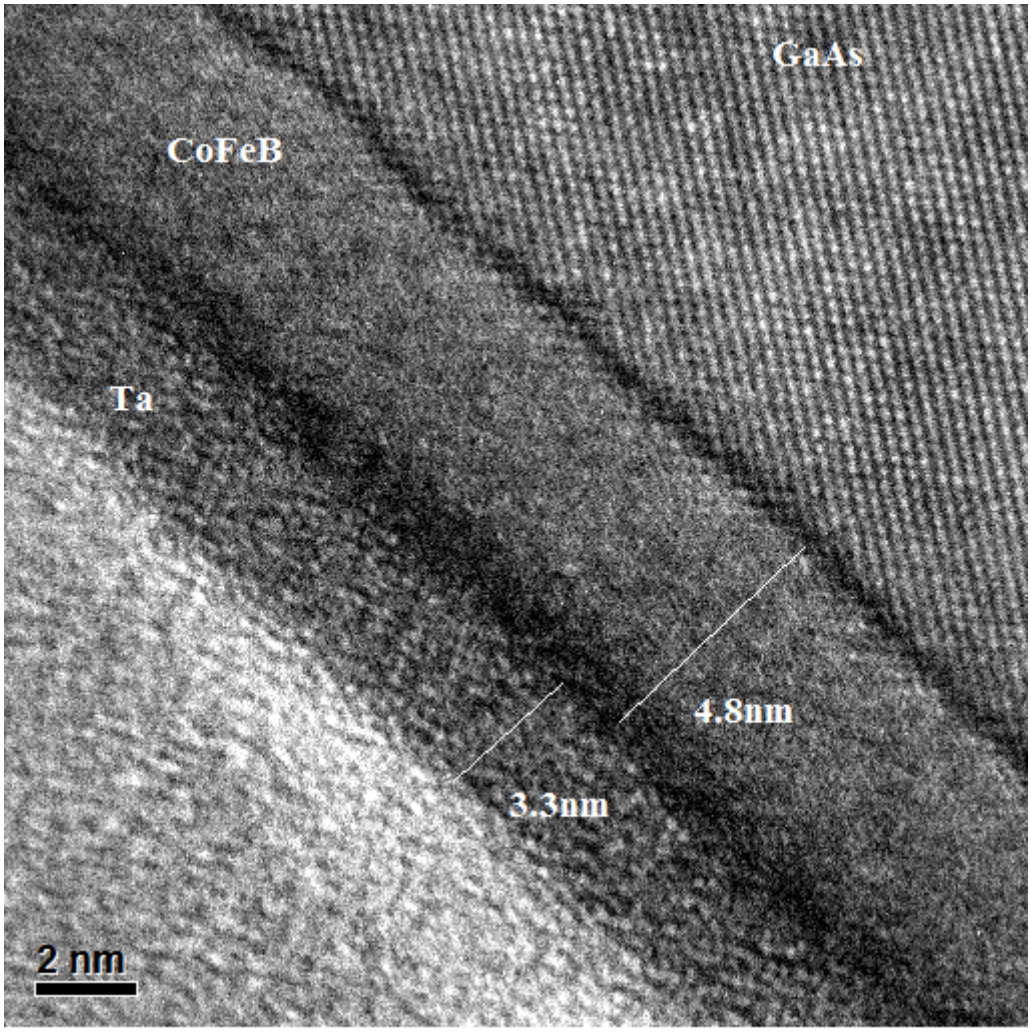

Fig 6.16. TEM cross-section of CoFeB/GaAs(110).

Another set of TEM images were taken independently for the sample on GaAs(110) substrate. At the highest resolution, this image shows that the film thickness of CoFeB is 4.8nm, and the capping is 3.3nm. The interface roughness is demonstrated again to be within very low scale. Moreover, this image clearly identifies the atomic alignment of the GaAs substrate, with each atom being distinguishable. Such alignment

terminated at the film/substrate interface due to the CoFeB being amorphous. Both images show that the FeCoB/GaAs system has a sharp interface and there is little interfusion at the interface, showing the high quality film growth of this study. Furthermore, the films are very flat, and there is magnetic shape anisotropy responsible for the UMA. This demonstrate that the UMA observed here is intrinsic and comes from the interface bonding.

6.5 Conclusion and Future Work

In this chapter, we have studied the interface structure and magnetic properties of the amorphous CoFeB on three GaAs substrates (100), (110) and (111) using a combination of VSM, XMCD and TEM techniques. Clear UMA were observed in all three sets of samples, and the UMA is the largest in CoFeB/GaAs(100). From the XMCD measurements, we found that the ratio of the spin to orbital moments of both the Fe and Co films grown on GaAs(100) are significantly larger than those of the films grown on GaAs(110) and (111). This might explain the fact that the film grown on GaAs(100) has the largest UMA. The TEM images of films grown on GaAs(100) and GaAs(110) show that the interfaces are very sharp and there is no evidence showing the magnetic shape anisotropy being responsible for the UMA. We can conclude that the UMA observed here is intrinsic and correlated with the magnetic orbital moments.

This investigation does not end here. Further research can be carried on to look into the XMCD spectra out of normal incidence. In fact, such measurements has been partially conducted but not completed due to limited access of synchrotron station. The existing data could not cover the complete picture and is thus removed from the thesis. If saturation field of the film not achievable by the magnet, a field dependency measurement could also give a plot of the change of magnetic moment against the applied field. The result could be used to suggest the possible projection of hysteresis within the range of saturation.

Chapter 7

Conclusions and Future Work

7.1 Summary of Chapter 4

Frist of all, this project has a significant amount of instrumentations, especially for the Artemis TR-ARPES project in STFC Rutherford Laboratory. One of the major contributions to the Artemis project was the establishment of MBE system. It offers the conveniences for not only the author group but also the following research groups to produce fresh samples on site. On top of that, the sample transfer mechanism between MBE and analyse chamber allows the samples to stay within UHV environment during measurement and thus eliminate the necessity of being capped.

Based on the instrumentation setup, a batch of Fe/GaAs (100) samples were prepared in order to characterise the growth condition. Longitudinal MOKE measurements were performed to confirm the epitaxial growth of Fe, and this in-situ MOKE system was also built up during this project

Spin-resolved photoemission measurements on the Fe/GaAs samples were performed, which is the world –first experiment in this area. Time-dependent photoemission spectra from the Fe valence band have been successfully collected

after a huge amount of work in improving both the hardware and software of the TR-ARPES system during my PhD work. However, the predicted change of the density of states around the Fermi level was too small to be resolved with current energy resolution.

7.2 Summary of Chapter 5

Fe/GaAs(100)

Two GaAs substrate were treated using the same recipe except that one of them had an extra ion-milling etching process before film deposition. The impact of such process to the substrate surface were confirmed both using AFM and RHEED. The chemically etched sample has sharp RHEED patterns and flat surface, thus the development of ferromagnetism was earlier comparing with the other. The ion-milling etched substrate RHEED patter indicates that there were nano clusters formed on the surface and a mixture of single and poly crystalline phase were formed.

Though the film on ion-milling etch substrate could be poly crystalline dominant, and had its ferromagnetism appeared at a later stage, the uniaxial magnetic anisotropy was clear. The MOKE results indicates that, with the oxidation layer being sputtered off from the surface, the enhanced chemical bonding between Fe-As and Fe-Ga could be an important factor to the development of UMA. Thus, for when required in the application of Fe/GaAs based devices, the interface cleanness is critical in prior to roughness.

Ni/GaAs(100)

Two Ni/GaAs samples were produced under different annealing temperature. Such process differed the substrate with surface residuals as Arsenide and its oxides decomposes at higher temperature. For both of the cases, the Ni films turned to be polycrystalline only. Single crystalline was not achieved under this condition. The author also discovered that the ferromagnetism development was delayed for 5nm of deposition on an Arsenide-rich surface, however the relaxation process was unusual.

The polycrystalline film exhibits certain degree of anisotropy along [011], [010] and [0-11] axes, and it can possibly be uniaxial anisotropy. The origin of such effect could be from the interface region as well.

7.3 Summary of Chapter 6

CoFeB on GaAs (001), (110) and (111)

Three samples were prepared using the identical recipe of magnetron sputtering growth on three orientations of GaAs substrates. The impact initialised from the substrate was addressed element-specifically. Such impact was expressed as the change of XMCD *L3* absorption edge height, which is proportional to the magnetic moment of the corresponding element.

The XAS and MCD data were deep analysed using integration and the sum rules approach. The processed data give an indication of the magnetic orbital and spin moments of both Fe and Co element within the film. Though the samples were not measured under the saturation field, the ratio of the two moments should maintain at the same level, thus the comparison between different substrate orientations is reasonable. The unquenched magnetic orbital moment could be related to the origin of the UMA but the conclusion could not be drawn from here.

TEM cross section inspections indicate that the film structure is as expected and the interface between the CoFeB film and GaAs substrate are clear and shape. The surface roughness was kept at the minimum, and there is no strong sign of deep inter-fusion between the two materials. The images also showed no evidence of shape anisotropy since the film is clearly amorphous. The one remaining possible reason for its UMA behaviour is once again presumed from the interface bonding. This also matches previous research results published by other groups.

7.4 Future work

Further to the conclusions drawn in the thesis, there are still lots of open questions. For further research purposes, it is suggested that the following ideas to be considered.

For Artemis project, even though the UHV growth facilities have been successfully established, the zero time-delay between the XUV probe and the pump pulse have been precisely located, the Magnetic linear dichroism have been performed with minimum noise level and the time-resolve photoemission has been performed, the desired signal was not observed after all. It is assumed that an undesirable level of oxidation on the sample surface has prevented time-consuming measurements to be conducted thoroughly. It is worth stressing that any future run will certainly implement in-situ surface cleaning and structure characterisation equipment to yield high quality data.

For Magnetic Film disposition on GaAs, the success was only limited at sample preparation and MOKE measurement. We have found the magnetic properties difference from differently treated substrates. However, the exact impact of ion-milling induced surface roughness to the film properties definitely worth further experiments to identify. Ideas such like producing a double side sample with half of the surface ion-milled could be a promising method of avoiding switching between two samples and eliminating unavoidable errors. Furthermore, processing parameters such as ion-milling time span and gas flow can be adjusted to define the depth of ion milling. Films deposited onto different surface reconstruction could express different properties too, thus various annealing temperature can be involved as another factor for multi-sampling.

For the XMCD measurements of CoFeB. There are a few more measurements can be done to strengthen the results. The samples can be measured at a much larger magnetic

field, one that is big enough to reach to the saturation point. The spectra taken at that point would give confirmed data to calculate the orbital and spin magnetic moments of each elements. Furthermore, the incident angle of X-ray beam can be tilted to be not perpendicular to the sample surface plane. Measurements like this would offer the in-plane magnetic moments information of the samples, and could be put into comparison to with the out-of-plane data.

Last but not the least, since all the experiments are heavily dependent to the performance and condition of the equipment, any improvements done to them are welcome to ease the operator's trouble. Powerful processing capabilities, reliable and reasonable design of the hardware and cleaver design of user interface can further improve the lab efficiency which could bring more opportunities for greater discoveries.

Appendices

Film Growth Processes

Based on the growth rate obtained from calibration; if the emission current of the evaporator and the position of the sample substrate are maintained at the same value, the same growth rate could be achieved.

Detailed film growth processes are listed as follows. The only difference is the deposition time, which is linear to the total thickness of the film.

Sample loading

Prepare a clean substrate piece and secure it on the molybdenum sample plate.

The valve between load lock and growth chamber must be completed sealed. Stop the turbo pump of load lock. It takes a few minutes for rotation blade slowing down from 1500 Hz to 1200 Hz. Small amount of nitrogen will be send to the load lock steadily after 1200 Hz to further slow the blade down quickly.

Once the pressure of load lock is close to atmosphere level, open the gate flange and load the sample plate on the transferring arm head slot. Rotate the transfer arm for 90˚ to take the control and reseal the gate flange firmly.

Restart the turbo pump of load lock and the rotation speed will slowly increase back to 1500 Hz. Wait for a few more minute for the vacuum to recover before opening the gate valve to the growth chamber. The best pressure the load lock can achieve is 8.8×10^{-9} mbar; however it could take days to pump down to that limit. In order to make the

minimum effect to the growth chamber vacuum, it is suggested to wait till the load lock pressure to drop below $1x10^{-7}$ mbar.

Sample transfer I

Once the pressure in load lock is good enough. The gate valve to the growth chamber can be opened for 1st stage sample transfer. Since the load lock chamber is badly contaminated comparing with the UHV environment in the growth chamber, it is ideal to make the transfer as fast as possible.

Lift up the manipulator to its highest position, and adjust rotary drive to 115˚ so that the sample stage slot is aligned to the sample plate.

Send the transfer arm forward till the sample stage springs catch the molybdenum plate. Micro adjustment is required to push the sample plate to the end position. Rotate the transfer arm for another 90˚ will release the sample plate.

Draw back transfer arm and close the gate valve completely.

Annealing

Connect the current supply to e-beam heating filament and high voltage supply to the sample plate. Power on the thermal meter to monitor the temperature.

Gradually increase the filament current to 2.4 A and start the initial annealing.

When the pressure stops increasing or starts to drop, turn on the high voltage supply and start high temperature annealing. The voltage limit is set to be 650 V.

After 60 minutes, the annealing is completed. Switch off both current and high voltage supply and let the temperature drop to room temperature.

Iron film deposition

Rotate the manipulator to 315˚ to allow the back of sample stage facing the evaporator. Connect current and voltage supplies to evaporator.

Gradually increase the filament current to 5.0 A, then turn on the voltage supply and set the high voltage to 700 V.

Gradually adjust the depth of source rod using the linear motion drive till the emission current increases to 15 mA.

Turn over the sample stage 180˚ and start the recording of film deposition.

The emission current must be maintained close to 15 mA to ensure the flux density and growth rate.

Sample transfer II

When the desired film thickness is acquired, turn off the current and high voltage supply for evaporator.

Lower the manipulator to lower transfer arm stage. And pick up the sample plate using the main transfer arm. The locking mechanism is exactly the same as the upper one.

Open the gate valve between growth chamber and main chamber, and the sample plate can be now transferred to the main chamber manipulator stage.

Sample withdraw

The sample withdraw process is exactly the same as loading process, only in a reversed order. It is very important to minimize the opening time of all gate valves to avoid too much cross contamination between different chambers.

XAS and XMCD Spectra

Sample Ta(2nm)/CoFeB(3.5nm)/GaAs(100)

-0.2T Co

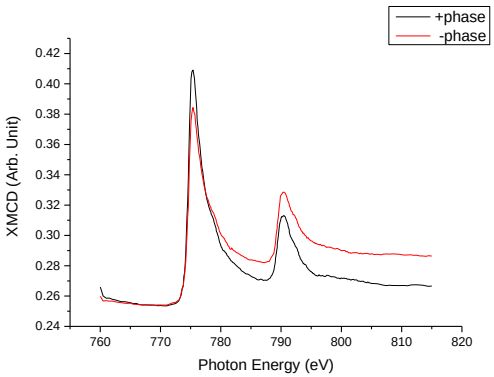

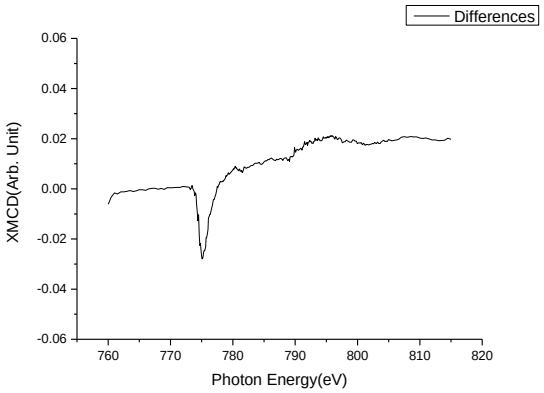

+0.2T Co

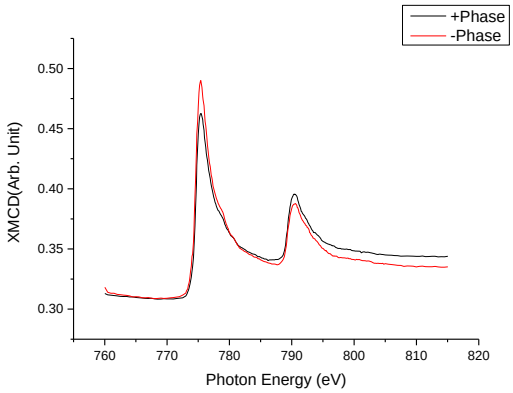

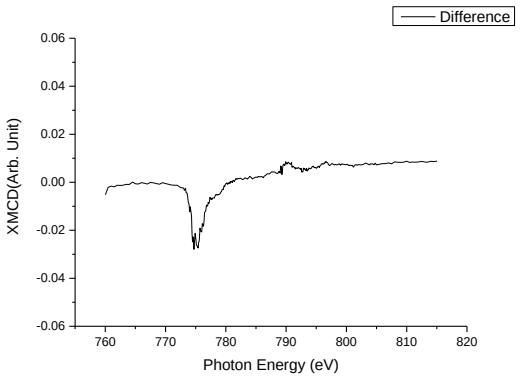

-0.2T Fe

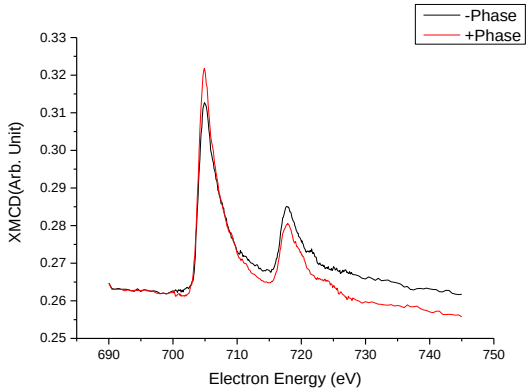
-Phase
+Phase
XMCD(Arb. Unit)
Electron Energy (eV)

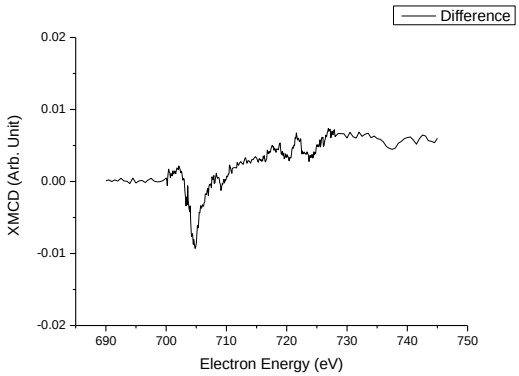
Difference
XMCD (Arb. Unit)
Electron Energy (eV)

+0.2T Fe

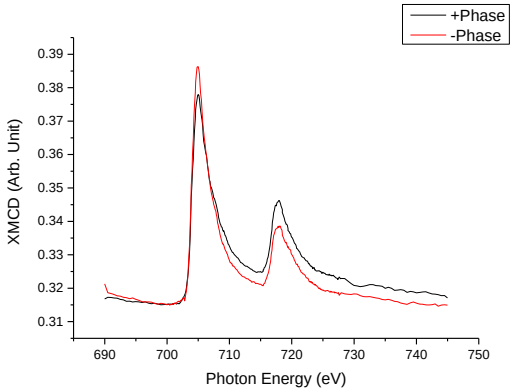
+Phase
-Phase
XMCD (Arb. Unit)
Photon Energy (eV)

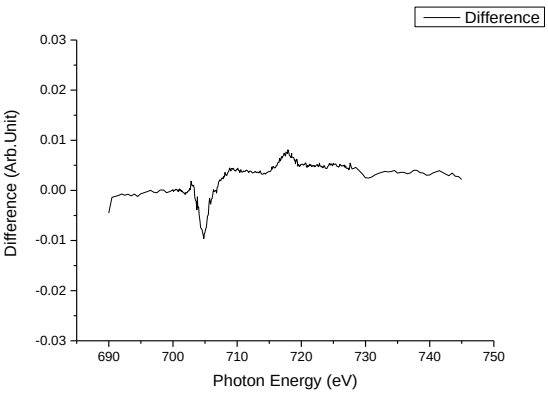
Difference
Difference (Arb.Unit)
Photon Energy (eV)

Sample Ta(2nm)/CoFeB(3.5nm)/GaAs(110)

-0.2T Co

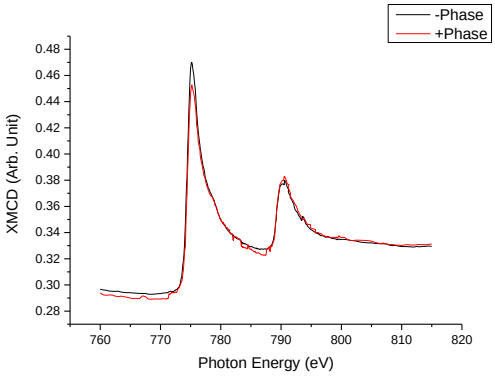

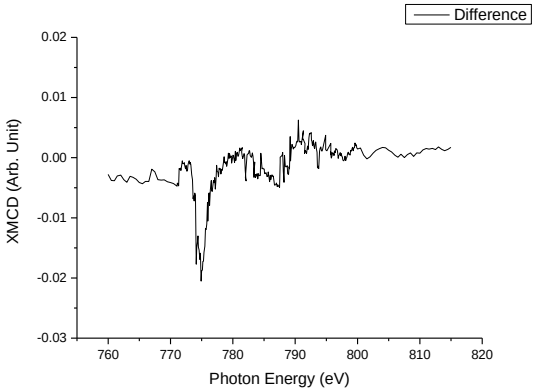

-0.2T Fe

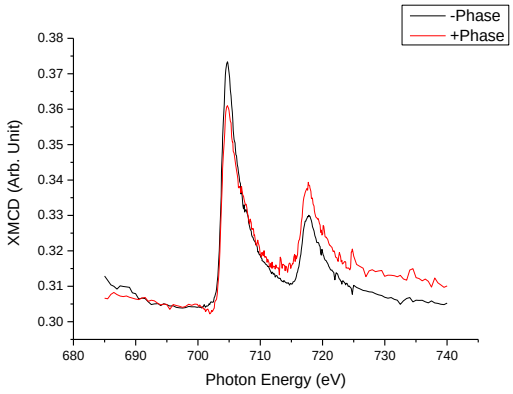

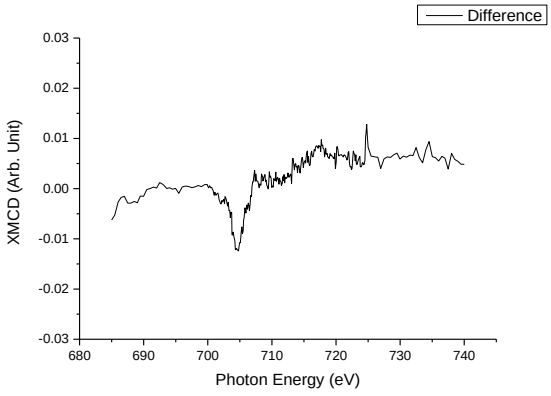

+0.2T Fe

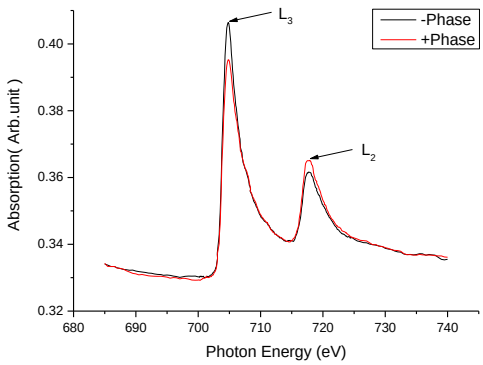
L3
L2
-Phase
+Phase
Absorption(Arb.unit)
Photon Energy (eV)

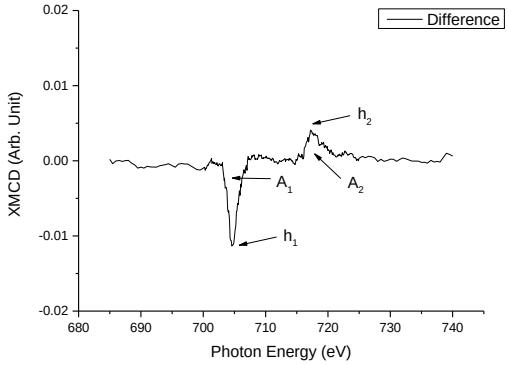
Difference
h2
A1
A2
h1
XMCD (Arb. Unit)
Photon Energy (eV)

+0.2T Co

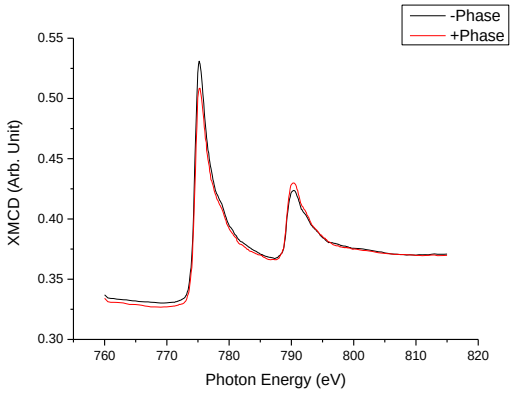
-Phase
+Phase
XMCD (Arb. Unit)
Photon Energy (eV)

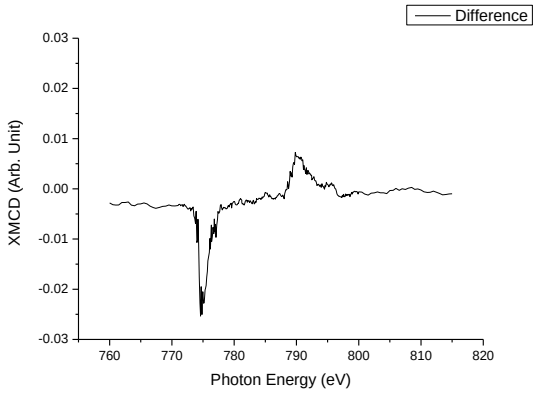
Difference
XMCD (Arb. Unit)
Photon Energy (eV)

Sample Ta(2nm)/CoFeB(3.5nm)/GaAs(111)

+0.2T Co

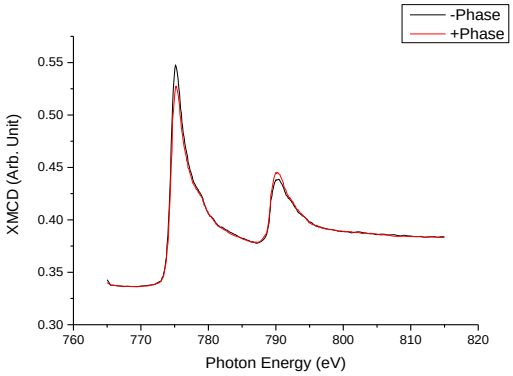

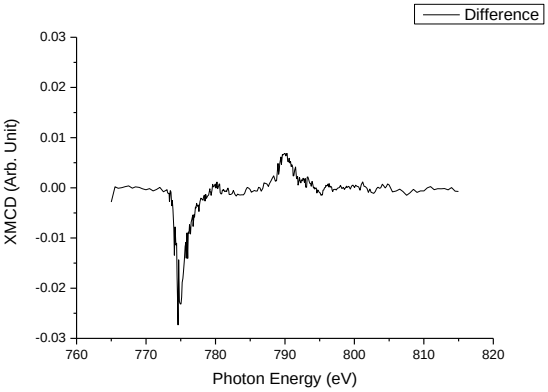

-0.2T Co

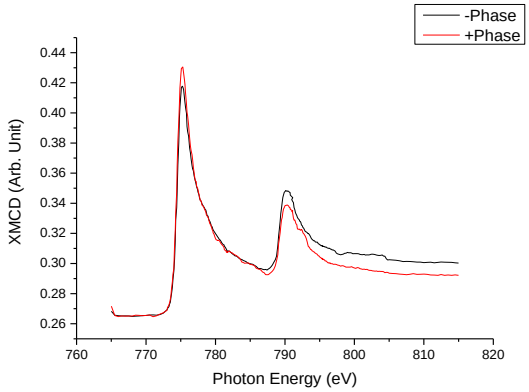
-Phase
+Phase
XMCD (Arb. Unit)
Photon Energy (eV)

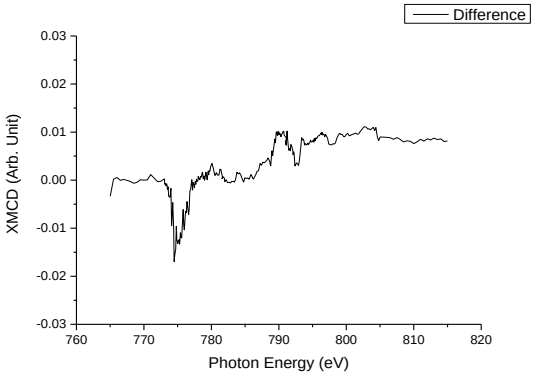
Difference
XMCD (Arb. Unit)
Photon Energy (eV)

+0.2T Fe

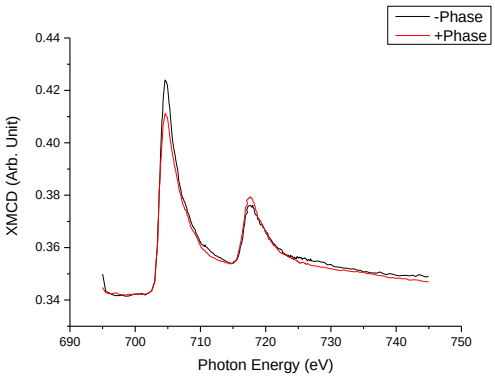
-Phase
+Phase
XMCD (Arb. Unit)
Photon Energy (eV)

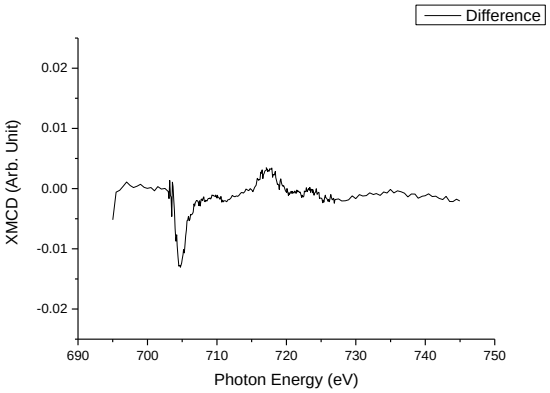
Difference
XMCD (Arb. Unit)
Photon Energy (eV)

Sample Ta(2nm)/CoFeB(3.5nm)/InAs(100)

+0.3T Co

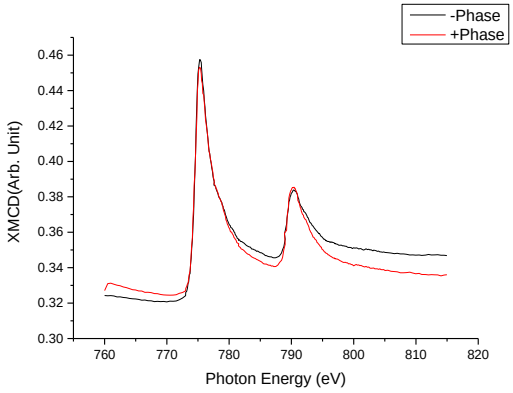

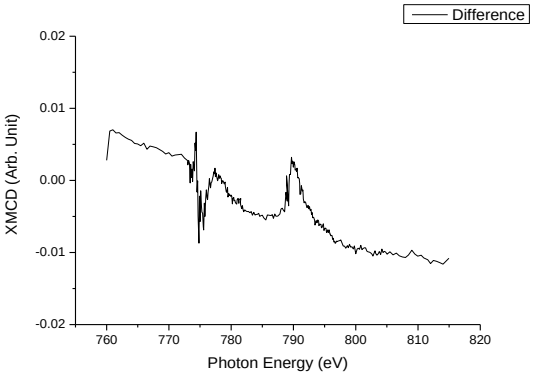

-0.3T Co

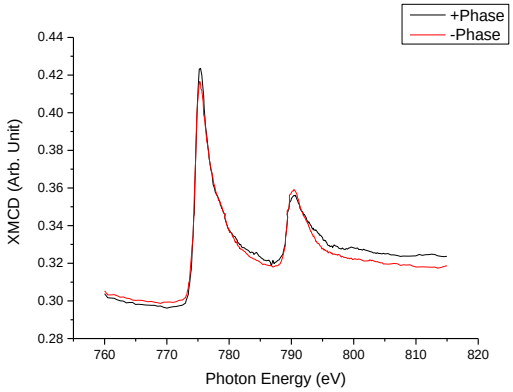

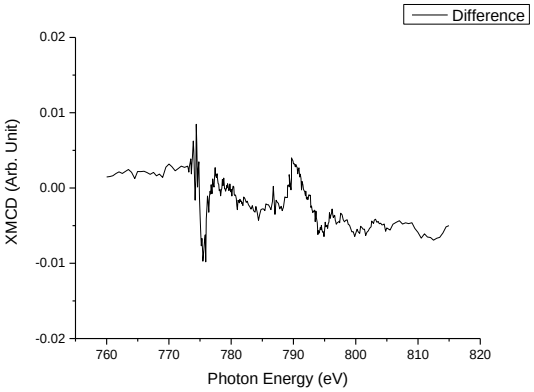

+0.3T Fe

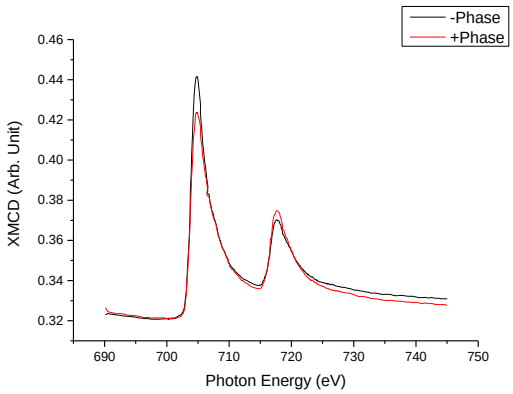
-Phase
+Phase
XMCD (Arb. Unit)
Photon Energy (eV)

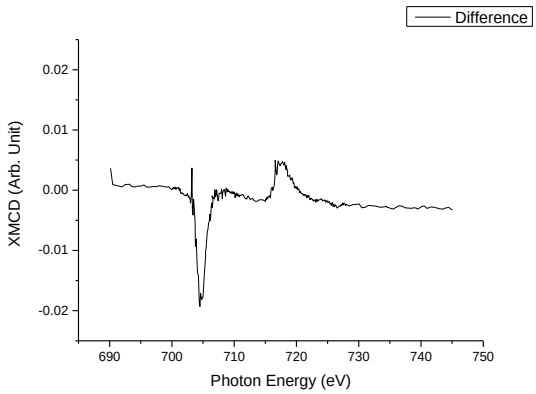
Difference
XMCD (Arb. Unit)
Photon Energy (eV)

-0.3T Fe

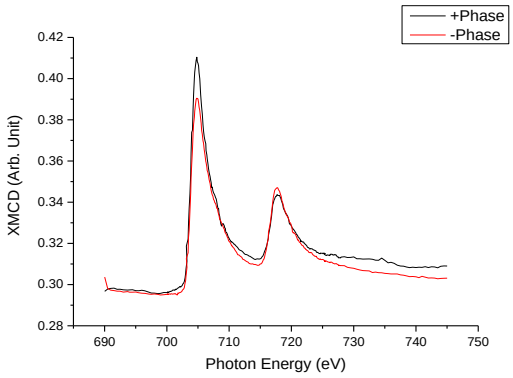
+Phase
-Phase
XMCD (Arb. Unit)
Photon Energy (eV)

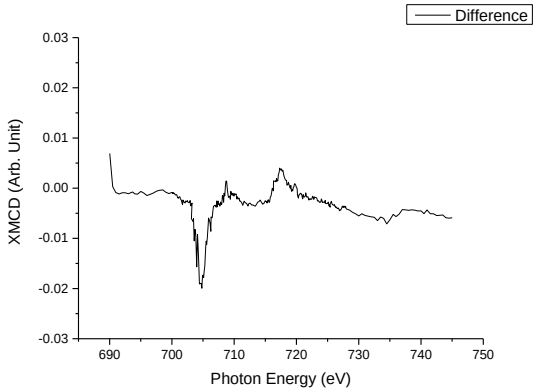
Difference
XMCD (Arb. Unit)
Photon Energy (eV)

Sample Ta(2nm)/CoFeB(3.5nm)/InAs(100) Field Dependency

3500Oe

Fe

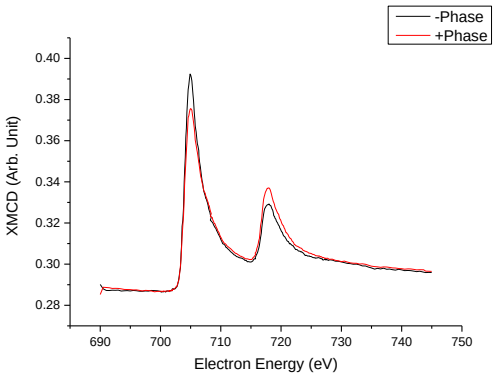

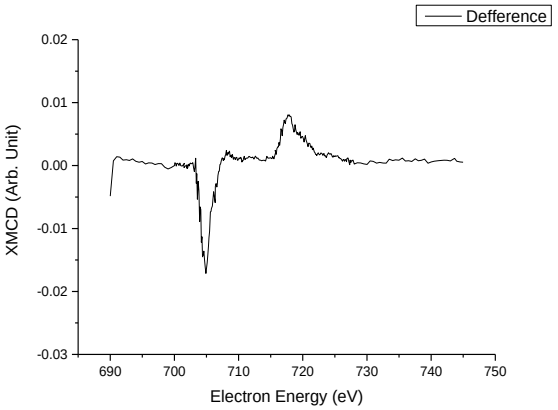

Co

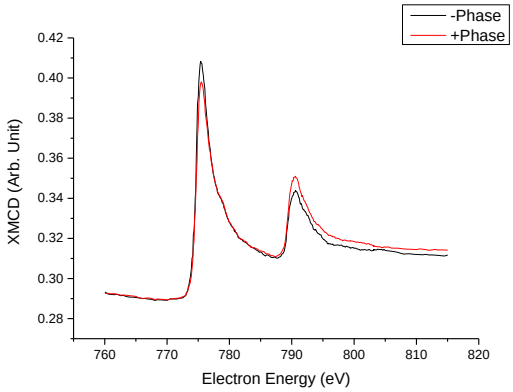

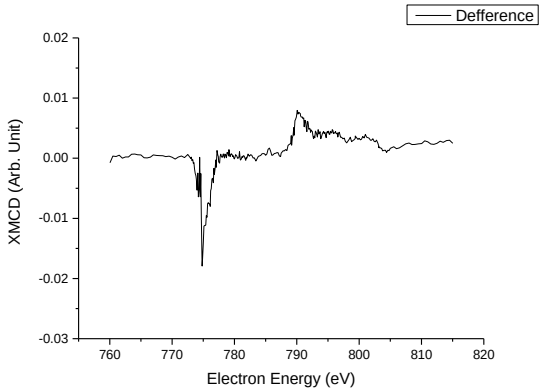

3000Oe

Fe

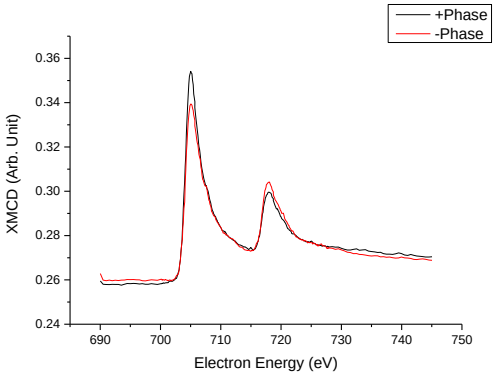
+Phase
-Phase
XMCD (Arb. Unit)
Electron Energy (eV)

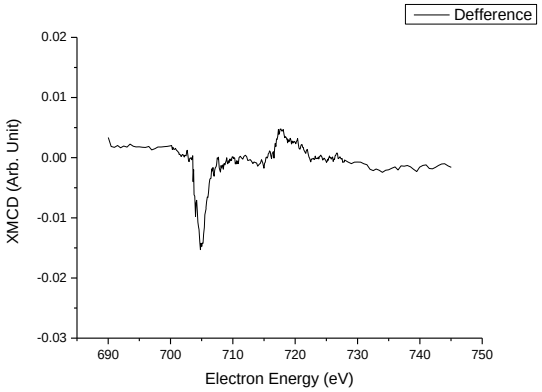
Defference
XMCD (Arb. Unit)
Electron Energy (eV)

Co

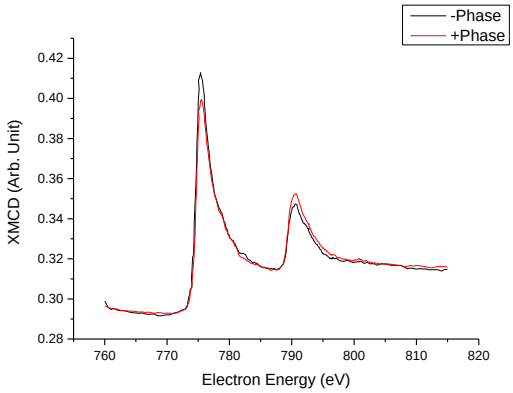
-Phase
+Phase
XMCD (Arb. Unit)
Electron Energy (eV)

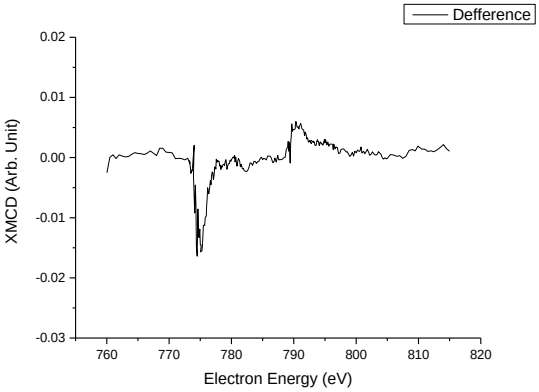
Defference
XMCD (Arb. Unit)
Electron Energy (eV)

2500Oe

Fe

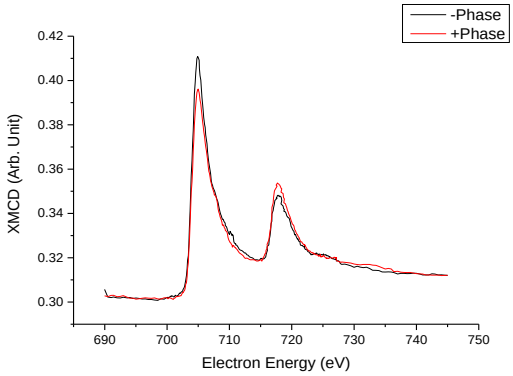
-Phase
+Phase
XMCD (Arb. Unit)
Electron Energy (eV)

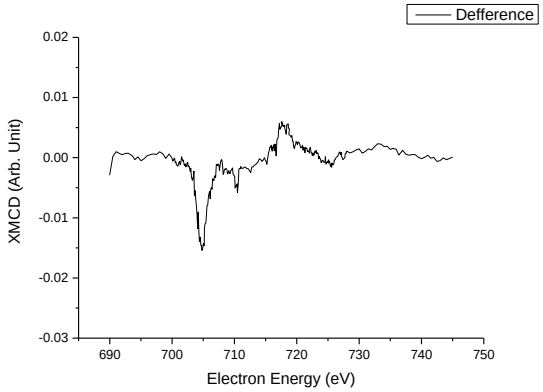
Defference
XMCD (Arb. Unit)
Electron Energy (eV)

Co

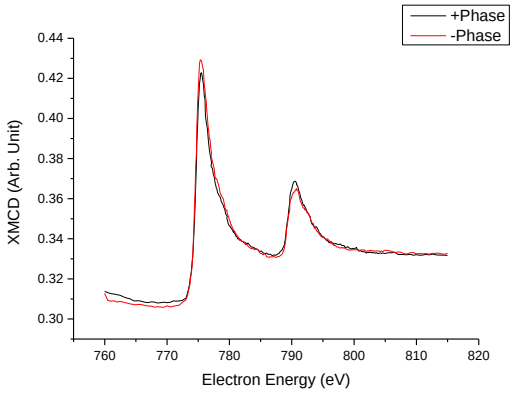
+Phase
-Phase
XMCD (Arb. Unit)
Electron Energy (eV)

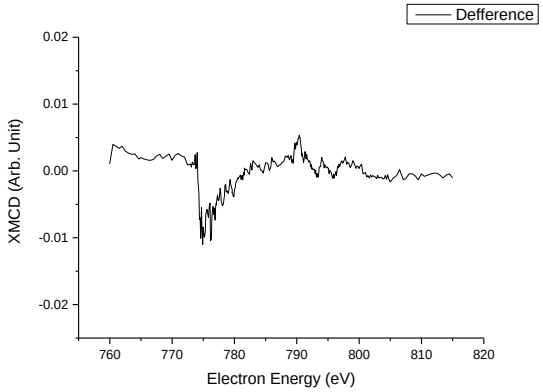
Defference
XMCD (Arb. Unit)
Electron Energy (eV)

2000Oe

Fe

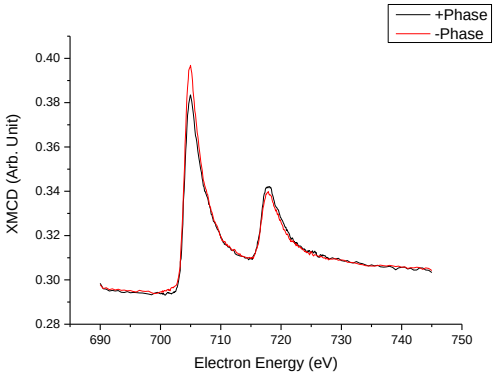
+Phase
-Phase
XMCD (Arb. Unit)
Electron Energy (eV)

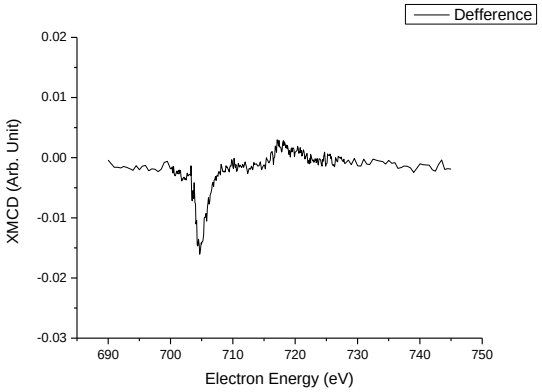
Defference
XMCD (Arb. Unit)
Electron Energy (eV)

Co

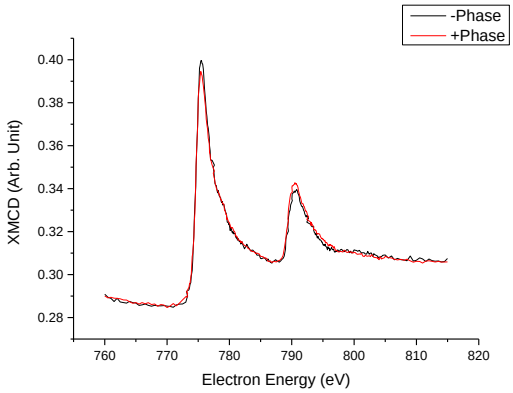
-Phase
+Phase
XMCD (Arb. Unit)
Electron Energy (eV)

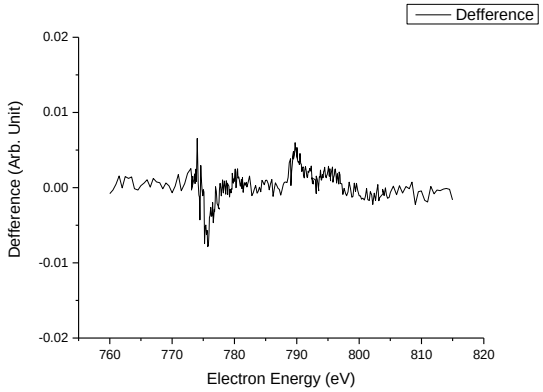
Defference
Defference (Arb. Unit)
Electron Energy (eV)

1500Oe

Fe

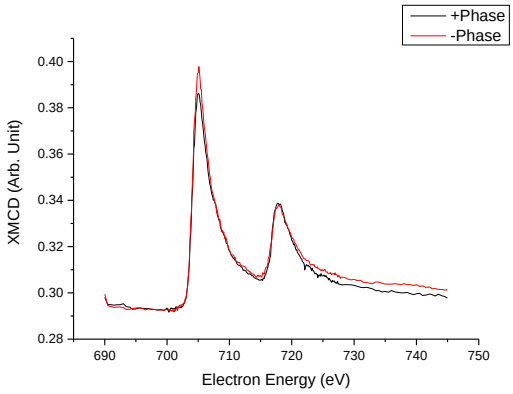
+Phase
-Phase
XMCD (Arb. Unit)
Electron Energy (eV)

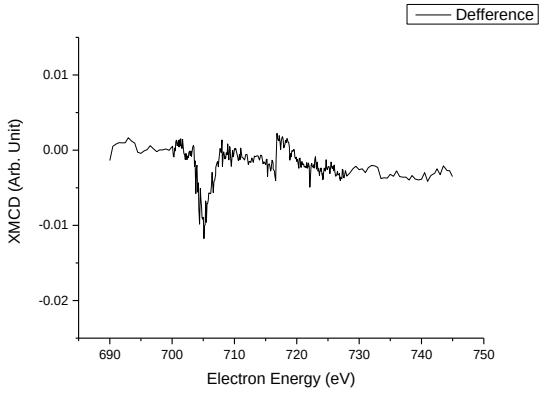
Defference
XMCD (Arb. Unit)
Electron Energy (eV)

Co

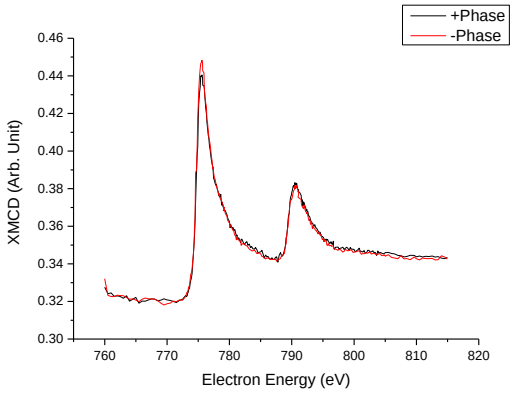
+Phase
-Phase
XMCD (Arb. Unit)
Electron Energy (eV)

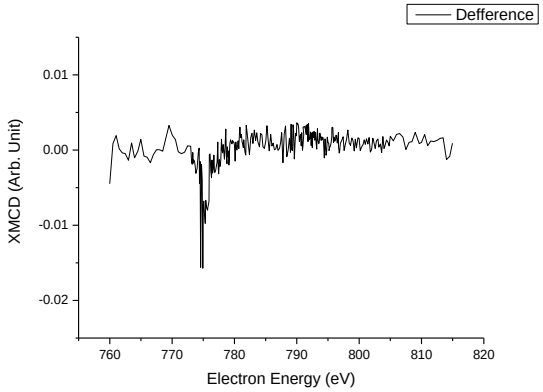
Defference
XMCD (Arb. Unit)
Electron Energy (eV)

1000Oe

Fe

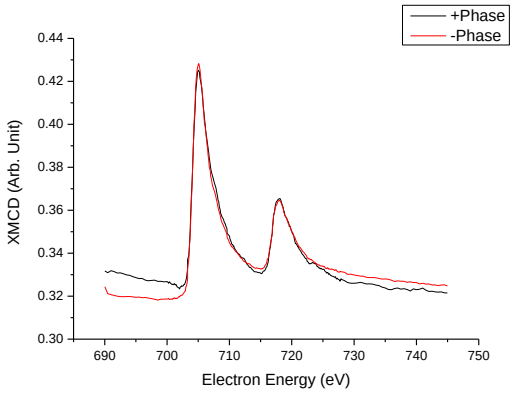
+Phase
-Phase
XMCD (Arb. Unit)
Electron Energy (eV)

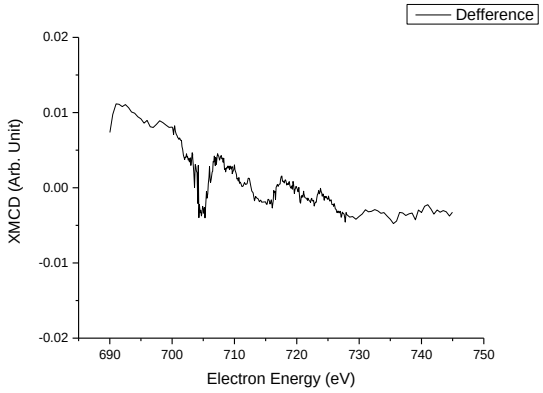
Defference
XMCD (Arb. Unit)
Electron Energy (eV)

Co

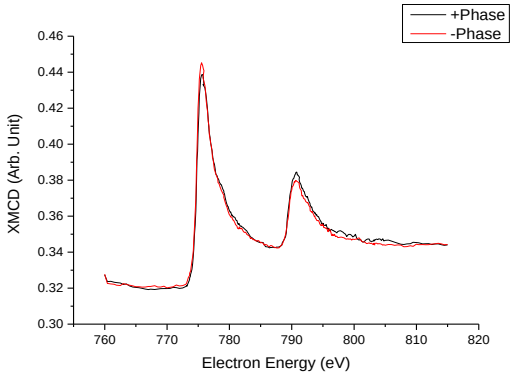
+Phase
-Phase
XMCD (Arb. Unit)
Electron Energy (eV)

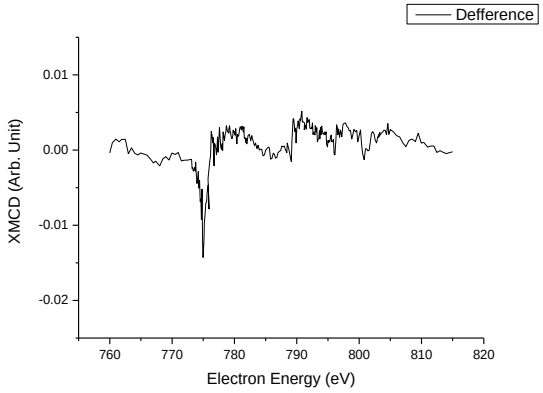
Defference
XMCD (Arb. Unit)
Electron Energy (eV)

500Oe

Fe

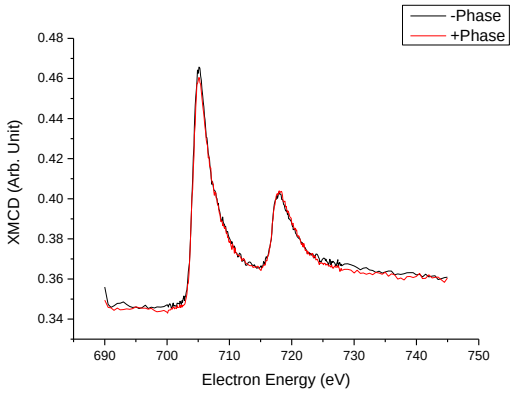
-Phase
+Phase
XMCD (Arb. Unit)
Electron Energy (eV)

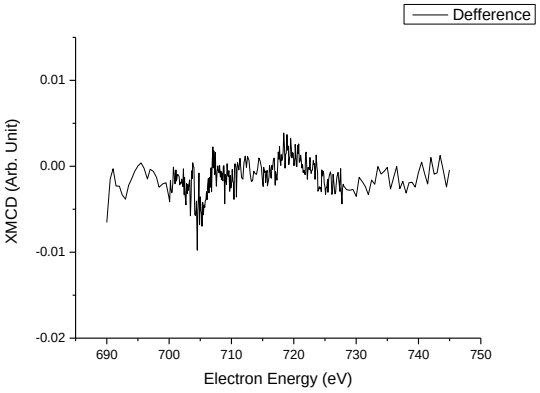
Defference
XMCD (Arb. Unit)
Electron Energy (eV)

Co

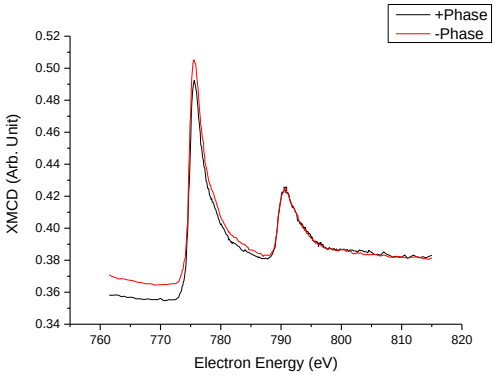
+Phase
-Phase
XMCD (Arb. Unit)
Electron Energy (eV)

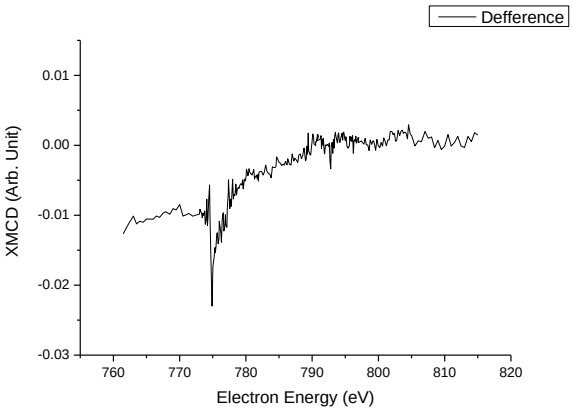
Defference
XMCD (Arb. Unit)
Electron Energy (eV)

List of Abbreviations

BBO	Barium Borate Oxide (BaB_2O_4)
Bcc	Bulk centred cubic
CVD	Chemical Vapour deposition
DI	De-ionized (water)
DW	Domain Wall
Ems	Electron microscopes
EDX	Energy Dispersive X-ray Spectroscopy
Fcc	Face Centred Cubic
FET	Field Effect Transistor
FM	Ferromagnetic
GMR	Giant Magneto resistance
HM	Half-Metallic
IT	Information Technology
IPA	Iso-Propyl Alcohol
LED	Light Emitting Diode
LEED	Low-Energy Electron Diffraction
MBE	Molecule Beam Epitaxy

MOKE	Magneto-Optical Kerr Effect
ML	Monolayer
MR	Magneto resistance
OM	Optical Microscope
PLD	Pulse Laser Deposition
RHEED	Reflection High-Energy Electron Diffraction
RAM	Random Access Memory
RT	Room Temperature
SQUID	Superconducting Quantum Interference Device
SEM	Scanning Electron Microscope
TEM	Transmitting Electron Microscope
TSP	Titanium Sublimation Pumps
TMR	Tunnel Magneto resistance
UHV	Ultra-High Vacuum
VSM	Vibrating Sample Magnetometer
XUV	Extreme Ultra Violet
XAS	X-ray Absorption Spectra
XMCD	X-ray Magnetic Circular Dichroism

References

1 M. N. Baibich et al, Phys. Rev. Lett. 61. 2472 (1988).

2 D D Awschalom and M. E. Flatte, Nature Physics 3, 153 (2007).

3 E. I. Rashba, Phys. Rev. B 62, R16267 (2000).

4 H. J. Zhu, M. Ramsteiner, H. Kostial, M. Wassermeier, H.-P. Schönherr, and K. H. Ploog, Phys. Rev. B 87, 016601 (2001).

5 A. H. Morrish, The Physical Principles of Magnetism, USA: John Wiley & Sons, Inc. (1965).

6 B. D. Cullity, Introduction to Magnetic Materials, USA: Addison-Wesley Publishing Co.(1972).

7 B. M. Moskowitz, "Hitchhiker's Guide to Magnetism," Available http://www.irm.umn.edu/hg2m/hg2m_index.html.

8 B. Heinrich, J. A. Bland, Ultrathin Magnetic Structures, UK: Spinger-Verlag, (1994).

9 E. Beaurepaire, J. C. Merle, A. Daunois, J. Y. Bigot, Phys. Rev. Lett. 76, 4250 (1996).

10 B. Koopmans, M. V. Kampen, J. T. Kohlhepp and W. J. M. de Jonge, Phys. Rev. Lett. 85 844 (2000). T. Kampfrath, R. G. Ulbrich, F. Leuenberger, M. Munzenberg, B. Sass, and W. Felsch, Phys. Rev. B 65, 104429 (2002). J. Y. Bigot, L. Guidoni, E. Beaurepaire, and P. N. Saeta, Phys. Rev. Lett. 93 077401-1, (2004). R. Gomez-Abal, O. Ney, and K. Satitkovitchai, Phys. Rev. Lett. 92, 227402-1, (2004). G. P. Ju, et al, Phys. Rev. Lett. 94, 087202, (2005). . Wilks, R. J. Hicken, M. Ali, and B. J. Hickey, J. Appl. Phys. 97, 10A705, (2005). C.D. Stanciu, F. Hansteen, A. V. Kimel, A. Tsukamoto, A. Itoh, and Th. Rasing, Phys. Rev. Lett. 99, 047601 (2007).

11 B. Koopmans, G. Malinowski, F. Dalla Longa, D. Steiauf, M. Fähnle, T. Roth, M. Cinchetti, and M. Aeschlimann, Nature Mater., 9 (2010) 259.

12 M. Wietstruk, A. Melnikov, C. Stamm, T. Kachel, N. Pontius, M. Sultan, C. Gahl, M. Weinelt, H.A. Dürr, and U. Bovensiepen, Phys. Rev. Lett., 106 (2011) 127401.

13 Uwe Bovensiepen, J. Phys. Cond. Matt. 19, 083201 (2007).

14 C. Stamm, T. Kachel, N. Pontius, R. Mitzner, T. Quast, K. Holldack, S. Khan, C. Lupulescu, E. F. Aziz, M. Wietstruk, H. A. Durr, and W. Eberhardt, Nature Materials, vol 6, 740 (2007).

15 G. A. Prinz et al, J. Appl. Phys. 53 (1982) 2087.

16 J. J. Krebs et al, J. Appl. Phys. 61 (1987) 2596.

17 E. H. Rhoderick, and R. H. Williams, "Metal-semiconductor contacts", Oxford University Press, Oxford, (1988).

18 Y. B. Xu, E. T. M. Kernohan, M. Tselepi, J. A. C. Bland and S. Holmes, Appl. Phys. Lett. 73 (1998) 399.

19 J. J. Krebs et al, J. Appl. Phys. 61 (1987) 2596.

20 J. M. Florczak and E. D. Dahlberg, Phys. Rev. B 44 (1991) 9338.

21 A. Filipe, A. Schuhl and P. Galtier, Appl. Phys. Lett. 70 (1997) 129.

22 E. M. Kneeler, B. T. Jonker, P. M. Thibado, R. J. Wagner, B. V. Shanabrook, and L. J. Whitman,, Phys. Rev. B 56 (1997) 8163.*

23 Y. B. Xu E. T. M. Kernohan, D. J. Freeland, A. Ercole, M. Tselepi and J. A. C. Bland,, Phys. Rev. B 58 (1998) 890.

24 J. S. Claydon et al, IEEE Trans. on Magnetics, (2005), to be published.

25 M. Brockmann, M. Zölfl, S. Miethaner, G. Bayreuther, 198, 384 (1999).

26 Y. B. Xu et al, J. Appl. Phys. 87 (2000) 6110, and Y. B. Xu et al, Phys. Rev. B 62, 1167. (2000)

27 E. Ahmad et al, J. Appl. Phys., 95, 6555 (2004)

28 N. A. Morley et al., J Appl Phys. 99, 08N508, 2006

29 C. J. Gutierrez, G. A. Prinz, J. J. Krebs, M. E. Filipkowski, V. G. Harris and W. T. Elam, J. Magn. Magn. Mater. 126, 232 (1993).

30 W. X. Tang, D. Qian, D. Wu, Y. Z. Wu, G. S. Dong, X. F. Jin, S. M. Chen, X. M. Jiang, X. X. Zhang and Z. Zhang, J. Magn. Magn. Mater. 240, 404 (2002).

31 C. S. Tian, D. Qian, D. Wu, R. H. He, Y. Z. Wu, W. X. Tang, L. F. Yin, Y. S. Shi, G. S. Dong, X. F. Jin, X. M. Jiang, F. Q. Liu, H. J. Qian, K. Sun, L. M. Wang, G. Rossi, Z. Q. Qiu and J. Shi, Phys. Rev. Lett. 94, 137210 (2005).

32 C. Scheck, P. Evans, G. Zangari, and R. Schad, Appl. Phys. Lett. 82, 2853 (2003).

33 C. Scheck, Y.-K. Liu, P. Evans, R. Schad and G. Zangari, J. Appl. Phys. 95, 6549 (2004).

34 Joy George, (1992), "Preparation of thin films", Marcel Dekker, Inc.

35 D.V. Morgan and K. Board, (1990), "An Introduction to semiconductor Microtechnilogy", 2nd edition, British Library Cataloguing in Publication Data.

36 http://www.wafertech.co.uk/products/categories-off-orientation/

37 http://cnx.org/content/m25712/latest/

38 Wikipedia, "Transmission Electron Microscopy", Retrieved Nov, 2010, from: http://en.wikipedia.org/wiki/Transmission_electron_microscopy

39 Semitracs. "Transmission Electron Microscopy", Retrieved Nov, 2010, from: http://www.semitracks.com/index.php/reference-material/failure-and-yield-analysis/materials-characterization/tem

40 J.Kerr, Phil. Mag. 3,321 (1877).

41 G. A. Prinz et al, J. Appl. Phys. 53, 2087(1982).

42 J. J. Krebs et al, J. Appl. Phys. 61, 2596(1987).

43 J. M. Florczak and E. D. Dahlberg, Phys. Rev. B 44, 9338(1991).

44 A. Filipe, A. Schuhl and P. Galtier, Appl. Phys. Lett. 70, 129 (1997).

45 E. M. Kneeler, B. T. Jonker, P. M. Thibado, R. J. Wagner, B. V. Shanabrook, and L. J. Whitman,, Phys. Rev. B 56, 8163(1997).

46 Y. B. Xu E. T. M. Kernohan, D. J. Freeland, A. Ercole, M. Tselepi and J. A. C. Bland,, Phys. Rev. B 58, 890(1998).

47 M. Brockmann et al, J. Magn. Magn Mater. 198, 384(1999).

48 S. Datta, B. Das, et al., Appl. Phys. Lett. 56 665 (1990).

49 I Appelbaum, B. Huang , D. J. Monsma, Nature, Vol 447, p. 295 (2007).

50 O. M. J. van 't Erve, A. L. Friedman, E. Cobas, C. H. Li, J. T. Robinson, B. T. Jonker, Nature Nanotechnology 7, 737 (2012).

51 A. Lahave, M. Eizenberg, Y Komem, J.Appl.Phys. 60 (3) 1986;

52 W.X. Tang, Journal of Magnetism and Magnetic Materials 240 (2002) 404-406;

53 C.S. Tian, PRL 94, 137210 (2005);

54 S.A. Haque, Journal of Magnetism and Magnetic Materials 226-230 (2001) 1591-1593;

55 S.A. Haque, Physica B 325 (2003) 259-264

56. Lu C, Lu X, Jin F, Yan Y, Yan L, Wu J, et al. The Effect of GaAs Substrate Treatment on the Magnetic Properties in Fe/GaAs(100). submitted to IEEE TRANSACTIONS ON MAGNETICS 2015.

57. Hindmarch A, Kinane C, MacKenzie M, Chapman J, Henini M, Taylor D, et al. Interface Induced Uniaxial Magnetic Anisotropy in Amorphous CoFeB Films on AlGaAs(001). Physical Review Letters 2008, 100(11).

58. Hindmarch AT, Rushforth AW, Campion RP, Marrows CH, Gallagher BL. Origin of in-plane uniaxial magnetic anisotropy in CoFeB amorphous ferromagnetic thin films. Physical Review B 2011, 83(21).

59. Wang D, Nordman C, Daughton JM, Qian Z, Fink J. 70% TMR at Room Temperature for SDT Sandwich JunctionsWith CoFeB as Free and Reference Layers. IEEE TRANSACTIONS ON MAGNETICS 2004, 40: 2269-2271.

60. Kubota H, Fukushima A, Yakushiji K, Nagahama T, Yuasa S, Ando K, et al. Quantitative measurement of voltage dependence of spin-transfer torque in MgO-based magnetic tunnel junctions. Nature Physics 2008, 4(1): 37-41.

61. Lee YM, Hayakawa J, Ikeda S, Matsukura F, Ohno H. Giant tunnel magnetoresistance and high annealing stability in CoFeB/MgO/CoFeB magnetic tunnel junctions with synthetic

pinned layer. Applied Physics Letters 2006, 89(4): 042506.

62. Ikeda S, Miura K, Yamamoto H, Mizunuma K, Gan HD, Endo M, et al. A perpendicular-anisotropy CoFeB-MgO magnetic tunnel junction. Nature materials 2010, 9(9): 721-724.

63. Stöhr J. X-ray magnetic circular dichroism spectroscopy of transition metal thin films. Journal of Electron Spectroscopy and Related Phenomena 1995, 75: 253-272.

64. Stohr J. Exploring the microscopic origin of magnetic anisotropies with X-ray magnetic circular dichroism (XMCD) spectroscopy. J Magn Magn Mater 1999, 200(1-3): 470-497.

65. Kuch W. X-ray magnetic circular dichroism for quantitative element-resolved magnetic microscopy. Phys Scripta 2004, T109: 89-95.

66. BEAMLINE I1011 Information- Available from: https://www.maxlab.lu.se/node/39

67. Kowalik IA, Öhrwall G, Jensen BN, Sankari R, Wallén E, Johansson U, et al. Description of the new I1011 beamline for magnetic measurements using synchrotron radiation at MAX-lab. Journal of Physics: Conference Series 2010, 211: 012030.

68. Cui B, Song C, Wang YY, Yan WS, Zeng F, Pan F. Tuning of uniaxial magnetic anisotropy in amorphous CoFeB films. Journal of physics Condensed matter : an Institute of Physics journal 2013, 25(10): 106003.

69. Lu C, Lu X, Jin F, Yan Y, Yan L, Wu J, et al. The Effect of GaAs Substrate Treatment on the Magnetic Properties in Fe/GaAs(100). submitted to IEEE TRANSACTIONS ON MAGNETICS 2015.

*70. Hindmarch A, Kinane C, MacKenzie M, Chapman J, Henini M, Taylor D, et al. Interface Induced Uniaxial Magnetic Anisotropy in Amorphous CoFeB Films on AlGaAs(001). Physical Review Letters 2008, **100**(11).*

*71. Hindmarch AT, Rushforth AW, Campion RP, Marrows CH, Gallagher BL. Origin of in-plane uniaxial magnetic anisotropy in CoFeB amorphous ferromagnetic thin films. Physical Review B 2011, **83**(21).*

*72. Wang D, Nordman C, Daughton JM, Qian Z, Fink J. 70% TMR at Room Temperature for SDT Sandwich JunctionsWith CoFeB as Free and Reference Layers. IEEE TRANSACTIONS ON MAGNETICS 2004, **40:** 2269-2271.*

*73. Kubota H, Fukushima A, Yakushiji K, Nagahama T, Yuasa S, Ando K, et al. Quantitative measurement of voltage dependence of spin-transfer torque in MgO-based magnetic tunnel junctions. Nature Physics 2008, **4**(1)**:** 37-41.*

*74. Lee YM, Hayakawa J, Ikeda S, Matsukura F, Ohno H. Giant tunnel magnetoresistance and high annealing stability in CoFeB/MgO/CoFeB magnetic tunnel junctions with synthetic pinned layer. Applied Physics Letters 2006, **89**(4)**:** 042506.*

*75. Ikeda S, Miura K, Yamamoto H, Mizunuma K, Gan HD, Endo M, et al. A perpendicular-anisotropy CoFeB-MgO magnetic tunnel junction. Nature materials 2010, **9**(9)**:** 721-724.*

76. Stöhr J. X-ray magnetic circular dichroism spectroscopy of transition metal thin films. Journal of Electron Spectroscopy and Related Phenomena 1995, ***75:*** *253-272.*

77. Stohr J. Exploring the microscopic origin of magnetic anisotropies with X-ray magnetic circular dichroism (XMCD) spectroscopy. J Magn Magn Mater 1999, ***200****(1-3)****:*** *470-497.*

78. Kuch W. X-ray magnetic circular dichroism for quantitative element-resolved magnetic microscopy. Phys Scripta 2004, ***T109:*** *89-95.*

79. Surface-enhanced Raman spectroscopy: a brief retrospective. Journal of Raman spectroscopy. 2005, volume 36, issue 6-7, pages 485-496.

80. Experimental Confirmation of the X-Ray Magnetic Circular Dichroism Sum Rule for Iron and Cobalt. Physical review letters. 3July 1995, volume 75, number 1.

81. Tuning of uniaxial magnetic anisotropy in amorphous CoFeB films. Journal of physics:Condensed Matter2013,106003(9pp)

82. BEAMLINE I1011 Information- Available from: https://www.maxlab.lu.se/node/39

83. Kowalik IA, Öhrwall G, Jensen BN, Sankari R, Wallén E, Johansson U, et al. Description of the new I1011 beamline for magnetic measurements using synchrotron radiation at MAX-lab. Journal of Physics: Conference Series 2010, ***211:*** *012030.*

84. Cui B, Song C, Wang YY, Yan WS, Zeng F, Pan F. Tuning of uniaxial magnetic anisotropy in amorphous CoFeB films. Journal of physics Condensed matter: an Institute of Physics journal 2013, ***25****(10)****:*** *106003.*